Gravity Wave Parameterization in the General Circulation Model

A THESIS SUBMITTED IN PARTIAL FULFILLMENT
OF THE REQUIREMENTS FOR THE DEGREE OF DOCTOR OF PHILOSOPHY IN PHYSICS

by

Mohar Chattopadhyay

UNIVERSITY OF CANTERBURY

Department of Physics and Astronomy

CHRISTCHURCH , NEW ZEALAND

Acknowledgements

I would first wish to thank my supervisor Dr. Darlene Heuff without whom I would not be at this stage today and associate supervisor Dr. Bryan Lawrence. On the same note, I extend my thanks to Dr. Don Grainger who has supervised me for a brief period.

My gratitude goes to all my colleagues, especially, Scott Osprey, Sam Dean, Jelena Aitic, Trevor Carey-Smith, John Grant, Daniela Wurl and Benjamin Williams who have been with me in good times and bad.

On the matter of science, I am grateful to Drs. Bryan Lawrence and Scott Osprey for providing me with all input. Many thanks also go to David Stainforth and Stuart Webster for their advice.

I am grateful to the University of Canterbury and Marsden Fund for supporting my work for these years and also for the time spent in Rutherford Appleton Laboratory, UK. I am thankful to the Met. Service NZ for their support and for allowing to use their resources while completing the thesis.

Last but not the least I want to thank my family, especially my husband Deb, for his support and encouragement.

Abstract

Although there is a rich literature on modelling the effects of broad spectrum gravity waves (GW) in General circulation Models (GCM), the effect of a coupled interactive broad spectrum and monochromatic GW has not been studied in detail. Such a study is of paramount importance as it could conclusively demonstrate that the coupled interactive broad spectrum and monochromatic GW can be parameterized in a GCM and its effects on atmospheric circulations can be studied.

The main objective of this thesis is to investigate how the climate simulated by the Unified Model (UM), a state-of-the-art GCM, responds to more physically realistic gravity wave parameterizations, beginning with the addition of a spectral gravity wave scheme, and then progressing to a scheme which couples both orographic and spectral gravity waves.

Behaviour of the schemes are analyzed using a set of four idealized experiments in a single column test-bed based on the architecture of the UM. Results from these experiments are discussed before implementing the schemes in the UM. These findings provide the necessary backdrop around which more complex interactions modelled by the UM are discussed.

The UM is run for six years with the two GW schemes. Monthly means of a range of diagnostic fields results are compared qualitatively with the U.K. Met. Office global assimilated data. Both schemes simulate the overall structure of the atmospheric circulation. The simulations based on the two GW schemes are also compared against each other to observe any potential effect on the climatology of the UM due to their different underlying assumptions. The results show sensitivity of the model in the dynamics of middle atmosphere. Some degree of variability is also exhibited in tropospheric circulation. A major conclusion that emerges from the extension of the spectral gravity wave scheme to the coupled interactive scheme is that the latter is equivalent to a change in the global mean gravity wave strength.

Contents

Figures

Tables

Chapter 1

Introduction

The last two hundred years have seen the ever increasing industrialization of the human civilization. Although such industrialization has indeed made our life more prosperous, its negative influence on our environment can not be ignored. Our atmosphere is exposed to a large amount of chemical pollutants and the resultant ill-effects are growing at an alarming rate. The effect of pollutants in the atmosphere with respect to ozone was first predicted by *Molina and Rowland* (1974) who suggested that stratospheric ozone [1] could be destroyed by the chlorofluorocarbons (CFCs) widely used in everyday life. This prediction was echoed in *Farman et al.* (1985) when they observed the ozone 'hole' over Antarctica. This discovery has played a crucial role in providing the impetus for further studies of the atmosphere to ensure a safe environment for support of our very existence.

Mathematical models of the atmosphere are an important tool for the study of the human impact on climate. Studies of past, present and future climate can be performed using atmospheric models or General Circulation Models (GCMs). In addition, the possible impact of various anthropogenic changes in future climate can be predicted by performing various sensitivity studies using GCMs.

The concept of mathematical modelling of the atmosphere was introduced by *Richardson* (1922) and after the development of electronic computers, a successful forecast was provided by *Charney et al.* (1950). With the advancement of powerful computing systems, mathematical modelling of the climate has improved immensely in recent times. Some examples of the various GCMs used world wide include: the National Centre for Atmospheric Research (NCAR) Community Climate Model (CCM), the Geophysical Fluid Dynamics Laboratory (GFDL) SKYHI model, the Goddard Institute of Space Studies (GISS) Global Climate Model (GCM), the Canadian Middle Atmosphere Model (CMAM), the European Centre-Hamburg Model ECHAM, the United Kingdom Meteorological Office (UKMO) Unified Model (UM).

[1] It should be noted here that ozone works as a shield and protects the biosphere from the sun's harmful ultraviolet radiation.

The modern GCMs address different physical properties of the atmosphere such as cloud formation, convection, radiation, diffusion etc. These processes cannot be adequately resolved in a numerical simulation. As a result, the physical effects of these processes are represented based on simplified parameters which are predicted by invoking basic physics contained within the model.

The World Climate Research Programme is supporting a project titled 'Stratospheric Processes and their Role in Climate' to test the performance of various GCMs used around the world. *Pawson et al.* (2000) have compared 13 state-of-the-art GCMs and have produced some preliminary results. Their results indicate that all models have shortcomings in their present-day simulation of climate, which limit their accuracy of predictions. Gravity wave drag parameterization is one of the major issues reported by *Pawson et al.* (2000). GCMs that do not have gravity wave drag parameterization are reportedly deficient in simulating many important features of the atmosphere, such as, the strength and position of the major stratospheric jet streams are misrepresented, and a cold bias is found in all locations.

Gravity waves (GWs) are disturbances in which buoyancy acts as restoring force. The momentum flux deposition from a spectrum of upward propagating GWs play an important role in the dynamical driving of the atmosphere (*Manzini and McFarlane*, 1998). GWs transport horizontal momentum and energy from the ground to the upper levels of the atmosphere or, more generally, from one layer of the atmosphere to another. The scales of GWs are smaller[2] than that resolved by a traditional GCM and hence they are parameterized.

The objective of this thesis is to study the effects of GW parameterization schemes, based on different physical regimes, in a GCM. In order to achieve this goal, the UM has been used to incorporate the gravity wave parameterization schemes to develop insight about the effect of their differences in climate simulations.

The Unified Model (UM) is developed and maintained by the UKMO, (*Unified Model User Guide*, 1998). The model supports both global and regional domains and is applicable to a wide range of spatial and temporal scales. The major features of the UM include

[2]Horizontal wavelength of these waves extend from tens to hundreds of kilometers and vertical wavelength extend from 5 to 15 km.

the consistency of its solutions for long integrations which is highly desirable for climate change experiments. The UM has its own customized GW parameterization schemes. The model simulates orographically induced GW up to a height of 25 km; beyond that height, it uses a Rayleigh friction.

In this thesis, two additional physically realistic gravity wave parameterization schemes, developed on different physical principles, are incorporated in the UM. These are the Doppler Spread Parameterization (DSP) scheme following *Hines* (1997a) and the coupled interactive broad spectrum and monochromatic wave scheme based on *Hines* (1997b). The purpose of this thesis is to investigate the sensitivity of the UM to the different underlying assumptions of these schemes, rather than attempting to establish the superiority of one over the other.

This thesis is structured as follows. Chapter 2 begins with the description of the basic equations governing the atmosphere. The role of GWs in these equations and the need for simulating their effects in GCMs are established. The GW parameterization schemes are constructed on the grounds of much observational evidence. A short literature survey on the results of different observational studies is presented before describing the parameterization schemes used in the GCMs. The effect of the gravity wave parameterization on the model's atmosphere can be identified in different dynamical processes and these processes are explained in detail at the end of the chapter.

The version of the UM used in the present work, is introduced in Chapter 3. The GW parameterization scheme originally employed in the UM is presented in detail including the implementation of the scheme in the UM. The technical details of incorporating the DSP scheme in the UM is presented next. Finally, the implementation of the 'coupled interactive' broad spectrum and monochromatic waves scheme in the model is explained.

Before implementing the new schemes in the UM, their performance was tested in a single column test-bed. The test-bed is based on the UM's architecture but it includes fewer parameter spaces than the UM. A description of the test bed is provided at the beginning of Chapter 4. Four idealized test cases were designed to provide insight into the behaviour of the schemes in an environment similar to that of the UM. The propagation of GW under different physical regimes inside the test-bed was studied extensively, and is discussed in Chapter 4.

Having tested the performance of the schemes in the simple test-bed and analyzed the resultant effects, the schemes were incorporated in the UM to study their effects on a global climate. The UM simulations employing both schemes covered a period of six years.

Although studies incorporating the DSP and 'coupled interactive' schemes in the models have been reported by *Osprey and Lawrence* (2001), troposphere was not included in their model. The inclusion of a troposphere within the UM has contributed to the uniqueness of this study. Hence, in Chapter 5, the effect of different GW parameterization schemes on the tropospheric circulation is discussed.

The effect of gravity wave forcing has been largely felt in the middle atmosphere where it plays an important role in the circulation. In Chapter 6, simulations of the middle atmosphere dynamics in both the hemispheres is examined and the differences are explained in terms of the difference in the GW acceleration of the two simulations.

Although GWs contribute to the climatology of the global circulation, their effects can also be identified in the circulations that take place at a daily scale. To study these features, daily data for an arbitrary simulation year is examined extensively. The direct and indirect effects of forcing produced by GW acceleration on these features are discussed in Chapter 7.

Finally, in Chapter 8, a comprehensive summary of the major contributions of the present research is provided and a few potential extensions of the work are discussed.

Chapter 2

Mathematical Modelling and Atmospheric Processes

2.1 Introduction

GCMs, such as the UM, attempt to provide detailed simulation of the observed atmosphere. Within the UM, atmospheric circulation is governed by primitive equations which are introduced in this chapter. The formulation of GWs in the primitive equations and the importance of parameterization of GW is briefly explained. A literature review describing recent developments on the subject of GW and the different parameterization schemes used in the GCMs is then presented. Finally, the atmospheric processes driven by GWs are described.

2.2 Modelling and the primitive equations

The atmospheric motion is governed by the fundamental laws of physics. The primitive equations are an approximation of these laws which can be represented by a set of five equations. They may be expressed in terms of spherical polar coordinates (*Andrews et al.* (1987), *Holton* (1979) and *Holton* (1992)). The UM is based on a discrete representation of the primitive equations also represented using spherical polar coordinates, as shown in *Appendix A* (*Cullen et al.*, 1993).

2.2.1 The primitive equations

The primitive equations consist of the zonal and meridional momentum equations, the vertical momentum equation subject to the hydrostatic approximation, the continuity equation and the thermodynamic energy equation. In spherical polar coordinates these may be written as follows:

$$Du/Dt - (f + u\tan\phi/a)v + (1/a\cos\phi)\partial\Phi/\partial\lambda = X, \tag{2.1}$$

$$Dv/Dt + (f + u\tan\phi/a)u + (1/a)\partial\Phi/\partial\phi = Y, \tag{2.2}$$

$$\partial\Phi/\partial z = H^{-1}RT, \tag{2.3}$$

$$(1/a\cos\phi)\partial u/\partial\lambda + (1/a\cos\phi)\partial(v\cos\phi)/\partial\phi + \rho_0^{-1}\partial(\rho_0 w)/\partial z = 0, \tag{2.4}$$

$$DT/dt + (\kappa T/H)w = J/c_p, \tag{2.5}$$

where

$$D/Dt \equiv \partial/\partial t + (u/a\cos\phi)\partial/\partial\lambda + (v/a)\partial/\partial\phi + w\partial/\partial z$$

Here u is the zonal wind, v is the meridional wind, w is the vertical wind, a is the radius of the earth, z is the 'log-pressure' height; $z = -H\ln(P/P_s)$, λ is the longitude, f is the Coriolis parameter; $f = 2\Omega\sin\phi$, ϕ is latitude; Ω is the angular velocity of the earth, Φ is the geopotential[1] which is given by $\Phi \equiv \int_0^{z^*} g dz^*$, ρ_0 is the basic state density, $\rho_0 = \rho_s \exp(-z/H)$, ρ_s is the standard reference density, J is diabatic heating rate per unit mass, c_p is specific heat of air at constant pressure, R is the gas constant ($= 287 J/K/kg$ for dry air), $H = RT_s/g$ is the scale height, $\kappa = R/c_p$, T is the temperature, T_s is the reference standard temperature. X and Y are of special importance in the present context. They are the zonal and meridional components of friction, or other nonconservative mechanical forcing due to small-scale eddies, such as, turbulent activities and GWs. It is the form of these two variables that vary based on the choice of parameterizations of the unresolved physical processes.

2.3 Gravity waves

GWs can exist only when the atmosphere is stably stratified so that an air parcel displaced vertically will undergo buoyancy oscillations. Buoyancy force is the restoring force responsible for GWs. GWs can be excited in a number of ways such as : wind flowing over orography, convective processes and jet stream activities in the troposphere. As the waves travel upward in the atmosphere, their amplitudes grow due to the decrease in density. When the amplitudes become too large, the waves start dissipating transferring momentum and energy into the background wind field.

The breaking GW have a noticeable impact on the atmospheric circulation. However, their associated scales of motion are smaller than that resolved by the current numerical grids of the GCMs and therefore the effects of GWs must be parameterized. The importance of GW parameterization in a climate model was shown by *Mayr et al.* (1997). They

[1] work done to lift an air parcel of unit mass from sea level to geometric height z^*

conducted simulations using a two dimensional Numerical Spectral Model (NSM) with and without a GW parameterization scheme. The results obtained from the model with the parameterization scheme showed a more realistic circulation of the middle atmosphere which was not displayed by the latter.

To simulate GWs in a climate model, it is necessary to have an estimation of parameters such as source strength, form and energy of the waves based on observations. Information on these parameters are obtained from observational data from balloons, radar, lidar and radiosondes. Some recent results from the observational studies are outlined below.

2.3.1 Observations of gravity waves in the atmosphere

To model GWs, it is very important to know the sources of GW and the geographical distribution of these sources. It is believed that orography or mountains contribute significantly to the origin of GW. The proof of the existence of 'orographically induced' gravity waves was provided by *Lilly et al.* (1982) who analyzed wind and temperature data obtained from aircraft measurements over the Rockies and found that GWs in that region were generated due to the interaction of the wind field with the mountains.

Studies by *Epsy and Huppi* (1997) with an aircraft-borne Michelson Interferometer within the inter tropical convergence zone (ITCZ[2]), and by *Sato et al.* (1995) and *Sato* (1996) with UHF/VHF radars and radiosondes in equatorial regions, showed that tropospheric convection is another major source of GW.

Allen and Vincent (1995) took radiosonde observations from 18 meteorological stations within Australia and Antarctica covering a latitude range of $12°S - 68°S$ and a longitude range of $78°E - 159°E$. They found strong seasonal variations of wave activity in the stratosphere. At lower latitudes ($10°S - 20°S$) a clear annual variation was observed with wave energy peaking during the monsoon months of December to February. At mid-latitudes ($30°S - 40°S$) a maximum was seen during the winter months when cold fronts swept across that region. A transition between these two regimes occurred at intermediate latitudes ($20°S - 30°S$) where a semiannual variation was observed. However, the seasonal variations of wave activity in the troposphere were less clear.

[2]The region of low-level convergence toward the upward branch of the Hadley cell (*Washington and Parkinson*, 1986)

In another report, *Gavrilov* (1996) analyzed the height, seasonal and latitudinal variations of the parameters of GWs using a ground-based radar, it was suggest that one of the important sources of the continual generation of GWs in the atmosphere is nonlinear interaction of different atmospheric motions. These studies gave evidence of the source strength and geographical variation of the sources of GW.

In addition to determining the sources of GWs and their geographical variation, studies have also been conducted on the propagation of these waves to the upper atmosphere. Observations with UHF/VHF radars by *Sato* (1996) revealed that in equatorial regions, strong vertical motion associated with cumulus convection plays an important role in the transport of GW energy from the troposphere to the stratosphere. Satellite observations by *Wu and Waters* (1996) at a height range of 30 to 80 km indicated that the background wind fields also plays a major role in determining the amplitudes of the GWs.

Results presented by *Vincent et al.* (1996), suggest that the directions of propagation of GW are limited. It was suggested that this might be related to dominant forcing mechanisms responsible for wave generation, or to filtering of waves by the background wind. Their radar data of wind and temperature fluctuations produced evidence of GWs that are quasi-monochromatic (QMC) in nature.

As discussed earlier, the vertically propagating GW generated in the troposphere dissipate as a result of wave breaking. The resulting absorption of the wave energy by the background wind field plays a major role in middle atmosphere dynamics, as reported by *Gavrilov* (1996). He deduced from his ground-based radar data that the convective and dynamical instability generated by the dissipating GWs could cause turbulence in the upper atmosphere, as high as 100 km and above. This was also supported by *Yu and She* (1995), who observed the mesopause region, at altitudes of approximately 90 km, using a lidar. Their analysis of the results revealed that heating in the mesopause is dominated by dynamical forcing GWs.

2.3.2 Gravity wave parameterization in General Circulation Models

The observational evidence provides grounds on which gravity wave parameterization schemes can be formulated. Most of the schemes make certain initial assumptions on the basis of these observations, as to the source of the waves and how they propagate. The exact way in which these processes are represented, however, varies from scheme to

scheme. A few examples of different schemes developed in time are stated below.

Rayleigh friction

Rayleigh friction assumes that due to dissipation of GWs, momentum flux is deposited linearly with height in the background wind. The scheme was first introduced by *Leovy* (1964) to calculate the zonal mean circulation of the mesosphere. In the zonal momentum equation (equation 2.1) the forcing by Rayleigh friction is expressed as

$$X = -K(z^*)U, \tag{2.6}$$

where $K(z^*)$ is a pre-defined damping rate depending upon altitude z^*, and U is the zonal wind speed. Rayleigh friction is used to prescribe a momentum source such that it is substantially larger in the upper mesosphere and lower thermosphere, and negligible elsewhere. It turns out to be negative in the winter hemisphere and positive in the summer hemisphere. The presence of such a force supports a non-zero steady-state meridional wind in the mesosphere that is directed from the summer pole to the winter pole.

In many GCMs, realistic effects of radiative and dynamical processes are obtained using a Rayleigh friction coefficient, $K(z^*)$, that increases with height. For example, *Holton and Wehrbein* (1980) and *Schoeberl and Strobel* (1978) used the Rayleigh friction scheme in order to obtain realistic zonal mean winds and temperatures in the upper stratosphere and mesosphere. *Pawson et al.* (1998) and *Butchart and Austin* (1998) have also used this scheme in the UM to simulate the circulation of the middle atmosphere.

However, it is also reported by *Holton and Wehrbein* (1980) and *Schoeberl and Strobel* (1978) that simulations using Rayleigh friction cannot generate either extra-tropical zonal mean winds that change sign in the mesosphere, or tropical oscillations such as the mesospheric semiannual oscillation. Hence, it is not extensively used in the climate models now a days.

Lindzen parameterization

The assumption that GWs deposit their momentum and energy linearly with height leads to an inaccurate simulation of winds and temperatures in a GCM (*McLandress*, 1998) and (*Lindzen*, 1981).

GWs are treated as linear and monochromatic disturbances that propagate energy upward in a slowly varying background wind, and do not interact with one another, implying that the waves are discrete in nature. The wave amplitudes grow exponentially with height and at some height an individual wave becomes convectively unstable. This height is known as the 'breaking height' where convective overturning is assumed to generate small-scale turbulence that damp the waves. Above the 'breaking height', the wave is assumed to be saturated, that is, the vertical wave number of the waves remain roughly unchanging in amplitude with height. The eddy diffusion required to maintain neutral stability causes a momentum flux that decays with height. The momentum flux is described by

$$\tau_u = \rho\eta\frac{k(c-U)^3}{2N}, \tag{2.7}$$

where ρ is the density, η is the efficiency factor varying from 0 to 1, k is the zonal wavenumber, c is the ground based zonal phase speed, U is the eastward wind, N is the static stability (see *Appendix C*). Above the breaking height the resulting zonal force obtained is given by

$$X = \frac{\eta k(c-U)^3}{2N}\left[\frac{1}{H} + \frac{3}{c-U}\frac{dU}{dz}\right], \tag{2.8}$$

Below the breaking height $X = 0$. This parameterization can also be used for GWs generated by flow over topography [3].

Application of the Lindzen parameterization in a two dimensional mechanistic model of the middle atmosphere showed the scheme to be superior to the Rayleigh friction scheme (*Holton*, 1982). *Garcia and Solomon* (1985) also reported that the use of discrete waves with different phase speeds in the Lindzen parameterization resulted in a better simulation of middle atmospheric circulation than was possible using Rayleigh friction.

Orographically induced gravity wave drag parameterization

Orographically induced GW has been parameterized by *McFarlane* (1987), *Milton and Wilson* (1996), *Bacmiester et al.* (1994), *Shutts and Gadian* (1999) and *Medvedev et al.* (1998). The orographically induced GW scheme in the UM is based on the premises of *Palmer et al.* (1986) and is incorporated by *Gregory et al.* (1998). A brief description of the scheme is given below and a detailed description is presented in Chapter 3.

[3] It can be coupled with continuous spectral schemes which are described later in this chapter

The parameterization is done in two parts. First, a formulation is developed for surface stress due to orography and the surface stress is oriented in the direction of the surface wind.

Secondly, a separate computation is performed for the vertical distribution of GW stress accompanying the surface value. Some GWs are damped by the 'hydraulic jump' phenomenon that may form on the lee slopes of mountains under certain conditions (*Holton*, 1992). However, these waves are not totally dissipated at the 'jump height', which is the altitude at which the 'hydraulic jump' takes place. The remaining stress is carried higher up in the atmosphere, breaking at what is called the 'critical level'.

Wave propagation in the vertical may also occur in a 'trapped lee-wave regime', which also involves wave damping due to reflection of these waves in the lower atmosphere (*Holton*, 1992). The waves are totally dissipated in this regime and the stress associated with these is deposited in the background wind.

The remaining wave energy including that from the 'hydraulic jump' regime is dissipated via a 'saturation' regime. The vertically propagating GWs in the 'saturation' regime are assumed to break at a level where a suitably defined Richardson number $[R_i = \frac{N^2}{(du/dz)^2}]$ for a wave falls below a critical value of 0.25. The identification of the critical level is based upon a combination of shearing and convective instability.

The total stress is calculated by adding all the stress generated by the above physical processes. The acceleration produced by the overall stress is calculated as:

$$F = \delta u/\delta t = g(\delta\tau/\delta p), \tag{2.9}$$

where $\delta u/\delta t$ is the acceleration, $\delta\tau$ is the difference between the stress for two consecutive levels, δp is the difference in pressure between two levels and g is the acceleration due to gravity.

The UM simulations with this scheme reveal that, at some places, the forcing due to GW is overestimated (*Gregory et al.*, 1998). Also, the behaviour of the scheme was not found to be smooth in space and time at higher altitudes above approximately 20 hPa (*Swinbank et al.*, 1998). These are some common disadvantages of an orographically induced GW

schemes.

Doppler spread parameterization

It should be worth noting here that observational studies conducted using radar by *Fritts and Chou* (1987), *Tsuda et al.* (1989) and *Vincent et al.* (1996) indicated that GW may have continuous spectrum and their results show excellent agreement with the hypothesis which is explained below.

It was assumed by *Dewan and Good* (1986) that the threshold amplitudes of instabilities that produced a saturated spectrum of GWs were functions of vertical wave number m. Hence, a universal vertical wave number spectrum (M) of horizontal wind can be formulated as a function of m. *Dewan and Good* (1986) followed by *Smith et al.* (1987) formulated the 'power spectral density', $M(m)$, of a saturated GW spectrum as:

$$M(m) \propto \frac{N^2}{2m^3}, \text{for } m \gg m_*, \tag{2.10}$$

where m_* is the characteristic vertical wavenumber of the GW spectrum.

At the low wavenumber end of the spectrum, $M(m)$, is assumed to be proportional to m^s, where s is a positive number (frequently chosen to be 1). Between the high and the low wave numbers is the region known as the 'knee' of the spectrum, where $M(m)$ is maximum and the associated horizontal wind is the strongest. The wavenumber corresponding to the knee is referred to as the characteristic vertical wavenumber (m_*) and observations indicate that it decreases with increasing height which implies that the m^{-3} tail commences at smaller wave numbers at greater heights.

The DSP scheme assumes that GWs are spectral in nature. According to the scheme, a broad spectrum of GWs can be characterized by a unique power spectral density of horizontal winds it produces at certain height and it depends on the values of vertical wave-numbers m_j at that height. The spectrum of waves is characterized by a height-varying cutoff value of m_j, denoted as m_c. The waves are destroyed if;

- waves with substantially small m_j values retain their current m values,
- waves with m_j values exceeding the current m_c are thought to be dissipated as they have approached a critical layer and

- waves having m_j near to but less than m_c contribute to the characteristic 'm^{-3} tail' of the middle-atmosphere spectrum.

The diminution of the value of vertical wavenumber m with increase in height is used to determine the rate of horizontal momentum deposition. The vertical flux of the horizontal momentum is taken to be conserved until dissipation of waves occur. With the obliteration of waves, horizontal momentum flux is deposited which generate energy on the mean flow of background wind (*Hines*, 1997a) and (*Hines*, 1997b).

Implementation of the DSP scheme has been carried out by *Manzini and McFarlane* (1998), *Mayr et al.* (1998a) and *Lawrence* (1997a) in their respective models. The results show that the models have successfully simulated the dynamics of the atmosphere using this scheme. This scheme is implemented in the UM for the present study and a detailed mathematical description is provided in Chapter 3.

Coupling the broad spectrum and the monochromatic waves

When the monochromatic waves are superimposed on the broad spectrum waves, the Doppler spreading of the waves are modified with inclusion of the RMS wind variance of the monochromatic wave. As a result, the atmosphere becomes predisposed to instability and the height varying cut-off vertical wavenumber (m_c) is reduced by a certain factor. When the monochromatic part of the spectrum break-down, that part of momentum flux is added to the momentum flux of the broad spectrum and the total change in the momentum flux is used to calculate the overall acceleration on the background wind (*Hines*, 1997b).

In this thesis, a 'coupled' interactive broad spectrum and monochromatic wave parameterization is also incorporated in the UM. A detailed mathematical description of the schemes is provided in Chapter 3. The orographically excited GW of the UM are combined with the DSP scheme following the theory in *Hines* (1997b) to analyze the potential effect in the model's dynamics.

Incorporating alternative GW parameterization schemes in a GCM has certain implications and in particular, this thesis focuses on the effects of GWs on atmospheric dynamics from the ground up to 80 km. It should be mentioned here that the atmosphere's dynamic processes vary with altitude owing to its underlying thermal structure. Hence,

before discussing the dynamics, a brief introduction to the different layers of the Earth's atmosphere is provided.

2.4 The atmosphere

From the ground to 100 km, the atmosphere can be divided into four different layers according to its global-mean thermal structure which also determines the dynamic properties of individual layers. Figure 2.1 depicts the typical temperature profile of the atmosphere at mid-latitudes.

The lowest 10 to 15 km of the earth's surface is known as the troposphere, where temperature normally decreases with altitude. Temperature in the troposphere is maximum near the equator and is minimum near the poles.

The layer immediately above the troposphere is the stratosphere, which extends from approximately 12 km to 50 km above the surface. The temperature in the stratosphere increases with height to a maximum at the stratopause, near 50 km. This layer plays an important role in the dynamical processes of the atmosphere due to the presence of ozone.

The next layer above is called the mesosphere. The temperature decreases with height in the mesospheric region which extends up to 90 km. The region including the stratosphere and the mesosphere is known as the middle atmosphere, and is the focus of this thesis.

The layer above this is the thermosphere where temperature steadily increases with height (*Holton*, 1979; *Trenberth*, 1992).

In the following section, those aspects of the atmosphere's dynamics that may be affected by the presence of GW are discussed in detail.

2.5 Dynamics of the atmosphere

2.5.1 Diabatic circulation

The temperature distribution of the atmosphere, as described before, is dependent upon the seasonal variation in solar heating. Under solstice conditions, the summer pole above

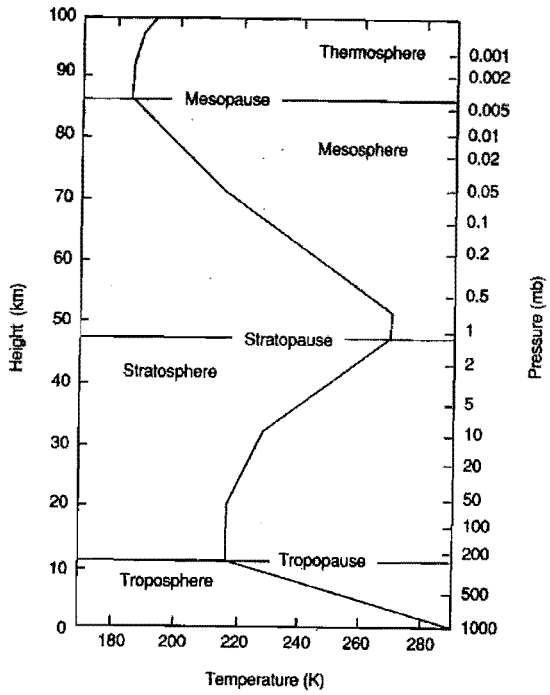

Figure 2.1: Mid-latitude Mean Temperature Profile (*U. S. Standard Atmosphere*, 1976).

the stratosphere is the region of maximum radiative heating and the winter pole is the region of minimum heating. At the equinoxes, there is a cooling at both poles and the maximum radiative heating is seen in the equator. A radiatively-driven atmosphere at solstice condition is shown in figure 2.2.

However, the temperature profile of the real atmosphere at solstice condition, shown in figure 2.3, differs significantly from that of the radiatively determined temperature profile of the atmosphere. Figures 2.2 and 2.3 are provided as a gross reference to the temperature profiles of the atmosphere. It should be noted that the temperature and wind profiles change seasonally and are also different in the two hemispheres.

The largest departure of the real atmosphere from a radiatively-driven atmosphere is observed in the mesosphere, above approximately 60 km. It has been observed that the mesosphere in summer is colder by 50 to 60 K compared to the mesosphere in winter, although the latter does not receive any direct solar radiation.

The zonal mean temperature is directly linked with the zonal mean wind through the thermal balance equation (explained in *Appendix B*). Figure 2.4 shows the zonal mean

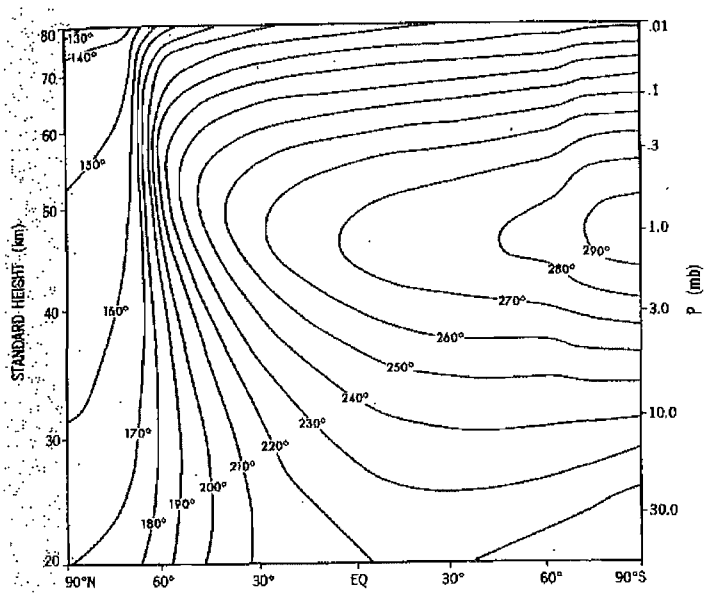

Figure 2.2: Zonal mean time-dependent radiatively determined temperature (K) for January (*Fels*, 1985).

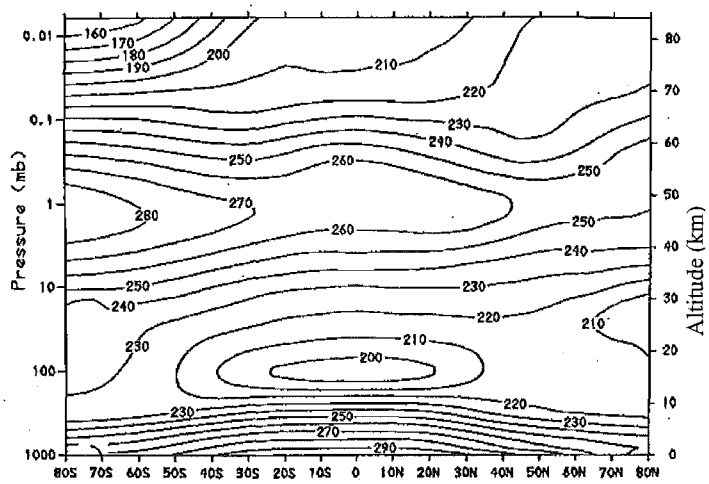

Figure 2.3: Zonal mean temperature (K) for January (*Fleming et al.*, 1990).

zonal wind profile for the same month. The closing of zonal mean wind jets in the lower mesosphere and change in the shear of the same in the upper mesosphere is directly linked with the change in the temperature gradient seen in figure 2.3.

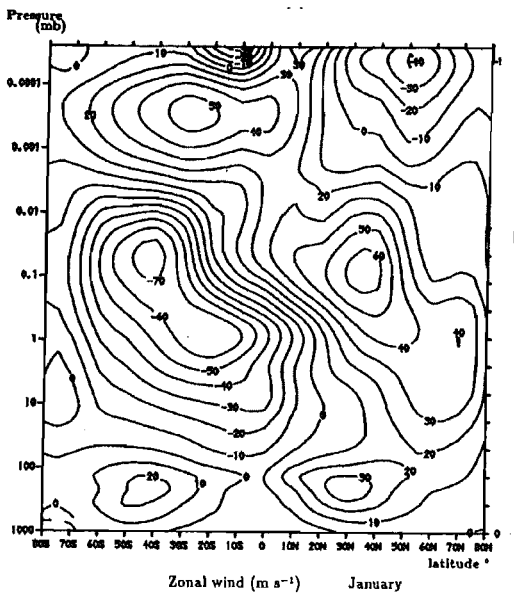

Figure 2.4: Zonal mean zonal wind for the month of January (*Holton*, 1992).

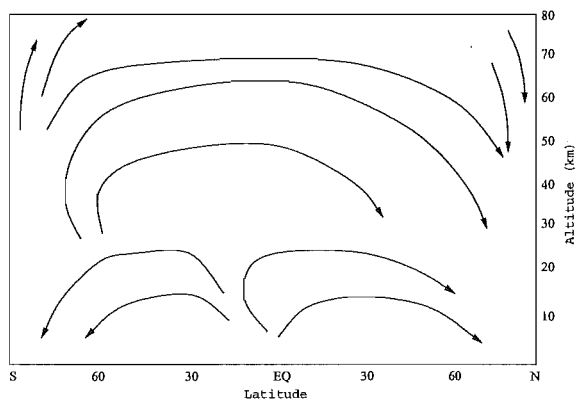

Figure 2.5: Mean meridional circulation in troposphere and middle atmosphere for Northern Hemisphere winter.

If the atmosphere was solely radiatively driven, as depicted in figure 2.2, then the jet streams in the middle atmosphere would be very large and they would continue to grow with height contrary to the observations, (*Geller*, 1997). Instead, the overall latitudinally dependent temperature distribution in the middle atmosphere (figure 2.3) arises from a

balance between the net radiative equilibrium and dynamical heating or cooling induced by atmospheric waves.

It has already been discussed that the net radiative heating distribution has a strong seasonal dependence with the maximum heating at the summer pole and the maximum cooling at the winter pole. The circulation in the meridional plane dynamically balances this differential heating and is called 'diabatic circulation'. This circulation is driven by eddy forcing produced by atmospheric waves such as GW. At the solstice, the diabatic circulation consists of a rising motion near the summer pole, meridional drift into the winter hemisphere and sinking near the winter pole. The Coriolis torque exerted by this meridional drift tends to generate mean zonal westerlies in the winter hemisphere, and easterlies in the summer hemispheres that are in approximate geostrophic balance with the meridional pressure gradient (*Andrews et al.*, 1987).

The diabatic circulation as discussed above can be represented by figure 2.5. At lower levels, two cells exist with a motion from the equator to the pole, with a single cell circulation at higher altitudes, approximately at 65 km. This circulation from summer pole to winter pole is believed to be driven by upward propagating GWs directionally filtered by mean wind structure. The vertical motion accompanying this circulation produces compressional heating, where the motion is downward and expansion cooling where the motion is upward (*Haynes et al.*, 1991). This explains the warm winter and cold summer mesopause and is the basis of *downward control* produced by drag created by atmospheric waves, such as GWs, on the mean zonal flow (*Geller*, 1997).

Haynes et al. (1991) derived an equation describing the amount of vertical motion due to GW forcing at extra-tropical latitudes. According to their calculation, the amount of vertical motion $w_F(z_0)$ due to GW parameterization at height z_0 is given by a downward control integral

$$w_F(z_0) = \frac{-1}{\rho_s(z_0) a \cos\phi} \frac{\partial}{\partial \phi} [\frac{\cos\phi}{f} \int_{z_0}^{z_T} \rho_s(z) F(z) dz], \tag{2.11}$$

where ϕ is the latitude, ρ_s is a standard density, f is the Coriolis parameter, a is the radius of the Earth and F is the body force per unit mass due to the parameterization.

Observational and modelling studies by *McIntyre* (1989), *Seol and Yamazaki* (1999), *Rosenlof* (1995) and *Lawrence* (1997b) have demonstrated the effect of the eddy-driven or GW forcing on the diabatic circulation of the middle atmosphere.

2.5.2 Stratospheric sudden warming

It is explained in the preceding section how GW driven diabatic circulation can induce dynamical changes in the mesosphere. In this section, another feature of the middle atmosphere driven by GWs is described.

Climatological zonal mean zonal winds in the winter stratosphere during solstice are generally westerly and increase with height (figure 2.4), while the zonal mean temperature decreases towards the winter pole along constant pressure surfaces in the stratosphere (figure 2.3). This can be explained in terms of the thermal balance equations discussed in *Appendix B.*

However, an interesting phenomenon is observed in the northern hemisphere between latitude 60° and the pole. During some winters, the zonal mean stratospheric temperature increases rapidly with time leading to a poleward increase of the zonal mean temperature. This, consequently, reverses the zonal mean wind from westerly to easterly. This leads to the break down of the stratospheric polar night vortex which disrupts the circulation in that region, and giving an impression of a descending stratopause. This phenomenon is commonly known as 'Stratospheric Sudden Warming' (SSW) (*Andrews et al.*, 1987).

These events can be catagorised as either 'major' or 'minor' warmings. A 'major' warming is one in which the reversal of the poleward zonal mean temperature gradient (from negative to positive) and the zonal mean zonal wind (from westerly to easterly) penetrates down to the altitude of the 10 hPa surface, or lower. If the temperature gradient reverses at that level but the circulation does not, it is known as a 'minor' warming. A 'major' warming is further classified as: 'wave−2' warmings, where the polar winter vortex splits completely into two halves and 'wave−1' warmings, where the Aleutian anti-cyclone strengthens and moves longitudinally, finally replacing the vortex over the pole. Major warming events have been noted as occurring once or twice during every northern hemisphere winter, while 'minor' warmings are observed more frequently (*Andrews et al.*, 1987).

Observations of SSW events have been reported by *Rosier et al.* (1994), *Rosier and Lawrence* (1999) and *Ruth et al.* (1994), who studied the data collected by the ISAMS instrument for the northern hemisphere winter of 1991/92. From these reports it is inferred that, at all levels in the stratosphere, the atmospheric circulation was generally

dominated by a cold cyclonic vortex that was mostly centered over or near the pole. This vortex pulsated between roughly circular and somewhat elongated shapes and the vortex was perturbed intermittently by a strong anticyclonic circulation near longitude 180° E. This circulation in the lower stratosphere is commonly known as the Aleutian high. It sometimes appeared to spilt into a lower stratospheric part and an upper-stratospheric part with a weak coupling between the two. In between the near major warming in mid-January, the strength of the Aleutian high increased considerably. The low pressure vortex then moved off the pole, forming a wave−1 structure in the geopotential height field. However, this pattern broke down at higher altitude of 48 km.

The very first attempt at modelling this process was undertaken by *Matsuno* (1971) who demonstrated that unusual amplification of tropospheric planetary waves could provide dynamical forcing for SSWs. Successful simulations of SSW events were also reported by *Erlebach et al.* (1996), *Yoden et al.* (1999) and *Braesicke and Langematz* (2000) with two-dimensional mechanistic models and GCMs.

However, results from an observational study carried out by *Whiteway and Carswell* (1994) with a Rayleigh lidar at the northern hemisphere pole during winter suggested that the temperature fluctuations in that region were caused by GW forcing. *Lawrence* (1997a) has also reported that GWs play an important role in SSW. It was suggested that in addition to any direct effect of GW parameterization in the climate models one also had to take into account the secondary effect of GW forcing in the evolution of stratospheric warming.

Transient planetary waves that propagate from the troposphere to the stratosphere also play an important role during SSW events (*Andrews et al.*, 1987). Prior to a SSW event, these waves, which generally focus equatorwards, change their direction of propagation and focus towards the north pole. This is accompanied by large negative values of divergence of the Eliassen-Palm (EP) flux (see *Appendix C*). The negative values of EP-flux divergence is associated with the rapid rise in temperature in the northern hemisphere stratosphere during the SSW events (*Andrews et al.*, 1987). This feature was demonstrated by the numerical studies of *Dunkerton and Baldwin* (1991), *Yoden et al.* (1999) and *Kodera* (1991), which showed a strong convergence of EP-flux in the upper stratosphere during the SSW phenomenon.

In addition to playing an important role in successful simulation of SSW events, forcing due to GW have been found by *Dunkerton* (1997) to contribute in the simulation of equa-

torial circulation.

2.5.3 Equatorial circulations

The global annual cycle in the equatorial region of the stratosphere is different from that of the extra-tropics in terms of the mean zonal wind and temperature profiles. At an altitude below 35 km, a long term oscillation is observed that is not directly related to the change of season. This oscillation is known as the quasi-biennial oscillation (QBO) and was first reported to be observed in 1961 by *Reed et al.* (1961). Above 35 km, another seasonal variation of the zonal wind occurs which is commonly known as the 'semi-annual oscillation' (SAO). Since the discovery of these oscillations, a few studies have been conducted to understand the driving forces behind them.

The characteristics of the QBO were reported by *Labitzke and vaan Loon* (1997). The main features include persistent east-west winds that have an average period of 27.7 months. The amplitude of the QBO was also variable, with the largest occurring between altitudes of 25 to 30 km where the mean velocity was 30 to 40 m/s. The QBO propagated downwards with the westerlies descending faster than the easterlies. It was noted that the SAO consists of two separate oscillations centered at the stratopause and one at the mesopause, that have opposite phases. The SAO appeared at first in the mesosphere and then propagated downward in the stratosphere. However, the downward propagation was mainly in the westerly phase of QBO, figure 2.6.

Earlier theory suggested that the SAO and the QBO might be caused by radiative forcing. More recently *Andrews et al.* (1987) have postulated that the easterly phase of the SAO is forced by residual mean meridional circulation or diabatic circulation (explained in section 2.5.1), while a recent analysis of UKMO data by *Ray et al.* (1998) illustrates that GWs are the primary source of momentum for westerly phase of the SAO.

Some observational and theoretical studies have stated that mesoscale GWs contribute $10 - 20\%$ of the observed QBO accelerations. *Canziani and Holton* (1998) reported after analyzing various satellite, radar and simulated data that for the occurrence of the westerly phase of the QBO, an enhanced westerly forcing was needed that was apparently provided by GWs. In another study, *Dunkerton* (1997) simulated the QBO using a two-dimensional model. The results showed that GWs have an important role to play in driving the QBO and the majority of these waves have critical levels in descending QBO

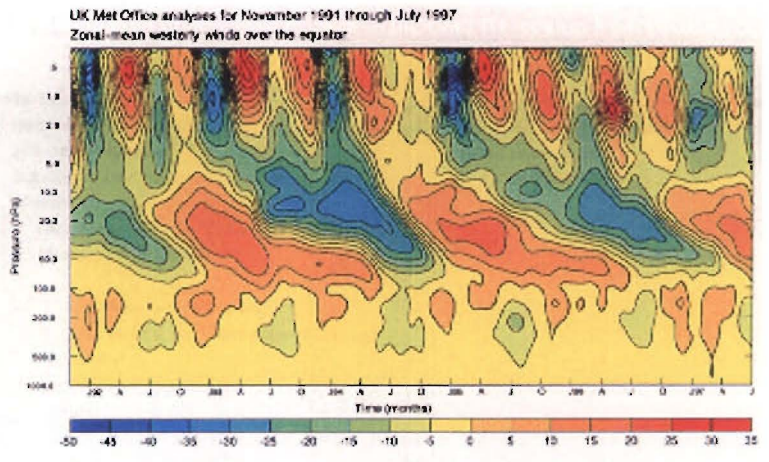

Figure 2.6: Time-series of zonal winds over the equator, analysed using stratospheric configuration of the Unified Model. The winds show a clear QBO in the stratosphere and a SAO near the stratopause (*Unified Model User Guide*, 1998).

shear zones. The study also illustrated that the local spectrum of GW phase speeds in the middle atmosphere is modulated by the mean flow at the underlying levels. Hence, at certain phases of the QBO, when the winds are easterly or westerly over a deep layer, waves with phase speeds of opposite sign escape to higher altitudes and contribute to shear-zone descent of the SAO at the stratospause or the mesopause.

Mayr et al. (1997) also simulated both the QBO and SAO in a two dimensional model with a broad spectrum GW drag parameterization. Without the GW drag, the SAO feature was not reproduced by the model while the same feature was reproduced with the GW parameterization. The model also simulated the QBO with a periodicity of 21 months and an amplitude of 8 m/s. A broad spectrum GW drag parameterization scheme has also been used by *Scaife et al.* (2000) in the UM with a GW source strength of 1.75 m/s to simulate the QBO with satisfactory results. In another study, *Mayr et al.* (1998b) showed that, filtering of GWs by the zonal wind could produce the observed equatorial variability. Yet another successful simulation of both the SAO and QBO was reported by *Takahashi* (1999).

Independent studies by, *Dunkerton and Baldwin* (1991), *Kodera* (1991) and *Yoden et al.* (2001) demonstrated that there was a link between the occurrence of SSW and QBO in the tropical lower stratosphere. *Dunkerton and Baldwin* (1991) also stated that a weaker than normal polar night jet and a warmer than normal polar temperature could be associated with an easterly phase of QBO at 27 km altitude.

2.6 Summary

This chapter started with an introduction to the primitive equations which are used to represent the atmospheric processes within GCMs. The importance of GW in these equations and hence the need for their parameterization was established. Different GW parameterization schemes have been discussed in detail including the DSP scheme, and the 'coupled' broad spectrum and monochromatic wave scheme, both of which are incorporated in the Unified Model (UM) in the present research. Some potential consequences of incorporating GW parameterization in a GCM can be observed in the middle atmosphere dynamics, which was discussed in the final section along with the relevant literature.

In the next chapter, the UM, which is used as a tool to investigate the effect of different GW parameterization schemes, is described, and implementation of the DSP and 'coupled' broad spectrum and monochromatic schemes in the UM are discussed in detail.

Chapter 3

Gravity Wave Parameterization Schemes in the Unified Model

3.1 Introduction

This chapter focuses on the incorporation of the gravity wave parameterization based on different physical regimes into the UM. The chapter is laid out in the following manner. A description of the UM with the different parameterization employed is presented. Then, a detailed explanation of the GW parameterization in the UM is provided. The chapter is concluded with a discussion of the implementation of the DSP scheme and the coupled interactive broad spectrum and monochromatic GW scheme in the UM.

3.1.1 Introduction and description of the Unified Model (UM)

The UM is developed and maintained by the UKMO. It is an atmospheric General Circulation Model (GCM) and can be used to simulate the atmosphere over a wide range of spatial and temporal scales. The UM can be run either as a mesoscale model or as a global scale model, which implies that it can be used as a Numerical Weather Prediction (NWP) model and also as a climate model. For details see the *Unified Model User Guide* (1998).

The equations of motion, or 'primitive equations', used in the model include a full 3-dimensional representation of the Earth's rotation which also accounts for planetary scale motions (*Cullen*, 1993)(detailed equations are provided in *Appendix A*).

The UM uses a hybrid scale to represent the vertical coordinate system (*Swinbank*, 1989). It is terrain-following near the surface and uses constant pressure surfaces higher up. The horizontal scale is arranged according to Arakawa B-grid (*Gadd*, 1985). At the corner points of the horizontal grid boxes, the parameters such as surface pressure (p_s), potential temperature (θ) and humidity mixing ratio (q) are provided, and geopotential (Φ)

and vertical velocity (w) are diagnosed. At the centre of the horizontal grid boxes, the horizontal components of wind velocity (u, v) are provided (details in *Appendix A*).

The UM uses a finite difference scheme for forecasting wind, temperature and other diagnostic fields. The finite difference scheme has a modified split-explicit method which conserves the mass-weighted temperature and moisture, and treats the energy conservation term consistently (*Cullen and Davies*, 1991).

This thesis uses the 'atmosphere' module of the UM in its 'climate mode'. The horizontal resolution used is $2.50^0 \times 3.75^0$ with 96×73 points in east–west and north–south directions, respectively. The vertical scale has 55 levels ranging from ground to 10 hPa, which corresponds approximately to an altitude of 80 km.

3.1.2 Parameterization schemes used in the UM

The UM contains different parameterization schemes to handle the sub-grid scale physics (as explained in Chapter 2) and hence to realistically simulate the atmospheric circulation. The physical processes that are parameterized in the UM are given below :

- land-surface interaction
- boundary layer
- large scale cloud and precipitation
- convection
- radiation
- horizontal eddy diffusion
- vertical eddy diffusion and
- GW drag

GW parameterization scheme is the central focus here because this research deals primarily with implementing different GW parameterization schemes in the UM. In the following sections the gravity wave parameterization scheme of the UM is discussed in detail, and the incorporation of the DSP and 'coupled' broad spectrum and monochromatic wave schemes is discussed.

3.2 Gravity wave drag parameterization in the Unified Model

3.2.1 Introduction

As discussed briefly in Chapter 2, the GW drag parameterization in the UM is based on the assumption that the waves are orographically generated monochromatic. This scheme is based upon the study of *Palmer et al.* (1986), who examined data from aircraft measurements, near-surface wind speed measurements and zonally averaged momentum budget. Based on their results, they proposed a parameterization scheme in which it was assumed that the surface stress was proportional to near-surface wind speed, U_0, static stability N, and to the variance of the sub-grid scale orography σ. The sub-grid scale orography was assumed to be isotropic. The vertically propagating waves were assumed to break depending on a particular Richardson number [$R_i = N^2/\eta^2$, N =static stability, $\eta = \partial U/\partial z$ and U is the mean horizontal wind and z is the thickness of a level in the atmosphere].

On the basis of theoretical studies, *Shutts* (1990), *Milton and Wilson* (1996) and *Gregory et al.* (1998) have proposed some modifications to the scheme to produce low and mid level acceleration on the background wind speed. *Milton and Wilson* (1996) studied its impact on a 5-day forecast using a Numerical Weather Prediction (NWP) model that had a similar configuration to the UM, while *Gregory et al.* (1998) studied its effects on the UM's climate model with 19 vertical levels. The proposed changes over the scheme of *Palmer et al.* (1986) included

- anisotropy in the subgrid-scale orography into the expression for surface GW stress
- low level wave breaking mechanisms such as trapped lee waves and hydraulic jump of waves

Following *Gregory et al.* (1998) and *Webster* (1997) the schemes may be summarized as follows. The basic elements of this scheme are the determination of the surface stress and distribution of the stress through surface column via 'hydraulic jump', 'saturation' and 'trapped lee waves and reflection of hydrostatic waves' regimes.

3.2.2 Determination of gravity wave surface layer

The surface layer is defined as a layer which is raised over sub-grid scale orography and is capable of generating GWs. The depth of surface layer is henceforth calculated using

the following equations.

The top of the layer can be expressed as

$$\hat{h} = min(\sqrt{2}\delta, 750m), \tag{3.1}$$

where δ = root mean square of subgrid-scale variance of topography evaluated from gridded terrian-height data-sets. The bottom of the surface layer is also the top of the blocked layer (if one exists). It is the top of the layer of air going around the mountains and is given by

$$h_b = \hat{h} - 0.985\frac{U}{N}. \tag{3.2}$$

The depth of the model levels (for level k) is calculated as

$$\triangle h_k = (\triangle \Pi)_k \theta_k \frac{c_p}{g}, \tag{3.3}$$

where $\triangle\Pi$ is the difference in exner function and

$$\Pi = (\frac{p}{p_0})^{\kappa}, \tag{3.4}$$

where Π is the exner function and $\kappa = \frac{R}{c_p}$. h_b in equation 3.2 is evaluated using the wind and static stability at level 2. The finite difference form used for the static stability N, at level k is

$$N_k^2 = \frac{(\triangle\Pi)_{k-1/2,k} N_{k+1/2}^2 + (\triangle\Pi)_{k,k+1/2} N_{k-1/2}^2}{(\triangle\Pi)_{k-1/2,k+1/2}} \tag{3.5}$$

$$N_{k+1/2}^2 = \frac{g(\theta_{k+1} - \theta_k)}{\theta_{k+1}\theta_k(\triangle\Pi)_{k,k+1}\frac{C_p}{g}}. \tag{3.6}$$

3.2.3 Calculation of hydrostatic surface stress

The components of the linear hydrostatic stress are given by

$$\tau_{xs} = \frac{\rho_s U_0^3}{\hat{\kappa}\delta^2 N_s}\hat{h_1}\hat{h_2}(\delta_{xx}cos\chi + \delta_{xy}sin\chi) \tag{3.7}$$

$$\tau_{ys} = \frac{\rho_s U_0^3}{\hat{\kappa}\delta^2 N_s}\hat{h_1}\hat{h_2}(\delta_{xy}cos\chi + \delta_{yy}sin\chi). \tag{3.8}$$

Here, ρ_s and N_s are the surface values of the density and static stability, respectively. U_0 is the component of the wind in the direction of the surface stress, $\hat{\kappa}$ is a typical wavelength for the spectrum of GWs being parameterized, χ is the phase of the surface layer wind relative to westerly direction and δ is the standard deviation of orography. δ_{xx}, δ_{xy} and δ_{yy} are the squared gradient of the elevation of the sub-grid scale orography. For example, if $\delta_{xx} = (\triangle h/\triangle x)^2$, where h is height of the sub-grid scale orography dataset, then δ_{xx} is simply the grid-box mean of the square of $\triangle h/\triangle x$. From the above equations, 3.7 and 3.8, it is evident that surface stress is dependent on the degree of anisotropy of the subgrid-scale orography. The values of $\hat{h_1}$ and $\hat{h_2}$ are calculated as

$$\hat{h_1} = \begin{cases} \frac{N\delta}{\alpha U_0} & \text{if} < 1 \\ 1 & \text{otherwise} \end{cases} \tag{3.9}$$

$$\hat{h_2} = \begin{cases} \frac{N\delta}{\beta U_0} & \text{if} < 1 \\ 1 & \text{otherwise} \end{cases} \tag{3.10}$$

where α and β are constants. In the present implementation, α is set at 0.4 and β is set at 1. Values of $\hat{h_1}$ and $\hat{h_2}$ are height dependent and are calculated based on the Froude number, $F_r = N\delta/U_0$.

The terms $\hat{h_1}$, $\hat{h_2}$, α and β are very important because they determine which physical regime is to be invoked (for a given Froude number F_r) for vertical propagation of the waves.

3.2.4 Calculation of hydrostatic drag profile

Hydraulic jump profile

When $F_r \leq \frac{1}{\alpha}$, the waves are dissipated through a 'hydraulic jump' regime. The height of the hydraulic jump layer, H_0, is taken as 3/4 of the mean vertical wavelength of the waves. H_0 is defined as the level where

$$\int_{h_b}^{H_0} \frac{N(z)}{U_0(z)} \geq \frac{3\pi}{2}, \tag{3.11}$$

where h_b is the depth of the blocked layer (defined above).

After the jump height has been diagnosed, the vertical profile of the atmospheric stress can be determined, once a check for the 'critical level' is made. A critical level is the level where orographic GWs dissipate. The critical level is determined by the value of the Richardson number R_i at that level. If R_i falls below a critical value of 0.25, critical level is assumed to have been reached and the waves dissipate at thatlevel. If $u\tau_s < 0$, where u is the wind at that level, then the jump height is lowered to that level.

If a critical level is not found below the jump height, 2/3 of the surface stress is deposited at the jump height. It should be added here that if critical level is found below the jump height, total atmospheric stress is deposited there.

The stress profile below the jump height decreases linearly from the bottom of the surface layer up to the jump height. Above the jump height, for those points where the critical level is not found below the jump height, the remaining stress is deposited by 'saturation mechanism', as discussed in the following section.

Linear hydrostatic profile or saturation mechanism

For the points where $F_r > \frac{1}{\alpha}$, and for hydraulic jump points above their jump height, the vertical profile of atmospheric stress is determined by using the 'saturation mechanism'. At each layer boundary, maximum stress or the 'critical stress' that can be supported by the background wind is calculated according to R_i at that level.

The components of the critical stress can be written as

$$\tau_{xc} = \frac{\rho U_0^3}{\hat{\kappa}\delta^2 N}(\delta_{xx}cos\chi + \delta_{xy}sin\chi)(\frac{\alpha}{\beta}) \tag{3.12}$$

$$\tau_{yc} = \frac{\rho U_0^3}{\hat{\kappa}\delta^2 N}(\delta_{xy}cos\chi + \delta_{yy}sin\chi)(\frac{\alpha}{\beta}). \tag{3.13}$$

If the 'critical stress' exceeds the stress in the layer below, there is no forcing between the two layers. However, when the stress carried upward exceeds the critical stress, then it is assumed that the wave is unstable and it breaks. The difference in stress between two consecutive levels for the 'hydrostatic regime', $\delta\tau$, equates to a drag or acceleration on the large scale flow given by the following equation

$$X_{saturation} = \triangle u/\triangle t = g(\triangle\tau/\triangle p) \tag{3.14}$$

Trapped lee waves and the reflection of the hydrostatic waves

This regime is invoked when $F_\tau > \frac{1}{\alpha}$. The generation of short wavelength non-hydrostatic lee waves and reflection of hydrostatic GWs at the tropopause are assumed to be caused by abrupt changes in the vertical profile of a term called the Scorer parameter, l,

$$l = \sqrt{\frac{N^2}{U^2} - \frac{1}{U}\frac{\delta^2 U}{\delta z^2}} \tag{3.15}$$

To calculate the GW stress for trapped lee waves and transmission coefficient for reflected hydrostatic waves, the atmospheric column is split into two halves of equal depth. This involves finding the optimum height L of the layer interface for the trapped lee wave modes. The optimum height L is determined such that it satisfies the following equation

$$\frac{\alpha_l\sqrt{l_1^2 - l_2^2}L}{\sqrt{1 + \alpha_l^2 tan^{-1}(\alpha_l)}} + 1 = 0, \tag{3.16}$$

where l_1 is the mean Scorer parameter of the bottom layer and l_2 is the mean Scorer parameter for the top layer, $\tan(\alpha_l) = \tan^{-1}(m_1 L) = -(m_1/m_2)$, m_1 is the vertical wavenumber of the trapped lee waves in the bottom layer and m_2 is the inverse decay rate of the trapped lee waves in the top layer. Once the height L (the layer interface for the trapped lee wave) is found, the trapped lee wave surface stress, $\tau_{s_{lee}}$, is calculated and added to already determined surface stress values in equations 3.7 and 3.8.

The waves are dissipated as follows. The momentum flux at the layer interface L is

determined first by the following expression

$$\frac{\alpha_l^2 l_2^2}{(l_1^2 + \alpha_l^2 l_2^2)(ML + 1)}, \tag{3.17}$$

where $M^2 = \frac{(l_1^2 - l_2^2)}{(\alpha_l^2 + 1)}$. The lee-wave surface stress linearly reduces to the value at L and the remaining stress is again reduced linearly at a rate of $(1/m_2)$ up to the top of the upper layer. The reduction in stress $(\delta\tau)$ is used for the calculation of drag due to lee waves with the following equation

$$X_{lee} = \triangle u / \triangle t = g(\triangle\tau / \triangle p). \tag{3.18}$$

To determine the reflection of hydrostatic waves, a 'transmission coefficient' is calculated. The calculation of the vertical transmission coefficient is done by splitting the atmospheric column again from the ground up to the tropopause into two layers of equal thickness. The transmission coefficient T is given by

$$T = \frac{2 l_1 l_2}{l_1^2 + l_2^2 + (l_1^2 - l_2^2) cos(2 l_1 L_t)}, \tag{3.19}$$

where H_t is the height above the ground of the interface of the two layers. In the present model, the transmission coefficient is used only to reduce the GW stress due to internal reflection.

The acceleration due to different regimes, $X_{Saturation}$ and X_{lee}, are added together at each layer and the total acceleration on the background wind at each layer is calculated.

3.2.5 Rayleigh friction in the Unified Model

It has been stated by *Gregory et al.* (1998) and *Swinbank et al.* (1998) that the orographically induced GW drag scheme did not produce the expected results above a certain height. Hence, to reproduce physically realistic dynamics of the middle atmosphere, the orographic GW drag scheme is replaced by a Rayleigh friction above approximately 25 to 27 km in the UM. The Rayleigh friction applies an acceleration in the lower mesosphere such that it provides sufficient descent of the upper stratosphere over the poles. The GW acceleration, $X_{Rayleigh}$, within the Rayleigh friction scheme is given by

$$X_{Rayleigh} = [\frac{(z - z_0)}{(z_1 - z_0)}]^4 \times D_1, z \geq z_0 \tag{3.20}$$

where, $z_0 = 36$ km, $z_1 = 80$ km and $D_1 = 1/1.5$ days. The above equation suggests that between approximately 27km (20 hPa) and 36 km (5 hPa), no GW acceleration is applied. Figure 3.1 shows the implementation of the *original* in the UM with a flow-chart.

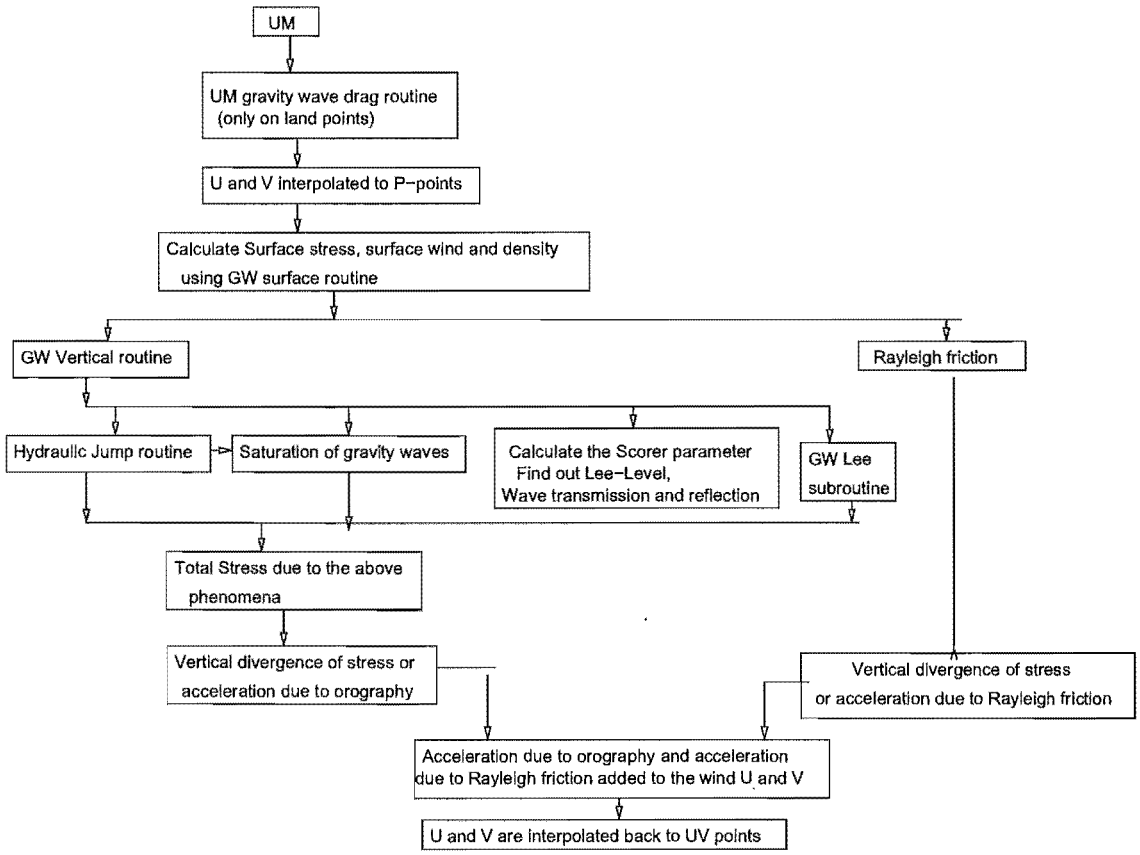

Figure 3.1: Flow chart of the UM's *original* parameterization scheme.

It has been suggested by *Gregory et al.* (1998) that the orographic waves are overly emphasized in the scheme to provide damping on the upper-level flow of the mid-latitudes. It was possible that other sources of GWs could also play a crucial role in the dynamical processes of the model's atmosphere and there was a necessity for further refinement of the scheme.

Therefore, as a part of this study, the DSP scheme and coupled interactive broad spectrum and monochromatic GW schemes, (*Hines*, 1997a,b), have been incorporated into the UM.

3.3 Incorporation of DSP scheme in the Unified Model

The DSP scheme has already been discussed in Chapter 2 of this thesis. A detailed mathematical description along with the technicalities of implementation of this scheme in the UM is provided in this section.

DSP scheme (*Hines* (1997a) and *Hines* (1997b)) is based on the assumption that gravity waves have a continuous spectrum. At a certain initial height, a GW spectrum of horizontal winds is assumed to be a function of vertical wave number m, which terminates at some high wavenumber known as the cutoff wavenumber m_c.

The initial spectrum is assumed to be of sufficiently weak intensity that the waves can be assumed to be linear in nature. The intensity of the waves grows exponentially with height. When the 'root mean square' (RMS) strength of the GW-induced wind σ, becomes comparable to the smallest horizontal phase speed, given by N/m_c, the linearity and the non-interacting behaviour of the waves breaks down and nonlinearity comes into play. Nonlinear effects resulting from horizontal advection alter the shape of the spectrum and form the m^{-3} tail. If the tail becomes sufficiently long and extends beyond some maximum value m_M, then all waves with $m > m_M$ are assumed to be completely dissipated as a result of the critical level filtering by GW induced horizontal winds.

The parameterization is constructed by first discretizing the spectrum into J horizontal azimuths (value of J should be minimum 4 for two-dimensional models and 8 for three-dimensional models, (*Hines*, 1997a)) and assuming a separable horizontal wind power spectrum in each azimuth. The initial spectrum for the j^{th} azimuth can be expressed as

$$M_{ji}(m_i) = (s+1)m_{ji}^{(-s-1)}m_i^s, \tag{3.21}$$

where s is positive and assumed to be 1 and M_{ji} is assumed to vanish for all $m > m_{ji}$.

The square of the horizontal wind variance σ_j resulting from waves in the j^{th} azimuth can be expressed as

$$\hat{\sigma_j^2}(z) = \hat{\sigma_{ji}^2}\frac{\rho_i}{\rho}\int_{m_m}^{m_M} M_j(m)dm, \tag{3.22}$$

where m_m is a minimum vertical wave number and m_M is a maximum vertical wave number. The horizontal background wind gives rise to an azimuthally varying vertical wave number m_{ji}, also known as the initial 'cut-off' vertical wave number, expressed as

$$m_{ji} = N_i(\Phi_1\sigma_{ji} + \Phi_2\sigma_{ji})^{-1}. \tag{3.23}$$

The azimuthally varying vertical wave number m_j decreases with height along with M_j. The decrease in M_j can give rise to momentum deposition. Hence the values of M_j and m_j need to be related at a given height to the corresponding values at the initial height.

To achieve this, an individual GW in the spectrum is expressed with a dispersion equation

$$Nm^{-1} = \Omega h^{-1}, \tag{3.24}$$

where h is the horizontal wave number, N is the static stability and Ω is the local intrinsic frequency. For a wave with intrinsic propagation into the j^{th} azimuth, the ground-based frequency, ω, is Doppler-shifted from the intrinsic frequency by

$$\omega h^{-1} = \Omega h^{-1} + U_j + u_j = Nm^{-1} + U_j + u_j, \tag{3.25}$$

where U_j is the horizontal background wind velocity at the j^{th} azimuth and u_j is the superimposed wave induced coordinate.

Assuming that $|U_{ji}| \gg |u_{ji}|$ (where U_{ji} and u_{ji} are the initial horizontal background wind velocity and initial superimposed wave induced velocity, respectively) the cut-off vertical wave number at a given height is calculated as

$$m_j = N_i[Nm_M^{-1} + U_j - U_{ji} + \Phi_1\sigma_j]^{-1}, \tag{3.26}$$

where $U_j \approx \Phi_1\sigma_j$, $Nm_M^{-1} \approx \Phi_2\sigma$, σ_j is the total horizontal wind variance in the j^{th} azimuth, $\sigma^2 = \Sigma_{j=1}^{J}\hat{\sigma_j^2}$, Φ_1 is the first fudge factor ($1.2 \leq \Phi_1 \leq 1.9$) and Φ_2 is the second fudge factor ($0.1 \leq \Phi_1 \leq 0.4$). Φ_1 and Φ_2 are constants and their values do not change with height.

Once the value for m_j is calculated, and the horizontal wind variance resulting from waves in the j^{th} direction is calculated as

$$\hat{\sigma_j^2}(z) = \hat{\sigma_{ij}^2}\frac{\rho_i}{\rho}\frac{N}{N_i^{-1}}I_j, \tag{3.27}$$

where

$$I_j = \int_0^{m_j} M_{ji}(m_i)[1 - N_i^{-1}(U_j - U_{ji})m_i]^{-1} dm_i. \tag{3.28}$$

The vertical flux density (flux per unit area) of horizontal momentum at the j^{th} azimuth is thus calculated as

$$\hat{\tau}_j = \rho_i \hat{\sigma}_{ij}^2 k_j \int_0^{m_j} M_{ji} m_i^{-1} dm_i. \tag{3.29}$$

At each grid point, the vertical flux densities of eastward (τ_E) and northward (τ_N) momentum are given by

$$\tau_E = \Sigma_{j=1}^{J} \cos\alpha_j \hat{F}_j \tag{3.30}$$

and

$$\tau_N = \Sigma_{j=1}^{J} \sin\alpha_j \hat{F}_j. \tag{3.31}$$

The rate of intrinsic energy deposition per unit volume is, therefore, expressed as

$$dE/dt = -(N/m)\Sigma_{j=1}^{J}(d\hat{\tau}_j/dz). \tag{3.32}$$

In this study, the DSP scheme has been incorporated into the UM. The DSP scheme can be further extended to facilitate 'coupling' of broad spectrum waves with monochromatic or orographically induced GWs, which is discussed in the next section.

Initial implementations of the DSP scheme have been carried out by a number of people, for example *Manzini and McFarlane* (1998), *Mayr et al.* (1998a) and *Lawrence* (1997a). *Lawrence* (1997a) implemented the scheme in the Stratosphere Mesosphere Model (SMM), which is a mechanistic model without a tropopshere. That scheme has been extensively modified and implemented in the UM.

The orographically-induced GW scheme of the UM, in the current implementation, works from ground to 25−27 km in the UM and the DSP scheme is set to operate from ground to the top of the model. Unlike the UM's orographic GW parameterization which produces momentum flux only on the grid points representing land, the DSP scheme is applied over the entire globe, that is, at all the grid points. It should be noted here that the inclusion of the DSP scheme in the UM has obviated the need to include the Rayleigh friction scheme.

The monochromatic waves produced by the model's orography and the broad spectrum waves in the DSP scheme do not interact with each other and the waves break down according to their characteristic physical regimes. The schemes both independently calculate momentum flux and acceleration. The acceleration produced by orographic waves

and the DSP scheme are added at each layer and the total acceleration on the background wind is determined. Although the phenomenon of diminution of momentum flux continues up to the altitude of the mesopause, here the overall momentum flux is dumped at 80 km (the model's upper most level) to stimulate the residual mean circulation, (*Haynes et al.*, 1991). The incorporation of the DSP scheme in the UM is shown in figure 3.2 with a flow chart.

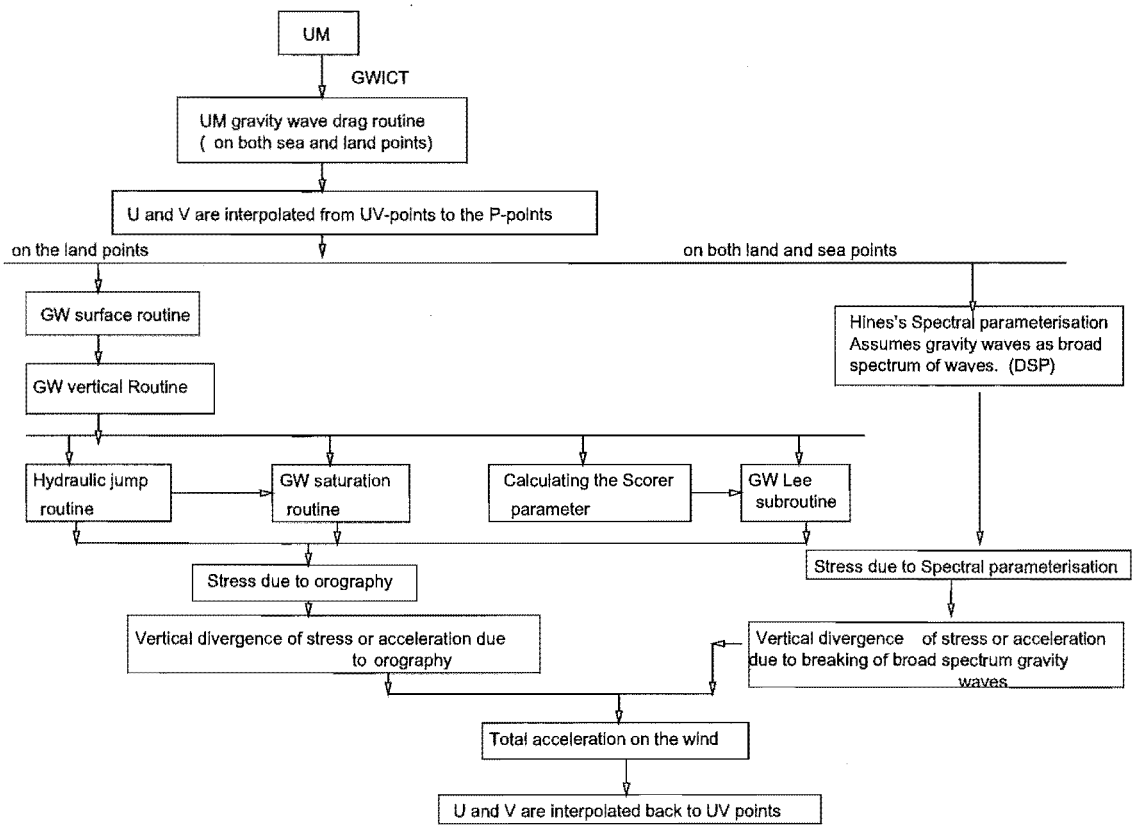

Figure 3.2: Flow chart of DSP scheme in the UM.

3.4 Incorporation of coupled broad spectrum and monochromatic gravity wave scheme in the UM

An overview of the coupled monochromatic and broad spectrum wave scheme has also been given in Chapter 2. In this section a mathematical description of the scheme and details of its implementation in the UM are provided.

In the DSP scheme, it is assumed that GWs comprise a broad spectrum of waves. However, an observational study using radar by *Eckermann and Hocking* (1989) suggested that a GW field might be a mixture of quasi-monochromatic (QMC) and broad spectrum waves. It is, therefore, important to study the coupling of those broad spectrum and QMC waves that are able to interact with each other. The theory underlying the parameterization is described as follows (*Hines*, 1997b).

A single QMC wave is constrained to propagate into a certain single azimuth, Q, that can be identified in the intrinsic, wind-borne frame of reference. The QMC wave at an initial height is assumed to have a horizontal wavenumber k_Q that it retains at all overlying heights. It also has an initial vertical wavenumber m_i that is subject to change under certain conditions.

Its intensity is characterized by its initial-height horizontal wind variance, $\hat{\sigma}^2_{Qi}$, and its initial vertical flux density of horizontal momentum ($\hat{F}_{Qi}$), which is directed into the Q azimuth and is given by

$$\hat{F}_{Qi} = \rho_i \hat{\sigma}^2_{Qi} k_Q m_i^{-1}. \tag{3.33}$$

Upward propagating waves in the absence of any dissipation have a wind variance of

$$\hat{\sigma}^2_Q = \rho^{-1}\rho_i N N_i^{-1} \hat{\sigma}^2_{Qi}[1 + N_i^{-1}(U_{Qi} - U_Q)m_i]^{-1}. \tag{3.34}$$

It is assumed that the wind or shear variance produced by the QMC waves is $N^2/3n_Q$, where n_Q is the number of waves included in some grid point of a model. It is also assumed that the Doppler shifting of the broad spectrum waves has an effect on the propagation of QMC waves. When the QMC waves start dissipating, the wind variance is given by

$$\hat{\sigma}^2_{QM} = (3n_Q)^{-1}[N_i m_i^{-1} + U_{Qi} - U_Q - \Phi_1 \tilde{\sigma}_Q]^2, \tag{3.35}$$

where

$$\tilde{\sigma}_Q = \sum_{j=1}^{J} \hat{\sigma}^2_j \cos^2[\alpha_j - \alpha_Q]. \tag{3.36}$$

The term $\hat{\sigma}^2_j$ is the horizontal wind variance associated with waves of the background spectrum propagating in the j^{th} azimuth.

When the value of $\hat{\sigma}^2_{QM}$ decreases to zero with an increase in height, the monochromatic waves are destroyed. It should also be noted that the presence of monochromatic waves

predisposes the atmosphere to instability, so the broad background spectra need not extend in vertical wave number m as far as before to induce instability. The maximum wave number m_M is reduced from $N(\Phi_2\sigma_h)^{-1}$ by a factor of $\exp(\pi N^{-1}\sum_Q[m_Q^2\hat{\sigma}_Q^2])$. The formulation and the analysis of the broad spectrum of waves can be performed as discussed before in the context of DSP.

The momentum flux density that is deposited on the background wind as the waves break is given by

$$\hat{\tau}_Q = -\rho N^{-1}\hat{\sigma}_Q^2 k_Q U_Q. \tag{3.37}$$

The flux density is separated into eastward ($\cos\alpha_Q$) and northward ($\sin\alpha_Q$) components, then combined with the flux densities contributed by the broad spectrum of waves. Using this formulation, *Hines* (1997b) showed that the QMC and broad spectrum of waves are interactive.

The implementation used by *Lawrence* (1997a) and extended by *Osprey* (2001) is used here to include coupling between the DSP and the monochromatic waves. This scheme was primarily developed to be implemented in the Stratosphere Mesosphere Model (SMM) *Lawrence* (1997a), although *Osprey* (2001) used off-line tropospheric analyses to calculate monochromatic wave amplitudes to simulate middle atmospheric circulations. This scheme has also been modified significantly in order to be incorporated in the UM, as discussed below.

The contribution of the monochromatic part in the broad spectrum waves is calculated from the UM's 'hydrostatic surface stress' regime. Information regarding momentum flux, phase and vertical wave number associated with the monochromatic wave are included in the broad spectrum.

If a 'hydraulic jump' regime is encountered, 2/3 of the momentum flux of the monochromatic waves is deposited at the jump height. The remaining spectrum follows the criteria for propagation and obliteration of 'coupled interactive' broad spectrum and monochromatic waves. The major modifications in this scheme are the exclusion of the Rayleigh friction scheme, inclusion of monochromatic waves in the broad spectrum and replacement of the 'saturation' regime of wave breaking with 'coupled interactive' regime.

The contribution from lee waves is not included in the broad spectrum waves for the following reasons. When a lee-wave regime is identified in the UM, an extra 'lee wave

surface stress' is added to the already calculated 'hydrostatic surface stress', which might change the initial phase of the stress at a later stage. However, for the operation of the coupled-interactive scheme, the initial stress and the phase of a monochromatic wave has to be pre-defined prior to the simulation. Also, according to the lee wave regime, the lee waves are totally dissipated by the time they reach the top of the upper layer of the level in which they are detected. The upper layer is obtained by splitting the atmosphere in two parts with an interface L. This implies that there are no remaining lee waves above the upper layer which can be carried upwards with broad spectrum waves.

Considering all the above features of the lee-wave regime it was found that coupling the lee waves with the broad-spectrum waves would complicate the coupled-interactive scheme without significantly affecting the overall parameterization. Hence, the waves from the lee wave regime are not included in coupled-interactive regime. However, the lee wave regime works separately in the model and the acceleration produced due to dissipating lee waves is added to the acceleration from the coupled interactive regime to calculate the total acceleration on the background wind. Incorporation of the coupled interactive broad spectrum and monochromatic waves in the UM is shown with a flow chart in figure 3.3.

3.5 Summary

Incorporation of the UM's orographically induced GW parameterization scheme, the DSP scheme and 'coupled interactive' monochromatic and broad spectrum waves scheme are discussed in this chapter.

This scheme works only on the grid points representing land, up to a height of 25 to 27 km in the UM. Above that height a Rayleigh friction scheme is used to damp the stratospheric jets.

The UM's orographically induced GW scheme aims at determining the surface stress and vertical propagation of the gravity waves through different physical regimes such as, hydraulic jump, saturation and trapped lee waves. These regimes are invoked based on the value of the Froude number, F_r.

The DSP scheme has been customized so that it works on all the grid points and also

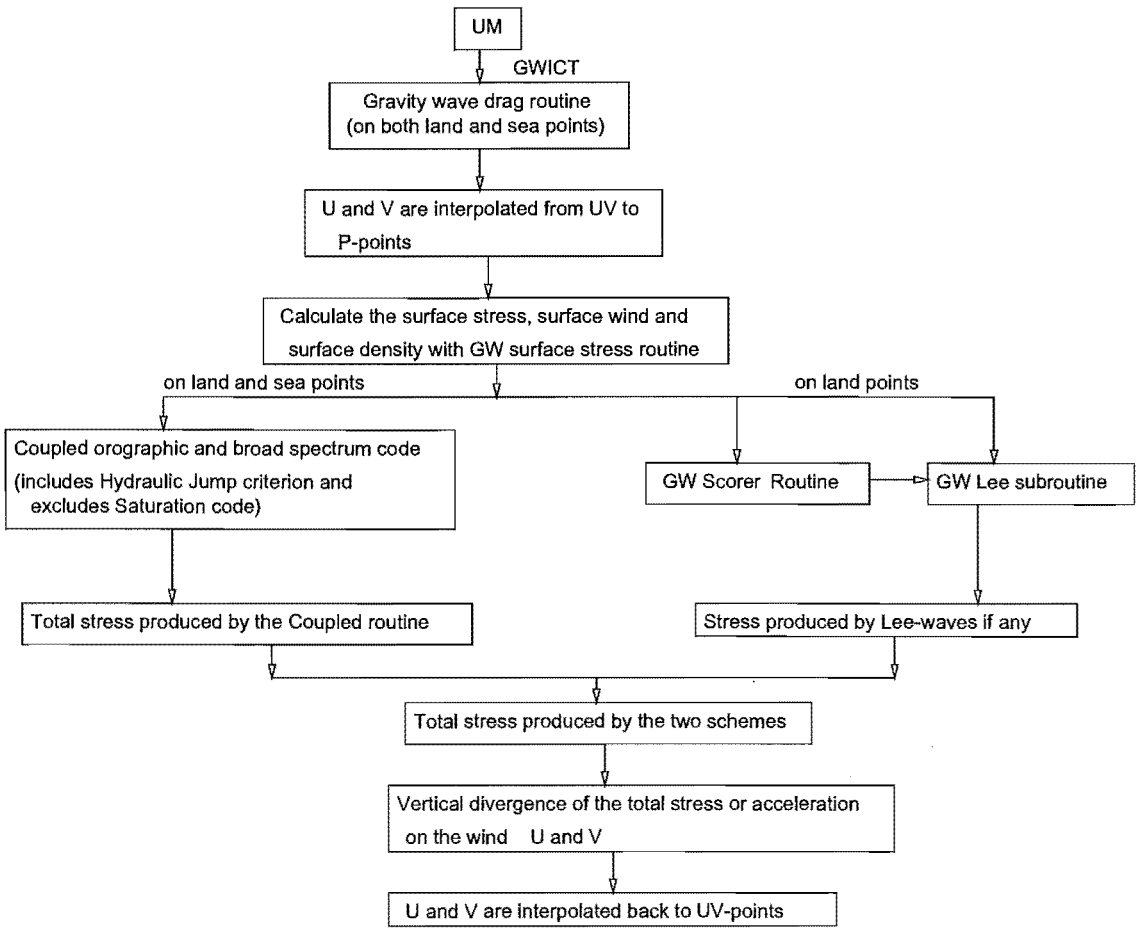

Figure 3.3: Flow chart of coupled monochromatic and broad spectrum GWs in the UM.

extends up to the top of the model. The DSP scheme and the orographically excited GW scheme do not interact with each other and independently produce acceleration on the background wind. The Rayleigh friction scheme is not needed in the UM with the incorporation of the DSP scheme.

The DSP scheme has been further extended to couple orographically induced monochromatic waves with the broad spectrum waves. As a consequence, the atmosphere is predisposed to instability and the corresponding parameters in the DSP have been changed accordingly. However, the contribution from the trapped lee waves is not included in the regimes, as lee waves are entirely dissipated inside the layer they are trapped in.

In the next chapter, case studies based on the DSP and coupled interactive schemes are presented on the basis of varying physical parameters. The case studies were carried with the aid of an off-line test bed based on the premises of the UM, to gain insight into the performance of the DSP and coupled interactive schemes in the UM.

Chapter 4

Comparative Study of the UM's Original GWD with the New Schemes in a Single Column Test bed

4.1 Introduction

In this chapter, implementation of the the DSP and 'coupled interactive' broad spectrum and monochromatic (CIBM) wave schemes in a single column test bed based on the UM's architecture is discussed. In addition to that, UM's orographic GWD, DSP and CIBM schemes are compared with the UM's original GWD scheme. The simplicity of the test bed offers the freedom to change various parameters within the schemes for a better understanding of the behaviour of GW propagation modelled on different physical regimes. Results from the test bed are analyzed to compare the effect of different launching heights and varied sources of GW on model simulations.

The chapter is arranged in the following order. A brief discussion of the test bed is provided at the beginning, followed by a design of the experiments. Results are then presented for experiments using varying horizontal wind speeds and GW launching heights with the DSP scheme. Results are then presented for the various comparative studies. The chapter is concluded with the summary of results.

4.2 The single-column test bed

The theory and implementation of the UM's original GWD scheme, DSP scheme and the CIBM scheme are discussed in Chapters 2 and 3.

Prior to implementing the new schemes in the UM, a simple test bed was developed so that the framework of each scheme could be tested without having to deal with the UM's user interface and code modification suite. With the aid of an off-line test bed, the evolution and then dissipation of the spectral and coupled waves can be studied in detail. These results can then be used to interpret the results off full UM simulations with the

new schemes. It should be mentioned here that the UM, being a climate model, has many parameterization schemes which makes the operation of the model complex. Because of its complexity, any additional parameterization scheme can induce chaotic response to the model results which may not be easily traced and corrected.

In addition to providing a useful tool for code development, construction of the test bed is also an important step toward understanding the UM architecture. The test bed, like the original UM, has a staggered Arakawa-B horizontal grid as shown in figure 4.1, and like the original model, uses a hybrid pressure-sigma coordinates with 55 levels.

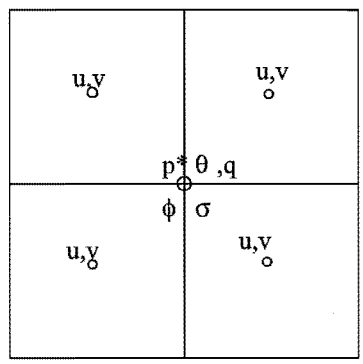

Figure 4.1: Grid structure to show the positions of the variables

In the present work, a single-column test bed was used to evaluate new GW parameterization schemes; therefore, only a selected part of the model, which performs this operation was incorporated in the test bed. In this framework, the response of a GW parameterization to arbitrary input parameters, such as, the background model fields and local topography, can be studied with a temporal resolution equal to the model's initial time step.

To carry out idealized test cases, realistic values of zonal and meridional winds, potential temperature and specific humidity were used in the test bed. A description of the experiments is given below.

4.3 Design of experiments

The experiments are designed to compare the new GWD schemes with the UM's original GWD scheme. The original GWD scheme of the UM (henceforth *CTL*) has an orographic

GWD scheme up to an altitude of 25 km and from 36 km and above Rayleigh friction is used. Implementation of this scheme has been discussed in Chapter 3.

The first experiment compares the behaviour of UM's orographic scheme alone (henceforth *ORO*) with *CTL*. Orography is represented at one grid point of the test-bed by using information based on UM's standard orographic data. A mountain height of 5500 m was chosen for the experiment.

Next, DSP scheme is incorporated in the test-bed. According to the available literature, for example *Hirota* (1996), the primary sources of GWs are believed to be in the troposphere. To elucidate the effects of tropospheric filtering of broad spectrum GW using the DSP scheme, two GW configurations are presented, which differ in their launching heights for broad spectrum waves. The configurations are referred to as:

- *SUR: waves launched from the surface,*
- *TRO: waves launched from the tropopause (*200 *hpa or approximately* 12 *km from the surface).*

In the third experiment, *SUR* and *ORO* are combined together and their effect is compared with *CTL*. The fourth experiment comprises a comparative study of *SUR* and *CTL*.

To study the importance of orographically induced GWs and their interaction with the broad spectrum waves the CIBM scheme is tested in the presence of mountains. These are introduced to two grid points. The following two configurations were constructed with differing mountain heights:

- *HIM: High mountains (elevation approximately* 5000 *to* 5500 *m),*
- *LOM: Low mountains (elevation approximately* 700 *to* 800 *m)*

The fifth experiment presents a comparison between *HIM* and *CTL*. Lastly, *HIM* and *SUR* are compared and contrasted for both summer and winter wind profiles.

The total RMS wind speed (σ_T) associated with the launching height for *SUR* and *TRO* were set at 1.414 m/s and 2.0 m/s respectively, which correspond to ${\sigma_T}^2 = 2$ and ${\sigma_T}^2 = 4$. These values were calculated such that the values of σ_T are approximately equal at 200 hpa for both cases [1]. For *HIM* and *LOM* the value of σ_T is set at 1.414 m/s.

[1] σ_T increases as density decreases (*Hines*, 1997a).

Other parameters within the DSP and CIBM schemes that were kept fixed over the four cases are: horizontal wave number of broad spectrum GWs given by $2\pi/(900$ km), minimum vertical wave number of the spectra, $m_{min} = 1/3000$ m, the adjustable parameters $\phi_1 = 1.5$ and $\phi_2 = 0.4$.

Three different zonal wind patterns; a typical QBO profile on the tropics, mid-latitude summer and mid-latitude winter are used for the study (figure 4.2). The meridional wind, BV frequency, and the temperature profiles were kept constant for all cases (*Osprey and Lawrence*, 2001), as shown in figure 4.3.

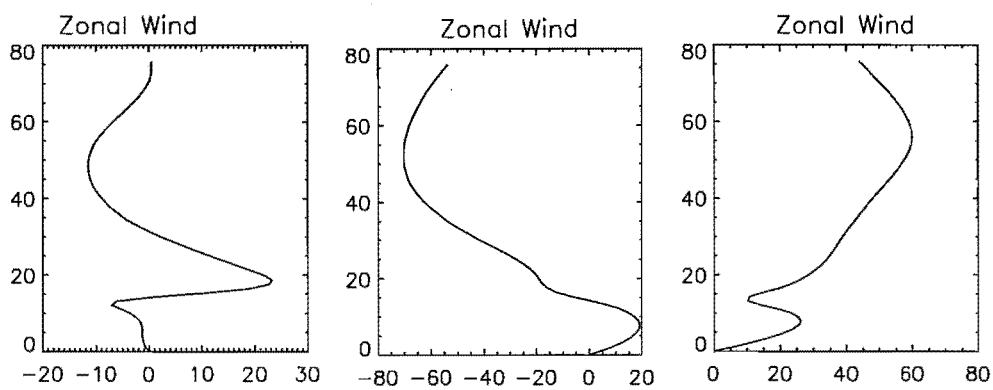

Figure 4.2: Standard profiles of tropical, winter and summer hemisphere wind profiles used in the test bed (m/s).

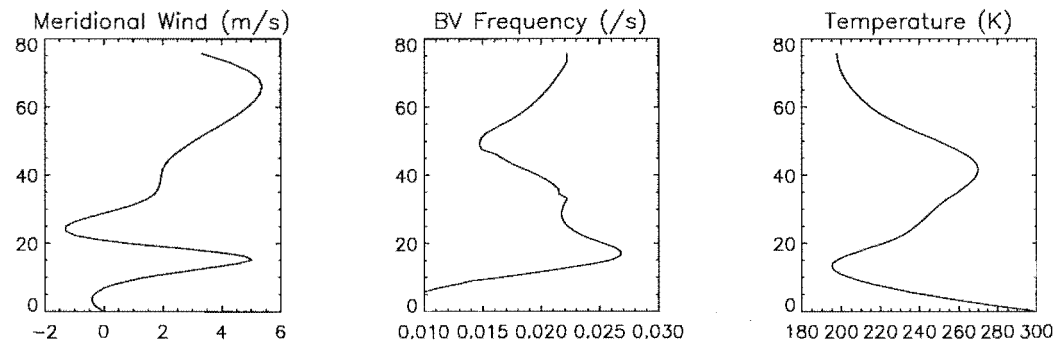

Figure 4.3: Standard profiles of meridional wind, temperature and BV frequency as a function of height (km).

It should also be mentioned here that to capture the effects of residual mean circulation or diabatic circulation in the mesosphere, the test bed was configured such that entire

momentum flux due to GWs was deposited at the top-most level of the model.

4.4 Results and Discussion

4.4.1 Effects of orography

To study the effect of orography only *ORO* and *CTL* configurations are compared with each other. Orography is represented in one grid point in both the configurations. Zonal wind profile chosen for this experiment is winter zonal wind profile, because effect of orography is found to be more magnified during winter than summer (*Gregory et al.*, 1998).

Figure 4.4 shows momentum flux or stress due to *ORO* and *CTL*. The orographic GWD scheme in the UM extends only up to an altitude of approximately 25 km and that is shown in figure 4.4. The direction of *ORO* momentum flux depends upon the gradient of orography and is positive in this case. It reduces slowly below the tropopause and above the tropopause the rate of reduction is faster. However, there is no momentum flux due to Rayleigh friction in *CTL*. Therefore, only momentum flux due to orography is represented in this case.

The *ORO* shows a significant amount of drag at tropopause (-3 m/s/day). This value agrees with the one in (*Lilly et al.*, 1982). The drag due to Rayleigh friction in the UM is calculated as;
$X = -(z - z_0)^4/(z_1 - z_0)^4 * D_1 * U$,
where, z_0 = 36 km, z_1 = 80 km, D_1 = 1/1.5 days and U = zonal wind. It should also be mentioned here that there is no GWD between 25 to 36 km in the UM. This is shown in the *CTL* drag. The drag in *CTL* is due to orography up to 25 km and above 36 km it is due to Rayleigh friction. The value in the upper stratosphere and lower mesosphere is around -40 m/s/day. Hence with only orography, *ORO* the zonal wind in the troposphere and the lower stratosphere is damped whereas with the inclusion of Rayleigh friction, *CTL*, the damping is extended to the mesosphere.

4.4.2 Tropospheric filtering of broad spectrum GW

Figure 4.5 shows a zonal wind profile depicting a typical QBO signal, zonal momentum flux and acceleration due to momentum flux for a GW spectrum launched at the ground (*SUR*). A strong deposition of momentum flux in the troposphere is evident which is

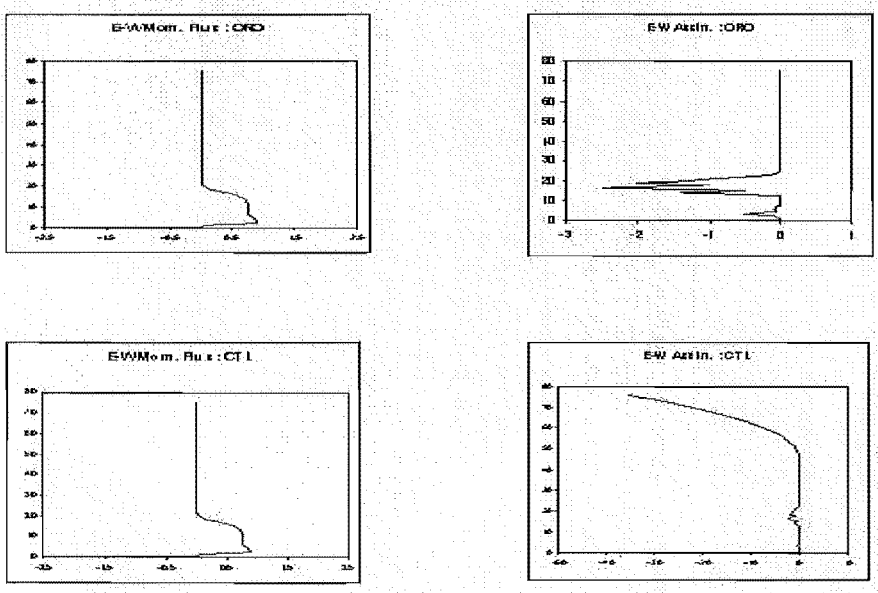

Figure 4.4: Momentum flux (N/m^2) and acceleration (m/s/day) for *ORO* (above) and CTL (below).

caused by the filtering of the spectrum by the tropospheric wind. As the wind shear changes in the lower stratosphere (at an altitude of approximately 15 to 20 km), the part of spectrum which is not in phase with it is filtered through and the remaining momentum flux is gradually deposited at higher altitudes.

The dissipation of waves in the troposphere is not evident from the zonal acceleration (figure 4.5) due to the relatively higher density of the atmosphere[2]. However, a small spike in the zonal acceleration profile can be observed at approximately 15 km altitude. It should also be noticed from the zonal acceleration profile that the spectrum starts dissipating at about 55 km altitude. A sudden change in the zonal acceleration can be observed at the top-most layer due to the deposition of momentum flux in that region.

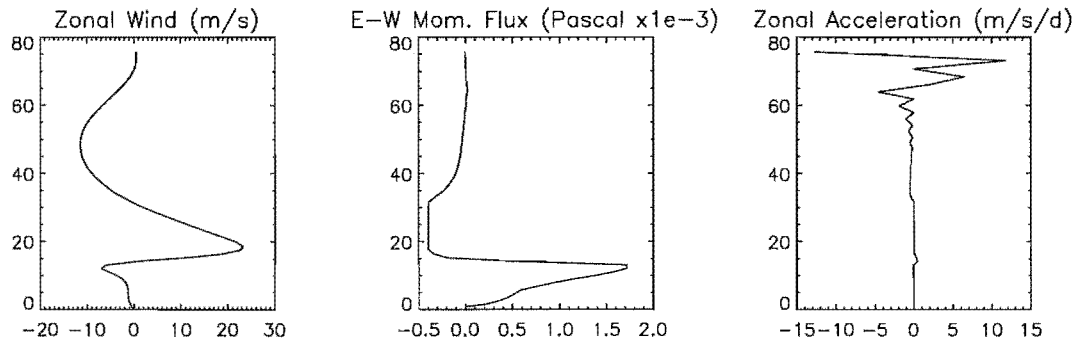

Figure 4.5: Zonal wind (m/s), momentum flux*10^{-3} (N/m^2) and acceleration (m/s/day) when broad spectrum waves are launched from the ground.

It is obvious from figure 4.6 that the spectrum launched from the tropopause (*TRO*) does not get filtered through the tropospheric wind and hence there is no instability in the spectrum at the tropopause. The spectrum, in this case, gets filtered through the stratosphere where a strong deposition of negative momentum flux can be observed. The rest of the spectrum is dissipated in the mesosphere. The zonal acceleration profile does not show any spike at the tropopause and indicates a stable spectrum, as evidenced by the

[2]The zonal acceleration depends upon the density of the atmosphere which decreases exponentially with increasing altitude, as shown in the following equation.

$$\frac{DF}{Dz_{iz}} = \frac{F_{iz} - F_{iz-1}}{\rho_{iz} \times dz} \tag{4.1}$$

where $\frac{D\tau}{Dz}$ is the vertical divergence of the horizontal momentum flux, τ_{iz} and τ_{iz-1} are the momentum fluxes at consecutive levels, ρ_{iz} is the density of air at that level and dz is the difference in altitude between the two levels.

lack of significant change in its value up to the stratopause. As the rest of the spectrum is forced to dissipate at the top layer of the model, a strong zonal acceleration can be observed at that point which is larger than that of *SUR*.

From the above experiment it can be stated that tropospheric filtering of the broad spectrum of waves reduces the strength of zonal momentum flux in the stratosphere, as reported by *Manzini and McFarlane* (1998). The zonal acceleration in *TRO* is much larger than that of *SUR*, figure 4.6.

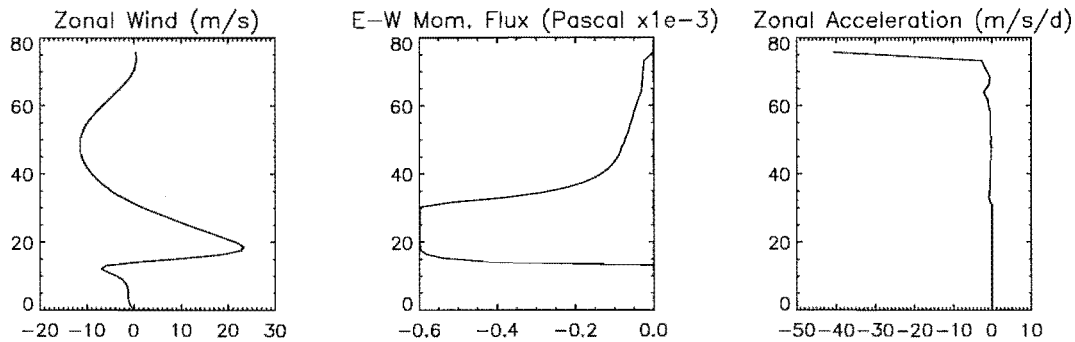

Figure 4.6: Zonal wind (m/s), momentum flux*10^{-3} (N/m^2) and acceleration (m/s/day) when waves are launched at tropopause.

The *SUR* and *TRO* configurations were also applied to typical summer and winter hemisphere mid-latitude wind profiles. The results, presented in detail in *Appendix D*, show that dissipation of waves in the *SUR* configuration commences at a lower altitude than in *TRO*. Hence, the GW acceleration in the top-most model layer is larger in the case of *TRO* configuration when compared to *SUR*.

The results from the above experiments indicate that tropospheric filtering of a broad spectrum of GWs leads to a spectral imbalance within the tropopause which results in the breaking down of the GW spectrum at a much lower altitude in the *SUR* configuration as compared to *TRO*. The differences in the process of wave dissipation effectively changes the GW acceleration in the upper atmosphere (*Manzini and McFarlane*, 1998).

These results can also be analyzed in terms of 'vertical wave number' which is a key factor in the DSP. As discussed in Chapter 2, the broad spectrum of waves is equally divided into J azimuths with $J = 8$ for a three-dimensional model such as the UM. Hence, $J = 8$

in this simulation and the m_j values vary for each (j) azimuth. At each height the cut-off wave number for j^{th} azimuth is given by

$$m_{cj} = \frac{N_i}{\phi_1 \sigma_j + \phi_2 \sigma_t + U_j - U_{ji}}, \tag{4.2}$$

where j is the azimuthal direction of the isotropic wave spectrum, σ_j is the total horizontal wind variance in the j^{th} azimuth, σ_t is the total RMS wind variance, and ϕ_1 and ϕ_2 are constants. U_j is the j^{th} component of the background wind and U_{ji} is its value at the initial height. m_{cj} is constrained to be positive and non-increasing with height.

The above equation implies that m_{cj} diminishes as any of σ_j, σ_t or $U_j - U_{ji}$ increases with the increase in height. The values of both σ_j and σ_t will be expected to rise with height as the density decreases. It should also be mentioned here that the value of $U_j - U_{ji}$ is zero at the initial level. Thus, the momentum flux will generally diminish with increasing altitude as shown by the following equation

$$\tau_j = \rho_i \sigma_t^2 k m_j^{-1}, \tag{4.3}$$

where τ_j is the momentum flux at the j^{th} azimuth, σ_t^2 is the square of the total wind variance, k is the horizontal wave number of the waves and m_j is the vertical wave number at the j^{th} azimuth. Figures 4.7 and 4.8 show the changes in σ_t, m_j and the corresponding value of τ_j with height, for the *SUR* and *TRO* configurations, respectively. Figure 4.7 shows σ_t, m_j and τ_j at 0° and at 180° which is the complementary angle, for spectrum launched from the ground, *SUR*.

In the *SUR* configuration (figure 4.7), σ_t increases with increasing altitude; however, its uniform increase is damped at around 60 km altitude indicating the location where the spectrum commences to dissipate. The value of m_j at 0° (the first azimuth) shows a rapid change at around the tropopause level, 15 to 20 km, above which m_j value remains constant. The zonal momentum flux behaves in a similar way, decreasing rapidly at the tropopause then remaining constant in height.

On the other hand, m_j at 180° (the fourth azimuth) gradually decreases with height. The magnitude of corresponding momentum flux also decreases gradually, establishing the relationship between the vertical wavenumber and the momentum flux. Evolution of m_j at 0° and 180° show how the different parts of the spectrum are chopped off when it is filtering through the background wind profile.

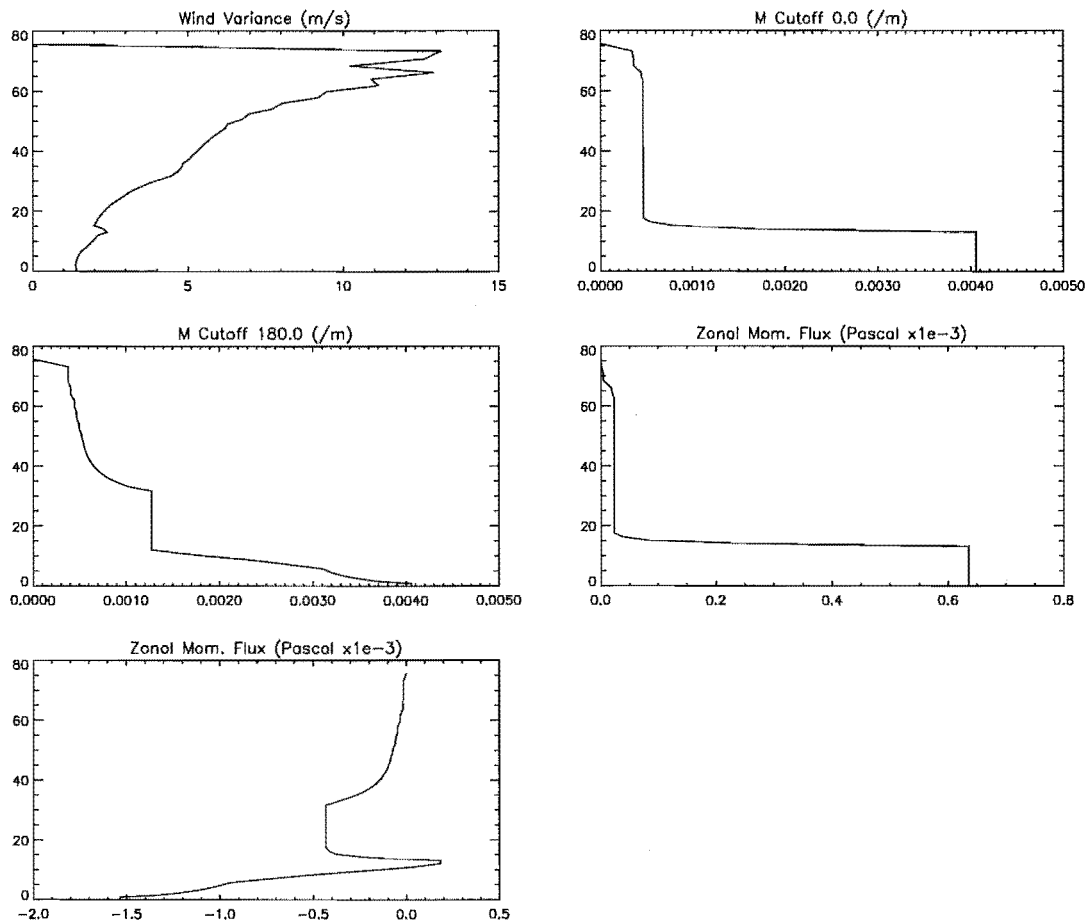

Figure 4.7: Total wind variance, cutoff vertical wave number for first and the fourth azimuths, and momentum flux for first and fourth azimuths when waves are launched from the ground, *SUR*.

In the *TRO* configuration (figure 4.7), σ_t increases uniformly with altitude indicating that the spectrum has not been attenuated at lower levels.

The value of m_j at 0° decreases very rapidly up to the tropopause level, remaining unchanged above that. A similar trend is seen for the corresponding momentum flux which diminishes initially and then remains unchanged. The value of m_j at 180° is constant up to 30 km then gradually decreases to zero. The zonal momentum flux for this particular azimuth has also approaches zero, although there is an initial increase in its magnitude.

These results demonstrate that a differences in the evolution of m_j at 180° for the two configurations have effectively changed the momentum flux at that azimuth. Changes

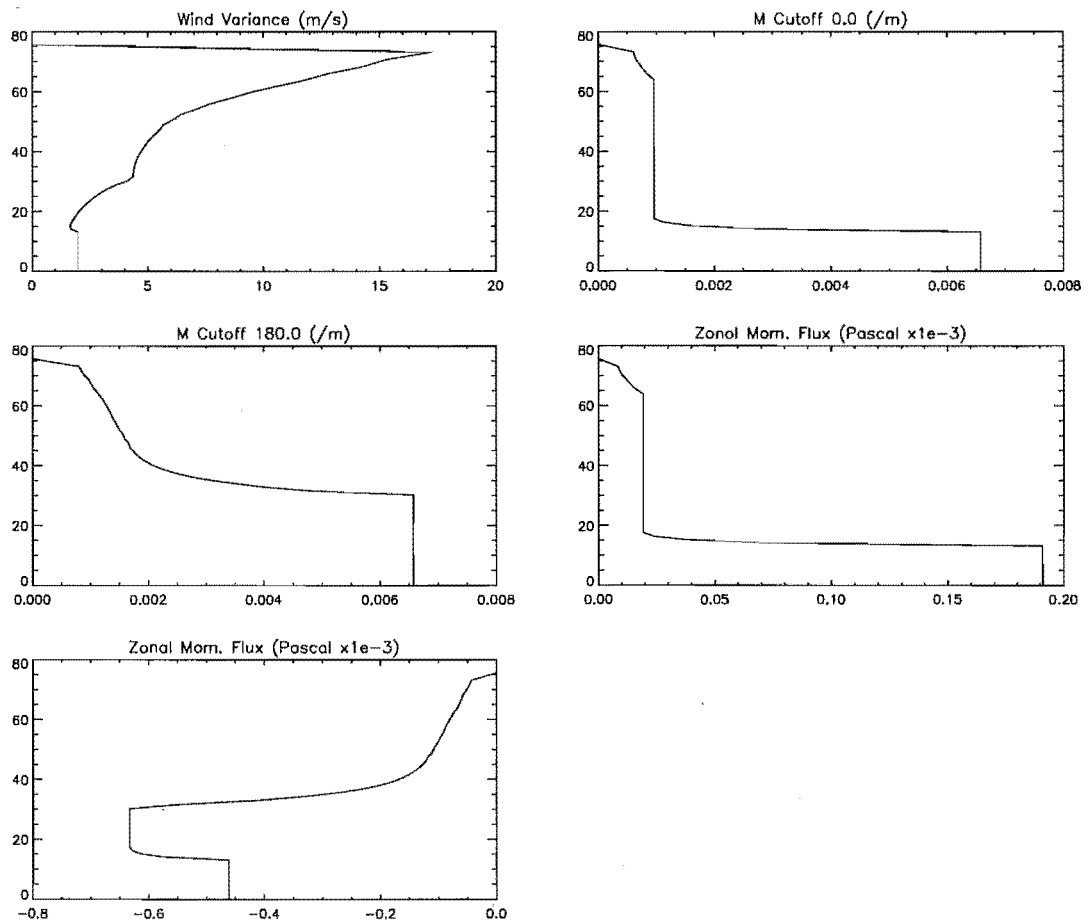

Figure 4.8: Total wind variance, cutoff vertical wave number for first and fourth azimuths, and momentum flux for the first and the fourth azimuths when waves are launched from tropopause, *TRO*.

in the momentum flux values at other azimuths have also contributed to the changes in the total momentum flux of the spectrum and, as a result, the total acceleration differs significantly between the two configurations.

From the above analysis it can be inferred that the tropospheric zonal wind shear (westerly for all cases) filters out a part of the GW spectrum creating a spectral imbalance within the troposphere of the model - an effect that has been discussed earlier. The filtering has resulted in the GW spectrum breaking down earlier in the *SUR* configuration than in *TRO*. The change in momentum flux due to this process contributes to a change in the zonal acceleration, which can induce further changes in the zonal mean flow.

In addition to the above experiments, the *SUR* was also applied to a high mountain case, which was achieved by changing the orographic information at two grid points. The results are the same as those obtained without mountains, because the DSP scheme does not have an orographic GW component. This experiment was conducted to compare the results from the *SUR* configuration with those from the *CTL*, *ORO*, *HIM* and *LOM* configurations.

4.4.3 Effect of combination of the DSP and the UM's orographic schemes

The previous section shows that tropospheric filtering of GWs plays a major role in determining the acceleration produced by them in the upper atmosphere and launching GW spectra from the ground allows the incorporation of these effects. Hence, to demonstrate the effect of both DSP and the UM's orographic schemes together, *SUR* was chosen. The stress and drag of *SUR* and *ORO* are added with each other. Zonal mean wind for winter hemisphere is used to obtain results, similar to the first experiment.

The stress due to *SUR* + *ORO*, figure 4.9 shows negative values. The change in stress below the tropopause is contributed mainly by the stress due to *ORO*. In the upper stratosphere, the reduction in the amount of stress is caused by the filtering of spectra by winter zonal mean wind as explained in the previous section. It should also be noted that the direction of stress in *SUR* is dependent on the direction of the zonal wind. When comapred to the stress in *CTL*, figure 4.9, it is obvious that stress in *CTL* has no contribution above 25 km.

The amount of drag in *SUR* + *ORO* and *CTL*, figure 4.9, both have contribution from

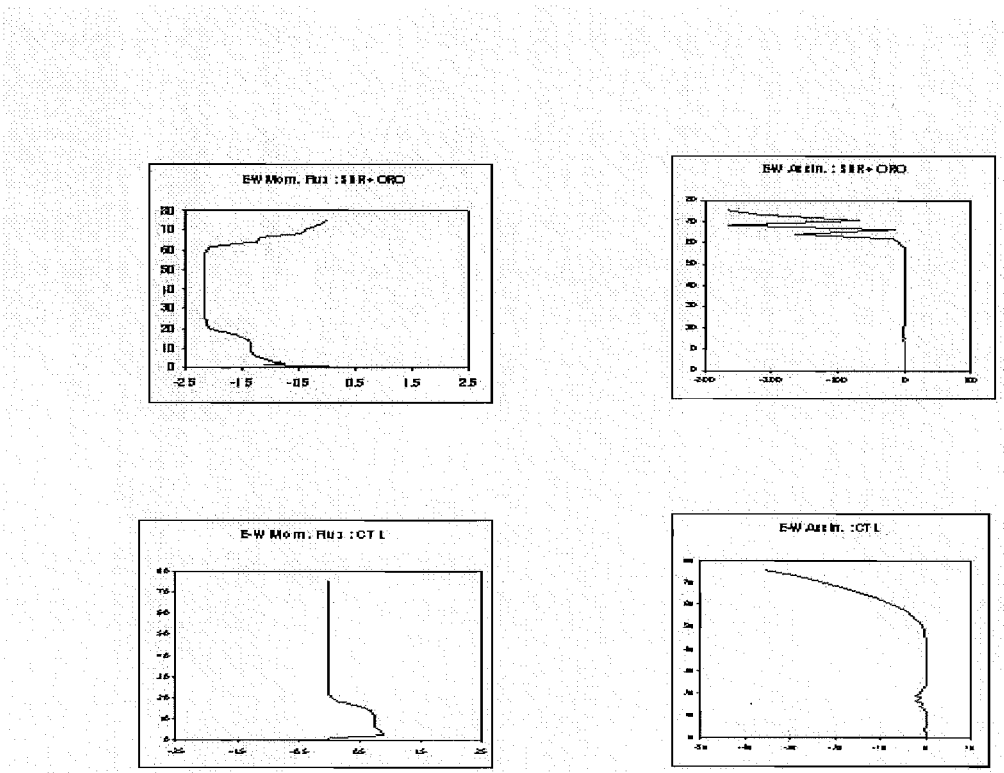

Figure 4.9: Stress or momentum flux ($*10^{-3}$ N/m^2) and drag (m/s/ day) for *SUR* and *ORO* added together (above) and stress ($*10^{-3}$ N/m^2) and drag (m/s/ day) for *CTL* (below).

orography at the lower stratosphere level. However, the amount of drag in *CTL* at the upper stratosphere and lower mesosphere altitude is far less than *SUR* and *ORO* combined together (approximately, 260 m/s/day). This value is in agreement with the values suggested by (*Allen and Vincent*, 1995).

Hence, the combination of *SUR* and *ORO* not only has a damping at the lower stratosphere equal to the value of *CTL*, but is also has almost six times stronger damping of the zonal wind at the model's top-most levels.

4.4.4 Effect of broad spectrum GW

In addition to the combination of *SUR* and *ORO*, the effect of *SUR* only is also studied and the results are discussed in this section. Similar to the last section, zonal mean wind for the winter hemisphere is used to generate the results.

Figure 4.10 shows stress and drag due to *SUR* and *CTL*. The stress in *SUR* shows no significant change in the troposphere and the lower stratosphere as compared to the stress for *SUR*+ *ORO* in figure 4.9. The amount of stress starts decreasing (figure 4.10) at the same level as *SUR* + *ORO* (figure 4.9). This indicates that the significant amount of stress contributed by the orography is absent in the case of *SUR* alone. When compared to *CTL* (figure 4.10), it is obvious that the stress in *CTL* exists only up to the tropopause whereas, the stress in *SUR* does not have any contribution to the model's lower level and works only at the model's topmost levels.

The drag due to *SUR* does not have a contribution from the orography. It differs from the value of drag by *SUR* and *ORO* combined together (figure 4.9) *CTL* (figure 4.9) at the tropopause. However, the amount of drag due to *SUR* is equal to the amount due to *SUR* + *ORO* and is much stronger than that of *CTL* at the model's top-most levels, as shown in figure 4.9 and 4.10.

It can therefore be inferred that although there is no sufficient damping of zonal wind at the troposphere and the lower stratosphere due to *SUR*, *SUR* contributes to significant damping in the upper stratosphere and lower mesosphere levels.

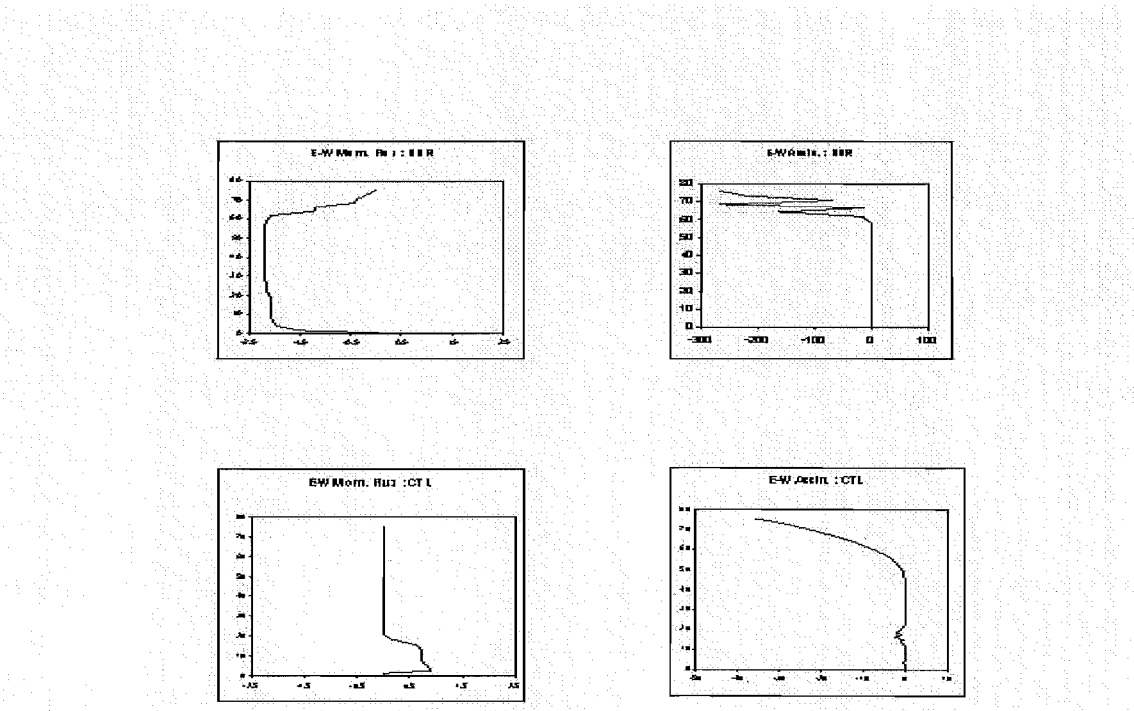

Figure 4.10: Stress or momentum flux ($*10^{-3}$ N/m^2) and drag (m/s/ day) for *SUR* (above) and stress ($*10^{-3}$ N/m^2) and drag (m/s/ day) for *CTL* (below).

4.4.5 Effect of CIBM scheme in the presence of high mountains

To observe the effects due to coupling of orographic waves with broad spectrum waves, the topography of the grids was varied so that they represent high mountains on one grid point, referred to as *HIM*. The values of height and standard deviation of orography were obtained from the UM's existing data for the Andes mountains with an altitude of approximately 5000 to 5500 m.

For CIBM simulations using the *HIM* configuration, the initial spectrum of GWs are launched from the ground. This is because the observational studies, for example, (*Allen and Vincent*, 1995), suggest that gravity waves are generated in the troposphere.

The depth of the surface layer of orographically-induced GWs, $\hat{h}$, in the UM is assumed to be related to the height of sub-grid-scale orography and is calculated as:

$$\hat{h} = min(\sqrt{2}\sigma, 750m), \tag{4.4}$$

where δ is the standard deviation of the sub-grid-scale orography (*Webster*, 1997). The value of $\sqrt{2}\delta$ for both configurations was calculated and are found to be larger than 750 m. Therefore, the surface stress due to orographically-induced GWs is calculated at a height of 750 m above ground level. The GWs were launched at this height with a source strength of 2 m^2/s^{-2} and δ_t of 1.414 m/s. Similar to the previous case zonal mean wind for winter hemisphere is used for the study.

The stress in *HIM* has a negative value because of the filtering of waves through the westerly wind profile. The stress contributed by the *HIM* shows a change at the tropopause level (figure 4.11) indicating dissipation of CIBM waves at that level. A slow reduction in the value of stress is also seen in *CTL* from that level.

It should be noted that the stress in *SUR* (figure 4.10) does not show any change in stress near the tropopause level. Also, the amount of momentum flux in *HIM* starts reducing from a lower level, approximately 45 km, (figure 4.11) than *SUR*, 60 km (figure 4.10), which indicates that the CIBM waves have started dissipating at lower altitudes than the broad spectrum waves. This point is discussed in detail in the following section.

The stress in *SUR+ORO* (figure 4.9) shows a more magnified change in its value in the tropopause compared to *HIM* (figure 4.11). However, the reduction in the value of stress

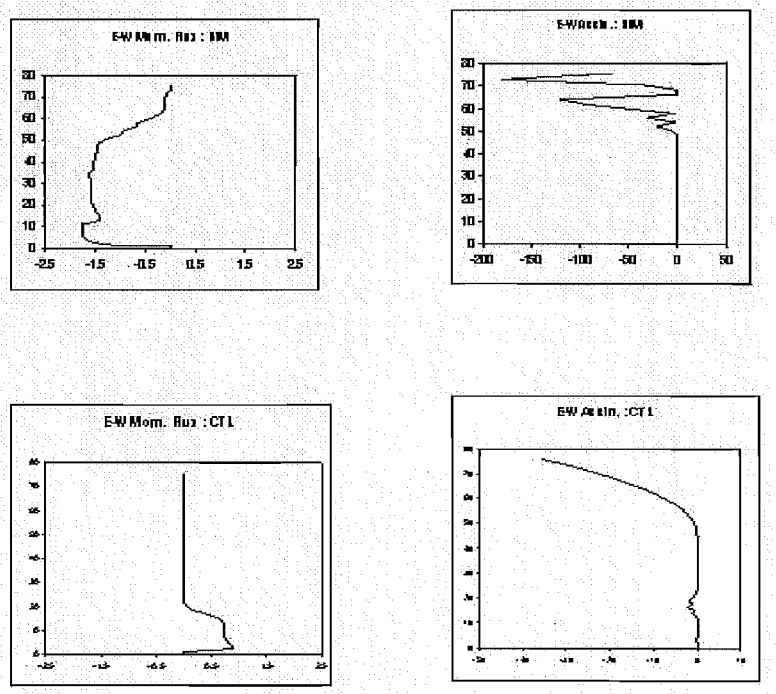

Figure 4.11: Stress or momentum flux ($*10^{-3}$ N/m^2) and drag (m/s/day) for *HIM* (above) and for *CTL* (below).

occurs at much lower level in *HIM* than *SUR+ORO*. It should be mentioned here that in *SUR+ORO* the broad spectrum and orographic waves contribute individually to the overall stress whereas, in *HIM* the stress is produced due to an interaction between the broad spectrum and orographic waves.

HIM produces a drag of -0.1 m/s/day near the tropopause (which is not shown in figure 4.11 due to scaling). It is weaker than the drag in *CTL* at the same level, -3 m/s/day. It is important to remember that orographic drag in *CTL* is dumped at 25 km. However, in *HIM*, the quasi-monochromatic waves are carried higher up in the atmosphere where they start dissipating at higher levels compared to *CTL*.

HIM produces a damping of -170 m/s/day at the top of the model which is much stronger than that produced by *CTL*, -40 m/s/day. It should also be noted that, in comparison to *SUR* and *SUR+ORO*, the *HIM* starts damping the zonal wind at a lower altitude. The amount of drag deposited by *HIM* is also less at the top-most model level than both *SUR* (figure 4.10) and *SUR+ORO* (figure 4.9). This is due to the dissipation of CIBM waves at a lower altitude than the broad spectrum waves. This point is discussed in detail in the next section.

4.4.6 Comparison of CIBM and DSP schemes

A comparison between the CIBM and the DSP schemes are presented in this section. In addition to the high mountains, the effect of low mountains have also been studied. The same grid points were changed again to represent low mountains of approximately 700 to 800 m altitude, referred to as the *LOM*. The values are again obtained from the UM's standard orographic data for the Wales region.
Both the *HIM* and *LOM* configurations were applied to typical mid-latitude summer and mid-latitude winter zonal wind profiles. To illustrate the effect of coupling the DSP and QMC GWs, the results are compared with the *SUR* configuration, as described in the previous section.

For the *HIM* configuration, the initial orientation of the orographically-induced stress and its value in both zonal and meridional directions are given in table 4.1, for a typical mid-latitude summer hemisphere wind profile. Similar values for the *LOM* configuration are shown in table 4.2. The orographically-induced stress and orientation were added to the values associated with the broad spectrum part of the wave, when the wave is launched

Land-points	1	2
S-X-STRESS	4.156×10^{-6}	1.0×10^{-8}
S-Y-STRESS	9.74×10^{-7}	1.99×10^{-9}
$\tan\theta$ =S-Y-STRESS/S-X-STRESS	0.234	0.199
θ°	13.18	11.25

Table 4.1: Zonal and meridional stress (N/m^2) and orientation due to orography (*HIM*) with a typical summer hemisphere wind profile at the model bottom.

from the 750 m level.

Land-points	1	2
S-X-STRESS	2.67×10^{-8}	1.0182×10^{-8}
S-Y-STRESS	$1,48 \times 10^{-9}$	9.91×10^{-10}
$\tan\theta$ =S-Y-STRESS/S-X-STRESS	0.0553	0.0973
θ°	3.17	5.56

Table 4.2: Zonal and meridional stress (N/m^2) and orientation due to orography (*LOM*) with a typical summer hemisphere wind profile at the model bottom.

It should be noted that the orographic stress in *LOM* configuration is much smaller than that of *HIM*, consistent with the expectation that lower mountains will induce weaker orographic GW stress than higher mountains.

The momentum flux in the troposphere for both *SUR* (figure 4.12(a)) and *HIM* (figure 4.12(c)) are negative because of filtering of the GW spectrum by the strong westerly tropospheric jet streams. In the stratosphere and mesosphere regions there is a net positive momentum flux deposition due to the easterly jet streams which filter out the remaining part of the spectrum. In terms of magnitude of the zonal momentum flux, these schemes are similar, indicating that the stress due to orographic GWs alone (figure 4.12(b))is small compared to the broad spectrum waves in the presence of a typical mid-latitude summer hemisphere wind profile.

It should be repeated here that the orographic GW scheme in the UM extends only up to an altitude of 25 to 27 km. However, the difference in momentum flux between *SUR* and *HIM* (figure 4.12(d)) shows a sudden positive stress near the tropopause. This suggests that the presence of orographic waves in the broad spectrum has modified the spectrum in such a way that a significant part of it is filtered out in the tropopause region.

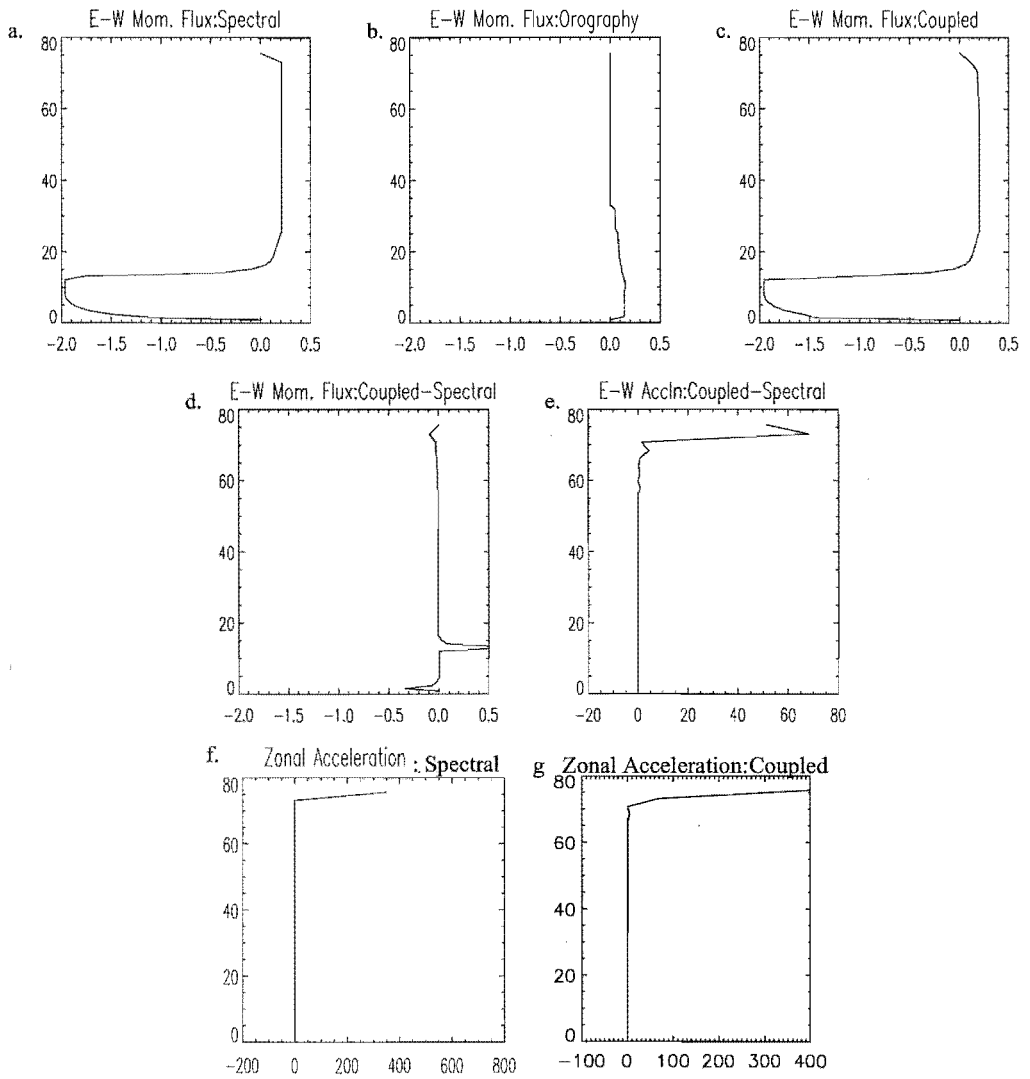

Figure 4.12: Zonal momentum flux (10^{-3}N/m^2) due to (a) broad spectrum waves in DSP scheme *SUR*, (b) due to orography only, (c) due to coupled interactive broad spectrum and monochromatic waves *HIM*, (d) due to difference between coupled interactive and DSP, (e) difference between zonal acceleration (m/s/day) for coupled interactive and DSP (*HIM*$-$*SUR*) for a summer hemisphere zonal wind profile, summer mid-latitude zonal acceleration when spectra are (e) launched from ground for *SUR* (m/s/day) and (f) in the presence of high mountains *HIM* (m/s/day).

The zonal acceleration profiles for *SUR* (figure 4.12(f)) and *HIM* (figure 4.12(g)) suggest that the waves in *HIM* configuration start breaking down at a lower altitude, resulting in zonal acceleration also at a lower altitude than that of the *SUR*. Although the difference (figure 4.12(e)) is small when compared to the amount of total acceleration produced by both at the model's topmost level. It can be inferred that the coupling of orographic and broad spectrum can induce very small changes in the zonal acceleration during summer.

Zonal momentum flux and acceleration for *LOM* are also studied. They are found similar to that of *HIM* for mid-latitude summer wind profile and hence are not discussed separately. The results indicate that varying topography has no effect in the mesosphere of the CIBM scheme during summer. Detailed results for this case are presented in *Appendix D*.

A similar experiment using the *HIM* and *LOM* configurations was performed in the presence of a typical mid-latitude winter hemisphere wind profile to study the effect of orography in the winter hemisphere. Initial values of stress and their orientation at the model's lowest level are shown in tables 4.3 and 4.4 for *HIM* and *LOM*, respectively. These are very similar to their summer hemisphere counterparts. This may be due to the low level tropospheric wind, which has approximately similar values during summer and winter.

Land-points	1	2
S-X-STRESS	5.75×10^{-6}	1.18×10^{-8}
S-Y-STRESS	1.34×10^{-6}	2.34×10^{-9}
$\tan\theta$ =S-Y-STRESS/S-X-STRESS	0.233	0.198
θ°	13.1	11.21

Table 4.3: Zonal and meridional stress (N/m^2) and orientation due to orography (*HIM*) with a typical winter hemisphere wind profile at the model bottom.

Zonal momentum flux values for *SUR* (figure 4.13(a)), *HIM* (figure 4.13(c)) and *LOM* (figure 4.13(h)) are negative from troposphere through to stratosphere (50 km) due to filtering of the waves through the westerly wind profile. However, the zonal momentum flux in *HIM* and *LOM* have started reducing in magnitude at a lower level than *SUR*. This indicates an attenuation of CIBM spectrum earlier than the broad spectrum GWs. Furthermore, the event has taken place earlier in *LOM* as compared to *HIM* due to relatively weaker CIBM GW spectrum in *LOM*. Contribution from GW due to orography

Land-points	1	2
S-X-STRESS	3.148×10^{-8}	1.197×10^{-8}
S-Y-STRESS	1.793×10^{-9}	1.169×10^{-9}
$\tan\theta$ =S-Y-STRESS/S-X-STRESS	0.0553	0.0977
$\theta°$	3.17	5.58

Table 4.4: Zonal and meridional stress (N/m^2) and orientation due to orography (*LOM*) with a typical winter hemisphere wind profile at the model bottom.

only (figure 4.13(b)) shows that zonal stress in troposphere is larger in magnitude with a winter hemisphere wind profile than that of summer wind profile as shown in figure 4.12(b).

The evidence of an earlier dissipation of CIBM GW can also be noticed in the zonal acceleration profiles of *HIM* (figure 4.13(g)) and *LOM* as compared to *SUR* (figure 4.13(i)) where the acceleration can be observed at a lower altitude. The difference between zonal acceleration of *HIM* and *SUR* (figure 4.13(e)) also shows that the zonal acceleration for *HIM* is less than *SUR* at the topmost layer of the model. Also, zonal acceleration in *LOM* (figure 4.13(i))are exhibited at an even lower altitude than *HIM* (figure 4.13(g))and the magnitude is smaller than that of *HIM* at the topmost level of the model. This indicates the dissipation of the spectrum in *LOM* configuration at a lower level than that of *HIM*.

The results suggest that the orographic part of the spectrum in *HIM* configuration has evolved through troposphere and has destabilized the spectrum at a lower altitude than that of *SUR*. As a result, the spectrum has started to dissipate by depositing momentum flux and acceleration at a lower altitude than *SUR*. When the spectrum in *HIM* finally reaches the mesosphere, it is much weaker than the spectrum in *SUR* with lower zonal acceleration at the model's upper most level. Also, with a weaker orographic part of CIBM spectrum in *LOM* the waves break down at a relatively lower altitude compared to *HIM* in the presence of a typical mid-latitude winter zonal wind profile.

The zonal momentum flux produced by orography with the summer hemisphere wind profiles is smaller than that reported in the literature (*Lilly et al.*, 1982), (*McFarlane*, 1987) and (*Milton and Wilson*, 1996). However, zonal momentum flux obtained for the winter hemisphere wind profile is comparable with those reported in the literature. Nevertheless, it should be mentioned here that the UM, as a climate model, has much lower resolution than the mesoscale models used by *McFarlane* (1987) and *Milton and Wilson* (1996) for the studies. Furthermore, the results shown in the citations are restricted to

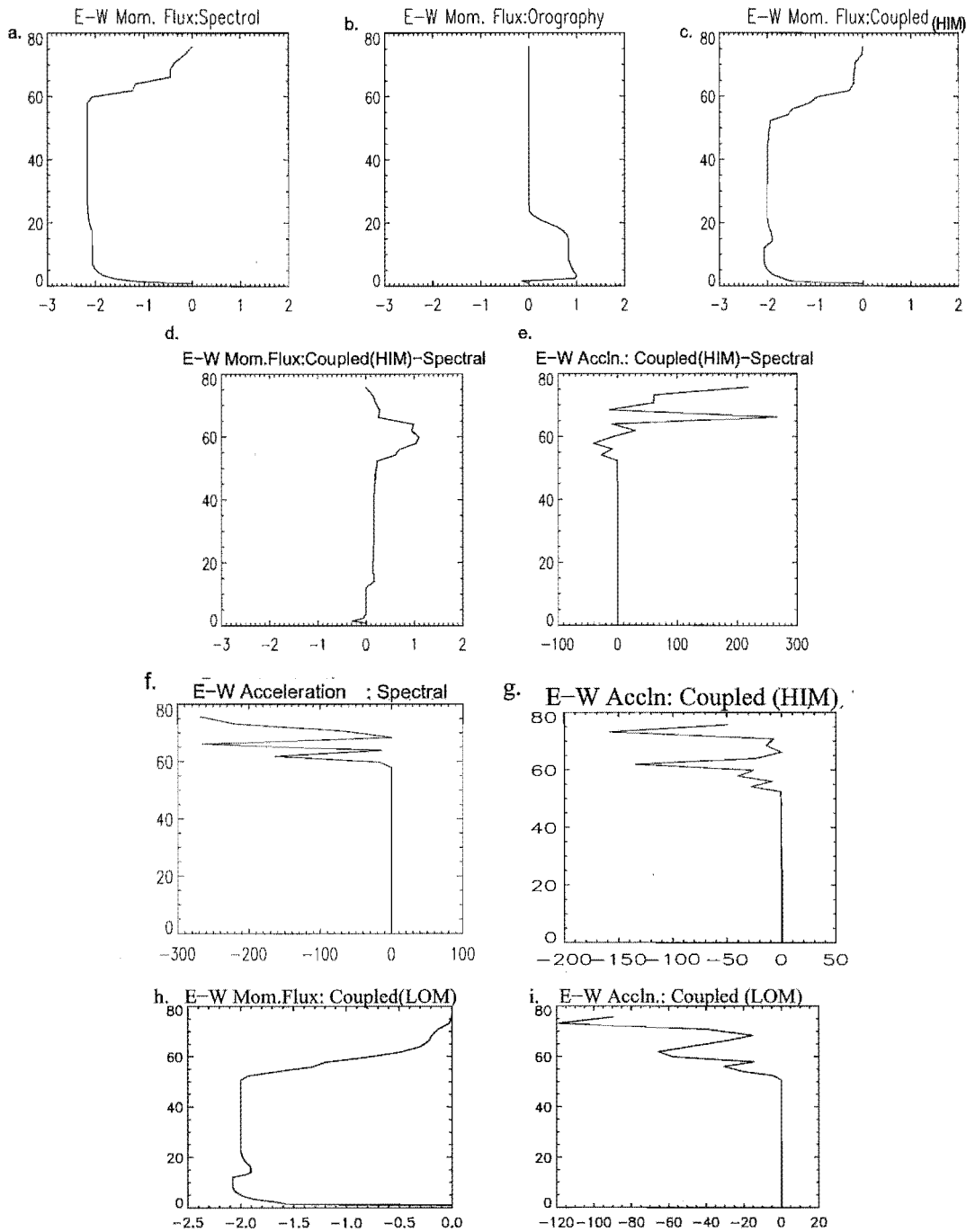

Figure 4.13: Zonal momentum flux ($10-3N/m^2$) due (a) broad spectrum waves in DSP scheme *SUR*, (b) orography only, (c) coupled interactive waves *HIM*, (d) coupled interactive–DSP (*HIM*−*SUR*), (e) zonal acceleration (m/s/day) for coupled interactive–DSP (*HIM*−*SUR*) for a typical winter hemisphere zonal wind profile, typical winter mid-latitude zonal acceleration when spectra are (f) launched from ground for *SUR*, (g) in the presence of high mountains *HIM* (m/s/day), (h) zonal momentum flux and (f) acceleration in the presence of low mountains *LOM*.

lower stratosphere only.

It is also obvious from the results that, with the typical winter hemisphere wind profile the effect of coupled orographic GWs is magnified as compared to the summer hemisphere wind profile, which is also suggested by *Osprey* (2001). It will be therefore interesting to study the effect of these schemes in the UM to determine if a similar trend is also observed on a global scale.

4.5 Summary

The results presented in this chapter are obtained from a single-column test bed based on the UM architecture. Two different physically realistic GW parameterization schemes, namely, DSP and CIBM schemes, (*Hines*, 1997a) and (*Hines*, 1997b), were assessed within this test bed prior to being incorporated in the original UM. The DSP and CIBM schemes were also compared to the UM's original GWD scheme. The experiments described in this chapter emphasize the effects of: the orography only, tropospheric filtering of broad spectrum GWs, combination of the broad spectrum and orographic waves working in parallel, broad spectrumonly and the effect of coupled-interactive broad spectrum and orographic waves over varying topography.

The evolution of GW in the schemes were studied using different configurations. The UM's original GWD scheme with orographic GWD and Rayleigh friction (*CTL*) and the orographic GWD scheme alone (*ORO*). The DSP scheme was tested with different launching heights of the broad spectrum of waves:

- *SUR: The surface,* and
- *TRO: The tropopause,* 200 *hpa or approximately* 12 *km.*

Combination of *SUR* and *ORO* was compared with *CTL.*

The CIBM scheme was tested with different orography:

- *HIM: High mountains, and*
- *LOM: Low mountains.*

Physical parameters such as meridional wind, temperature and BV frequency were set constant for all the tests, which made use of the following zonal wind profiles: a typical QBO profile in the tropics, mid-latitude summer hemisphere and mid-latitude winter hemisphere.

From the studies of *CTL* and *ORO* configurations it can be summarized that *ORO* only contributes to zonal wind damping up to a height of approximately 25 km. The drag due to *CTL* not only damps the zonal wind up to 80 km, it also contributes to equal amount of drag in the troposphere and the lower stratosphere as *ORO*.

Comparison of results for the *SUR* and *TRO* configurations implies that local shear in the troposphere generates a spectral imbalance when broad spectrum GWs are launched from the ground (*SUR*). Due to this bias, the spectrum destabilizes and starts dissipating at a lower altitude as compared to the configuration where the waves are launched from the tropopause (*TRO*). Evidence of this process is also seen in zonal acceleration profiles for the two cases where it is weaker in magnitude at the model's top-most level for *SUR* than that of *TRO*. A similar behaviour of broad spectrum waves has also been reported by *Manzini and McFarlane* (1998).

The effect of combination of *SUR* and *ORO* was also studied against *CTL*. The results show that in *SUR+ORO* the orographic GWD scheme produce stress and resultant drag near the tropopause and the DSP scheme produces damping of the zonal wind at the lower mesosphere. Although the amount of drag at the troposphere is same as that of *CTL*, *SUR+ORO* produces far stronger drag at the lower mesosphere as compared to *CTL*.

SUR was also compared with *CTL*. The results show that unlike *CTL* and *SUR+ORO*, *SUR* does not show any damping in the tropopause, as there is no orographic GWD scheme in *SUR* configuration. However, the drag produced by *SUR+ORO* and *SUR* are equal in magnitude in the lower mesosphere and is stronger than that produced by *CTL* at the same levels.

To simulate the effect of coupling QMC waves to the broad spectrum waves, the stress and orientation due to orographically-induced GWs (tables 4.1 and 4.3) were added to the broad spectrum information. When *HIM* was compared with *CTL*, a change in the value of stress in *HIM* was seen in the tropopause region. However, the resultant drag

was found to be weaker than that produced by *CTL* at the same level. However, the amount of drag contributed by *HIM* is stronger than *CTL* at the upper stratosphere and lower mesosphere. It is also noticed that deposition of momentum flux and the resultant drag in *HIM* occurs at a lower altitude than *SUR*, indicating dissipation of CIBM waves at a lower altitude in *HIM* compared to *SUR*.

With a mid-latitude summer hemisphere wind profile, it was found that the zonal momentum flux was not strongly affected by the introduction of orographic waves. Furthermore, changes in the height of mountains did not significantly affect the CIBM GW acceleration in the mesosphere.

With a mid-latitude winter zonal wind profile, the momentum flux starts reducing in magnitude at lower altitudes in *HIM* and *LOM* as compared to *SUR*. The results show that the CIBM spectrum is supported by a background westerly wind up to the winter stratopause where it starts dissipating in the presence of mountains. The main reason behind this is that the spectrum becomes predisposed to instability when orographic spectrum is included in broad spectrum waves (*Hines*, 1997b). As the CIBM spectrum reaches the upper most level of the model its strength reduces considerably. As a result, the acceleration produced at the top level is also weaker than when broad spectrum waves are launched from the surface.

It should also be noted here that with a mid-latitude winter wind profile, the GW spectrum in the presence of low mountains starts dissipating earlier than the spectrum generated by high mountains, which is seen in their respective zonal momentum flux and acceleration profiles. This is due to relatively weaker orographic spectrum associated with the low mountains as compared to that associated with the high mountains. The results further indicate that the effect of CIBM scheme is greatly pronounced with the mid-latitude winter wind profile than with summer wind profile which has also been discussed by *Osprey* (2001).

Single column test bed results give useful insights about the propagation and obliteration of GW simulated in different physical regimes. The effects on an atmosphere consisting of fewer parameter spaces than a GCM is identified. It is of paramount importance to explore if such effects are also reflected in a global scale. Hence, the parameterization schemes are further incorporated in the UM. The model results simulated with the DSP scheme and 'coupled interactive' broad spectrum monochromatic wave scheme are dis-

cussed in detail in the next chapter.

Chapter 5

Tropospheric Sensitivity to Coupling Orographic and Spectral GW Parameterizations

5.1 Introduction

The DSP (henceforth *spectral*) and coupled interactive monochromatic and spectral (henceforth *coupled*) schemes have been incorporated in the UM. The use of these schemes in the simple model test-bed was outlined in the foregoing chapter and in this chapter we progress to the application of these schemes in a sophisticated GCM that includes a troposphere. Previous applications of the DSP have either not used a coupled scheme, e.g., *Manzini and McFarlane* (1998), or have not used a model with a complete representation of the troposphere *Osprey* (2001). Here, we examine the sensitivity of the tropospheric climate to the different schemes and in the next chapter we examine the influence of the coupling on middle atmosphere dynamics.

To examine the climate sensitivity in the model the UM was run for two six years simulations, incorporating the *spectral* and *coupled* parameterizations, respectively. In each case, the spectrum of waves was launched at the model's ground level. In both cases, the source has equal strength and other parameters are kept similar to the values already discussed in the test-bed, as discussed in Chapter 4. In addition to the above specifications, orographic GWD of the original UM has been changed with the introduction of an interacting broad spectrum and quasi-monochromatic waves.

In addition to *spectral* and *coupled* schemes, the UM is also run for 6 years with its original GWD scheme (henceforth *original*). The results from the troposphere and lower stratosphere for the *original* is compared qualitatively with UKMO assimilated data at the begining of this chapter.

5.2 Comparison of the original GWD scheme and UKMO assimilated data

It should be mentioned before comparing the results of *original* with the UKMO data that the UKMO assimilated data system, (*Swinbank and O'Neill*, 1994), produces a self consistent sequence of three-dimensional grid-point analyses of the atmosphere, using observations (from radiosondes and satellites) to constrain the evolution of the model (UM's 42– level model). It consists of daily global fields of temperature, geopotential height and three component of winds. Studies performed by (*Coy and Swinbank*, 1997) have found that the UKMO analyses agree quite reasonably with Goddard Space Flight Center stratospheric analyses and that the results are not biased by the UKMO model. Also, studies by (*Manney et al.*, 1996) have revealed the fact that UKMO analyses are realistic and have been successfully used by (*Manney et al.*, 1994) in studies of the stratospheric polar vortex. For our purpose, only the monthly mean fields of the above mentioned diagnostics are compared qualitatively with the results of *original* simulation.

(*Swinbank et al.*, 1998) also reported a similar comparison of the model results, their model's lid height was different from the one used in this case. They used the climate version of the UM with 49 levels which extends up to an altitude of 64 km. The UM in this case has 55 levels and the model lid height extends up to 80 km.

5.2.1 Northern hemisphere winter

Six year monthly average of zonal mean zonal wind for the months of December, January and February (top to bottom) are presented in figure E.1. Results from the *original* simulations are presented on the left and the UKMO assimilated data are plotted on the right.

An external comparison of the results shows that there are considerable similarities between them in the position and the shear of the jets. The main differences are the strength of the tropospheric westerly jets in both the hemispheres. The *original* displays stronger jets compared to the UKMO data for all three months. The westerly jet in northern hemisphere lower stratosphere is also stronger in *original* than UKMO assimilated data. In addition to the above the easterly jet in the southern hemisphere lower stratosphere is weaker in the UKMO assimilated data than the *original.*

This consistent difference in the strength of zonal mean zonal wind may indicate a weak

damping by gravity waves which is a motivation for a better GWD scheme for the UM.

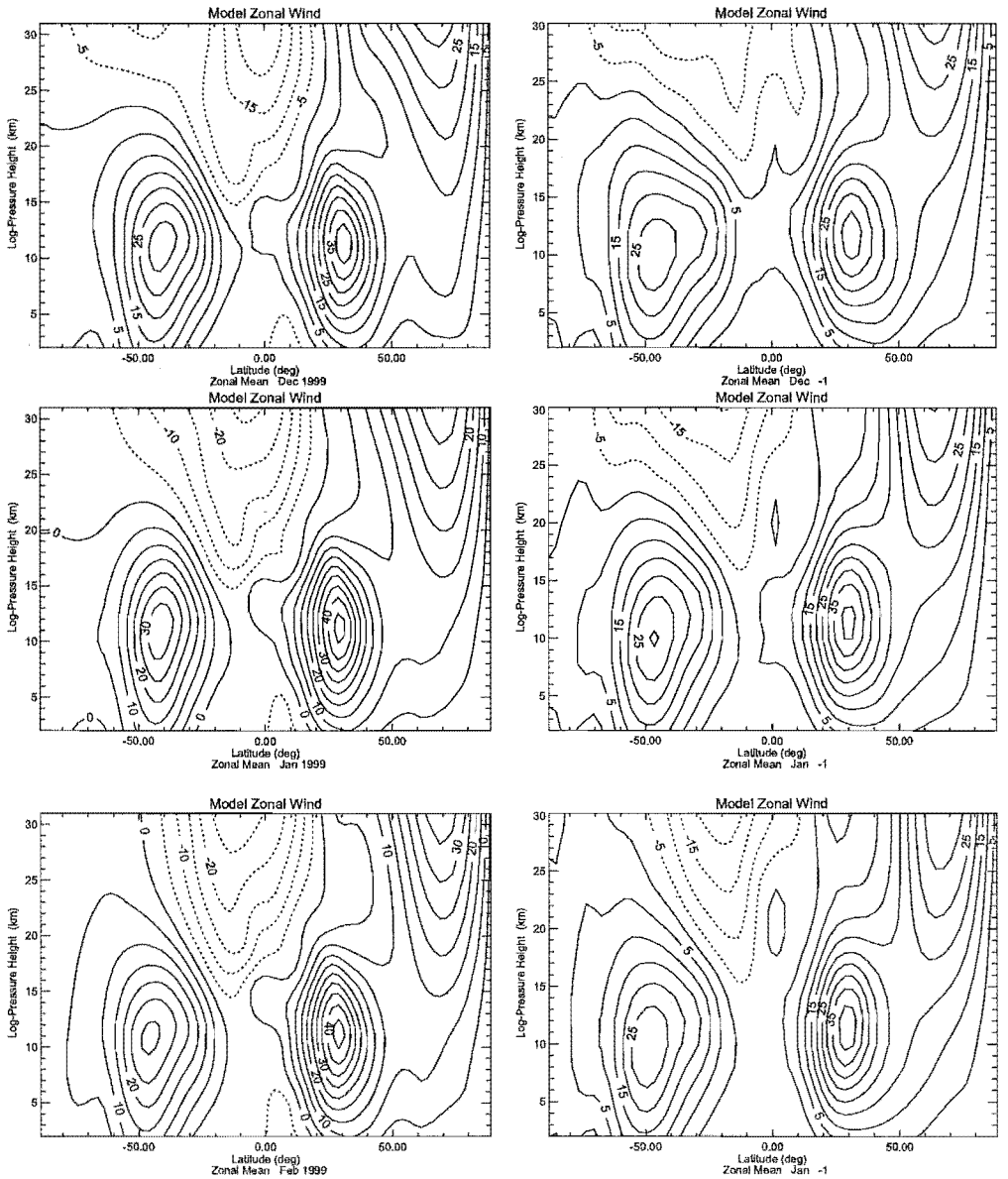

Figure 5.1: Zonal mean zonal wind for *original* (left) and UKMO (right) data for (top to bottom) December, January and February. Contour interval is 5 m/s.

Figure E.3 represents 6 years average of monthly mean zonal temperature for both *spectral* and UKMO data. The plots exhibit similarities in the temperature profiles in showing the cold tropical troposphere and the cold polar stratosphere in the Northern hemisphere.

However, the main difference between the plots is the persistent lower temperature in the stratosphere of the *original* in both the hemispheres compared to the UKMO fields. The

lower temperature seen in the Northern Hemisphere polar stratosphere compares well in January between the *original* and UKMO data. However, the temperature in the same region is much lower in the *original* than in that of the latter. This is a common discrepancy which has been detected in many GCMs, (*Pawson et al.*, 2000), and has been attributed to a weak GW forcing.

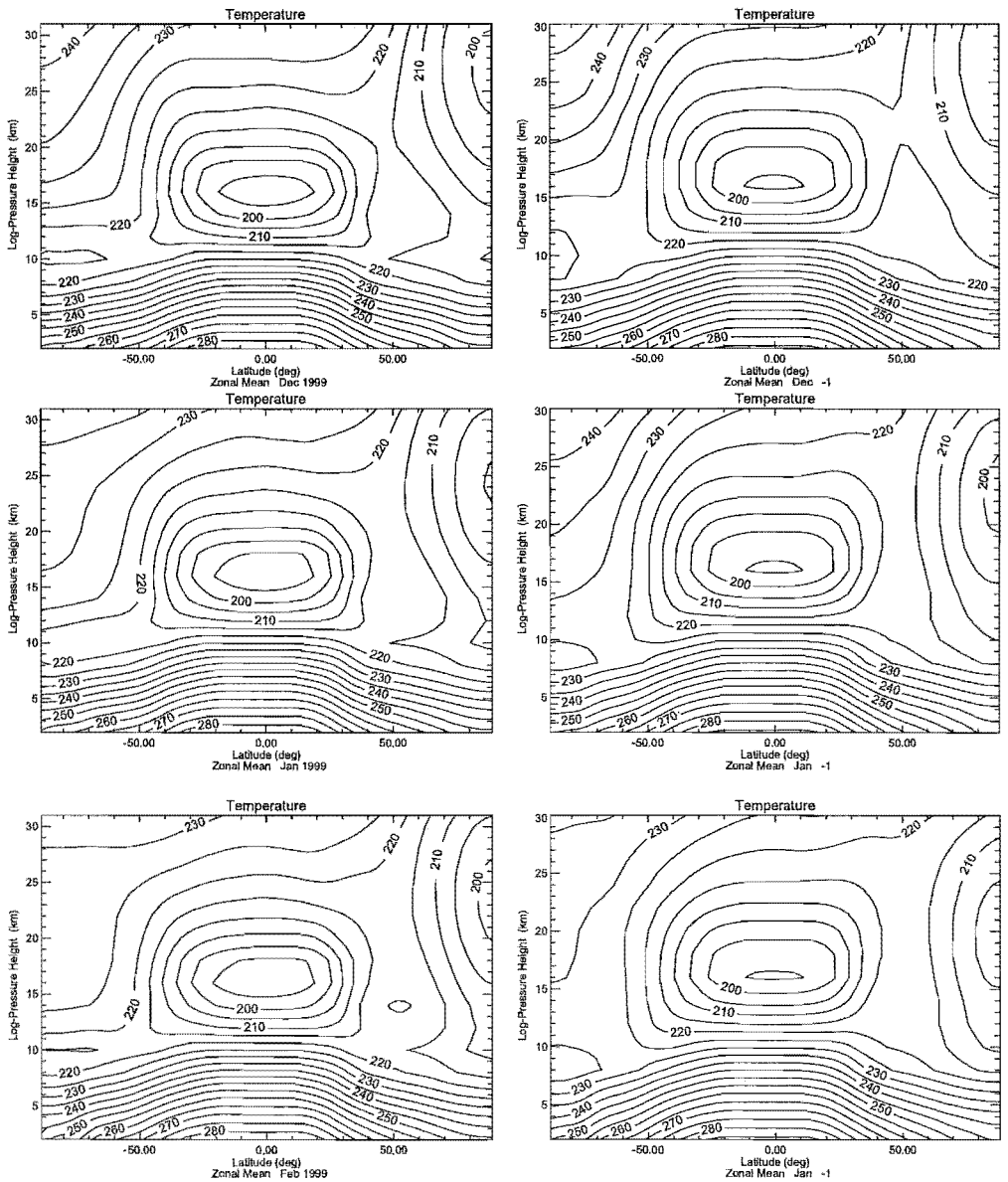

Figure 5.2: Zonal mean temperature for *original* (left) and UKMO (right) data for (top to bottom) December, January and February. Contour interval is 5 K.

6 years average of monthly mean values of zonal mean meridional (top) and vertical (bottom) velocities for the month of January are presented in the figure E.4 for the *originsl*

and UKMO assimilated data. An overview of the figureE.4 for the meridional and vertical velocities show similarities in the features for the *original* and the UKMO data. However, both meridional and vertical velocities are stronger in the *original* than that of the UKMO fields. An interesting feature in the vertical wind plots can be identified in both cases. There is an up welling of the zonal mean vertical wind in the northern hemisphere polar lower stratosphere. This might be due to SSW causing an adiabatic motion at that region during the Northern Hemisphere winter (*Ruth et al.*, 1994). It should be noted here that the strength of the vertical motion in the *original* is stronger than the UKMO fields.

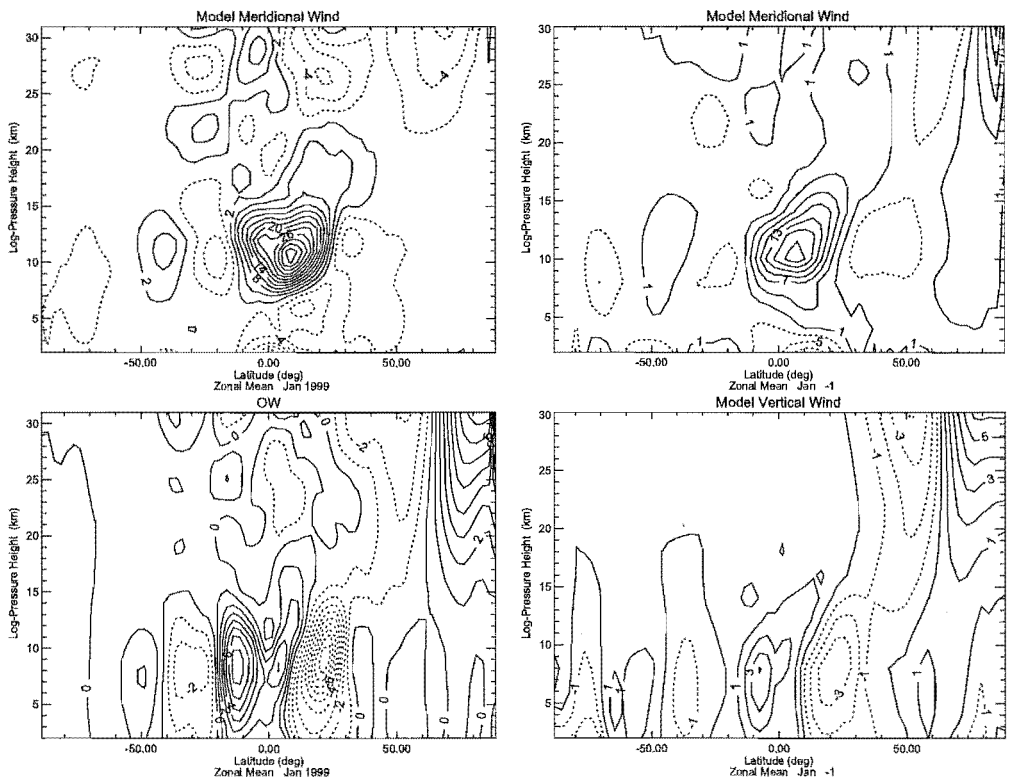

Figure 5.3: Zonal mean meridional and vertical wind for *original* (left) and UKMO (right) data for January only. Contour interval for meridional wind profiles is 3 decim/s and vertical wind is 1 mm/s.

5.2.2 Southern hemisphere winter

Figure E.5 represents six year monthly average of zonal mean zonal velocities for both the *original* and UKMO assimilated data fields for June, July and August. The strength and the position of the jets in both the hemispheres are similar in both cases as opposed to those of the Northern Hemisphere winter months.

However, strength of the easterly jets in the northern hemisphere lower stratosphere is more in *original* than the UKMO assimilated data which might again indicate a nessecity for stronger GW damping.

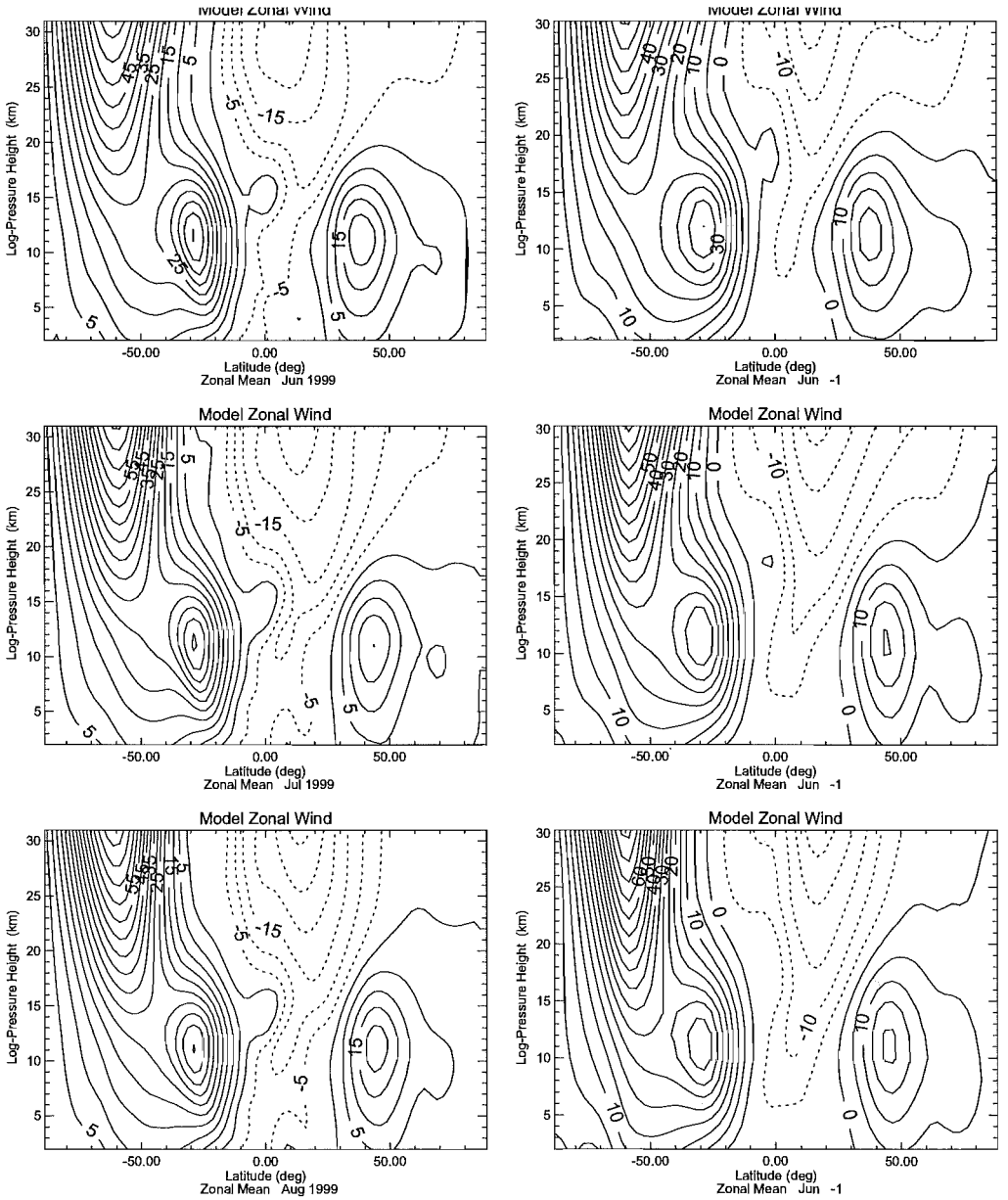

Figure 5.4: Zonal mean zonal wind for *original* (left) and UKMO (right) data for (top to bottom) June, July and August. Contour interval is 5 m/s.

Figure E.7 shows the zonal mean temperature for the *original* and UKMO assimilated data fields. The lower polar temperature in the Southern Hemisphere lower stratosphere

similar to each other. However, the rest of the lower stratosphere is colder in the *original* than in the UKMO fields as seen during December, January and February.

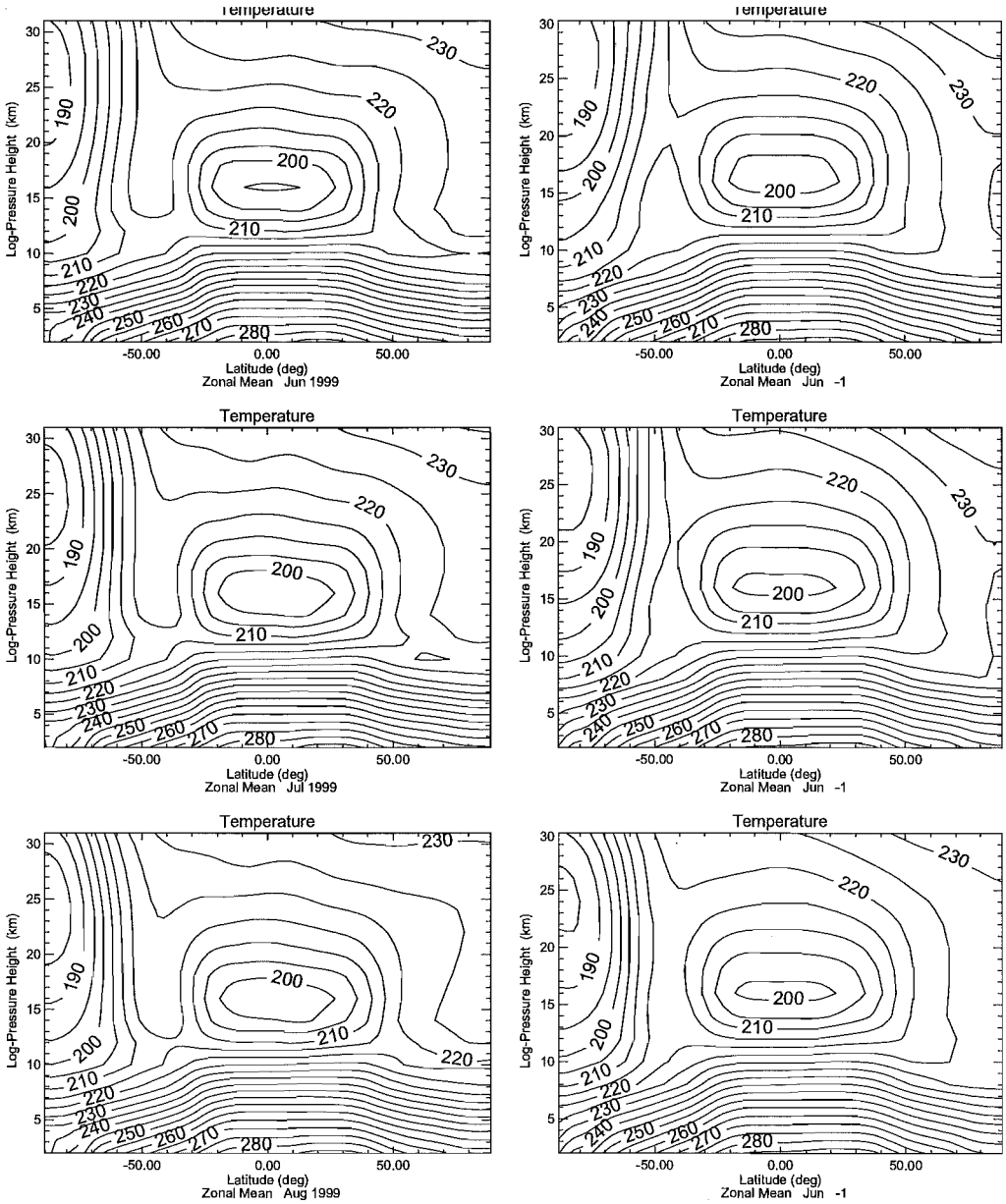

Figure 5.5: Zonal mean zonal wind for *original* (left) and UKMO (right) data for (top to bottom) June, July and August. Contour interval is 5 K.

The zonal mean meridional and vertical velocities for, July only, are shown in figure E.8. Comparison between the *original* and the UKMO data shows that the meridional wind in the tropical tropopause is much weaker in the latter. Also, the positive meridional wind shear in *original* at the tropical stratosphere is not observed. The features of the zonal

mean vertical velocity are well reproduced by *original* in comparison with UKMO data fields. However, the strength of the zonal mean vertical wind is greater in the *original* than the UKMO data.

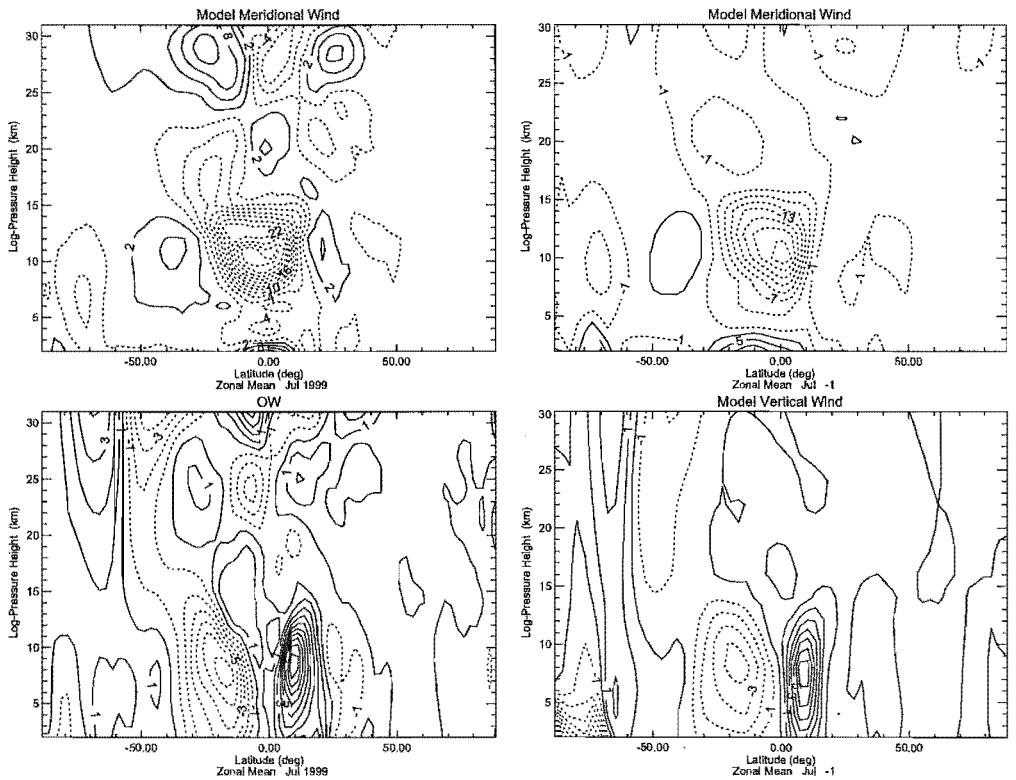

Figure 5.6: Zonal mean meridional and vertical wind for *original* (left) and UKMO (right) data for July only. Contour interval for meridional wind profiles is 3 decim/s and vertical wind is 1 mm/s.

Comparison of the *original* and the UKMO assimilated data shows that the tropospheric jets in both hemispheres are stronger in the *original* than that of the actual data. The southern hemisphere winter zonal mean zonal wind in the *original* up to an altitude of lower stratosphere compare very well with the assimilated data. However, the temperature fields from the model results show a persistent lower temperature in *original* compared to the assimilated data , a feature observed in most of the GCMs. The meridional and the vertical winds are very similar in both cases. The above study therefore indicates a nessecity for the incorporation and further studies of new GWD schemes in the UM. The results are presented in the following sections.

5.3 Comparison of *Spectral* and *Coupled* during northern hemisphere winter

In this section, the tropospheric zonal mean wind and temperature simulated by the two schemes are compared. As expected, the main differences in these fields are attributed to the difference in parameterized GW acceleration. In addition, changes in resolved waves and stationary planetary wave processes are also discussed.

Figure 5.7 shows the tropospheric and lower stratospheric zonal mean zonal wind for the *coupled* and *spectral* runs, and their difference, averaged over the month of January for six year simulation period. In this chapter, all figures use a vertical coordinate that is an effective height in km. While the model domain extends to near 80 km, the panels are limited to the lower 30 km so that tropospheric features are highlighted.

The main differences that can be seen in the northern (winter) hemisphere and the tropics are: a weaker stratospheric polar night jet in the coupled simulation (discussed in more detail in chapters 7 and 8); there is a stronger mid-latitude jet stream in the coupled scheme, and the tropical jet structure is different. It can be seen that the polar night jet is rather more distinct from the mid-latitude jet in the spectral simulation.

In addition to that, when zonal mean zonal wind in *spectral* and *coupled*, fig. 5.7 are compared with the same parameter in *original*, fig. E.1, it is found that, *original* has a stronger polar night jet compared to the other two cases. However, *coupled* has a stronger midlatitude jet-stream than *spectral* and *original*. It should be noted that the difference in contour intervals are accounted for while describing these features.

Figure 5.8 shows the zonal-mean temperature fields for the *spectral* and *coupled* runs and *spectral-coupled* differences, again averaged over the month of January for the six year period. The main features are a much cooler northern stratosphere, warmer polar upper troposphere (> 5K), and the warmer northern middle latitude stratosphere (all in the *spectral* simulation, in comparison with the *coupled* simulation). While these features are clearly in thermal wind balance with what is seen in the zonal-mean winds, the temperature differences also highlight the additional feature in the southern hemisphere, where the upper troposphere is also > 1K warmer in the *coupled* simulation. The wind perturbation in balance with this is not obvious due to the contour intervals chosen which highlight the large northern hemisphere differences.

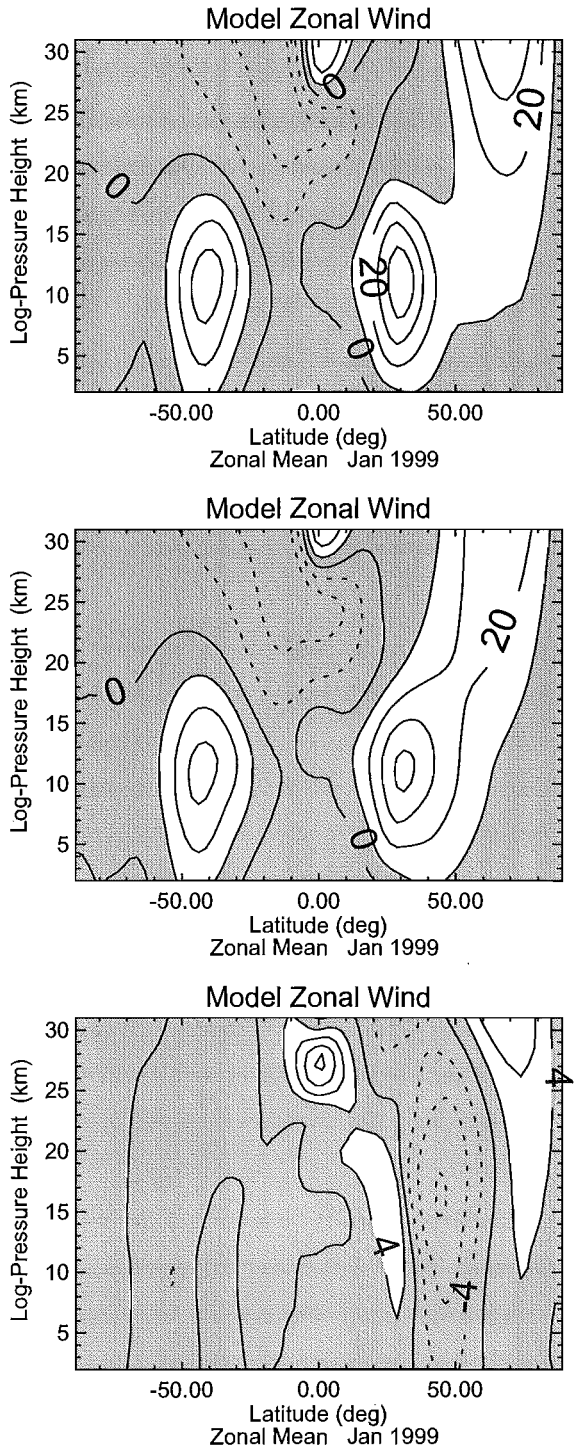

Figure 5.7: Zonal-mean zonal-wind for the *spectral* (top), *coupled* (middle) and their difference for the six-year January average (bottom). The contour interval is 10 m/s in the top two panels and 4 m/s for the lower panel.

Zonal mean zonal temperature of *spectral* and *coupled* are compared with the *original*. It is clear from fig. 5.8 and fig. ?? that the tropical tropopause in the *original* is much colder than the other two cases, which may be indicative of an improvement in the GWD scheme. However, *spectral* and *original* show warmer temperatures in the midlatitude tropopause and the lower statosphere.

Given that the external difference between the simulations is the GW acceleration, this acceleration is examined in an effort to explain these results. The key difference between the two simulations is that in the *spectral* simulation there are two independent gravity wave parameterizations operating, the UM's original orographically-induced GW scheme and the DSP scheme. In the *coupled* case the two are intimately linked. The total forcing on the background wind, in this case, is contributed by broad spectrum GW modified by the orographically induced waves.

The GW zonal acceleration contributed by the 'broad spectrum' or DSP part of the *spectral* simulation and the total zonal acceleration of the *coupled* simulation are compared with each other for the month of January in figures 5.9 and 5.10. It can be observed from figure 5.10 that there is no significant difference in GW acceleration in the northern hemisphere mid-latitudes up to an altitude of around 15 km. This difference is not strong enough to damp the zonal mean wind in the *spectral* simulation which does not explain the observed values obtained by *Lilly et al.* (1982).

It should be recalled from the test-bed results in Chapter 4, that independently propagating orographically-induced GWs produce strong momentum flux (1×10^{-3} N/m^2) in the troposphere and lower stratosphere level in the presence of high mountains during winter. It was also discussed that the orographic part of the spectrum in the *coupled* scheme propagates high in the middle atmosphere and starts breaking down in the stratosphere. Hence, the contribution from orographically-induced gravity waves in the *spectral* simulation is studied next. As noted in Chapter 4, this component of GW acceleration extends only up to 27 km of the model.

The contribution to orographic drag from various phenomena, such as, hydraulic jump, lee waves and saturation of waves are calculated. It is found that forcing due to hydraulic jump and lee wave phenomena extends only up to an altitude of 750 hPa and their amplitudes are considerably weaker than the saturation process. Hence, the six year average

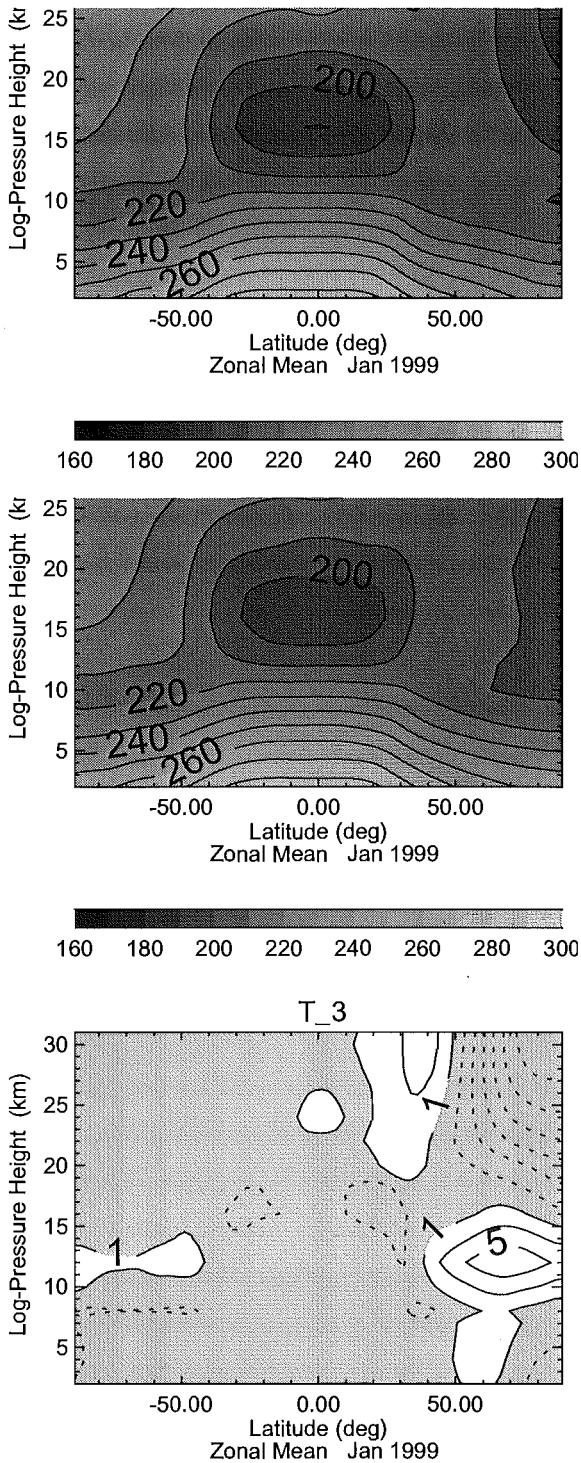

Figure 5.8: Zonal-mean temperature for the *spectral* (top), and *coupled* (middle) runs and their difference (bottom) for January averaged over six years. The contour interval is 10 K for the top two panels and 2 K for the last panel.

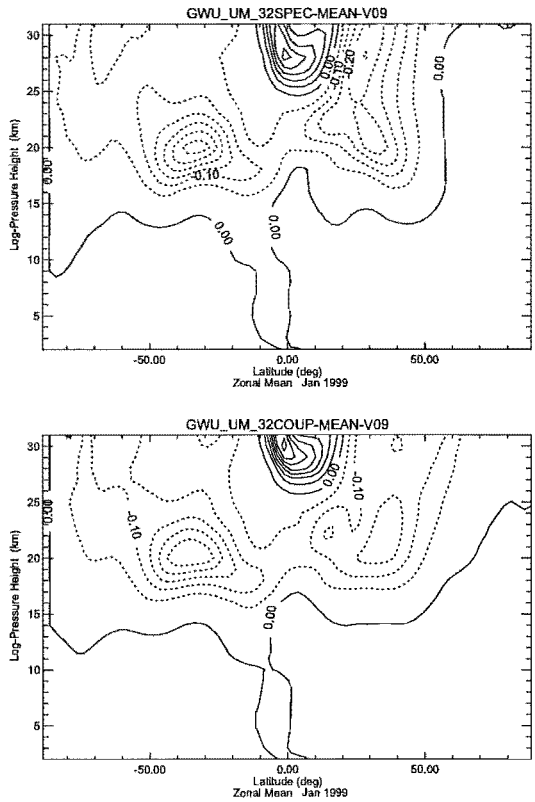

Figure 5.9: GW acceleration in January for *spectral* (top) and *coupled* (bottom) due to DSP. Contour interval is 0.05 m/s/day.

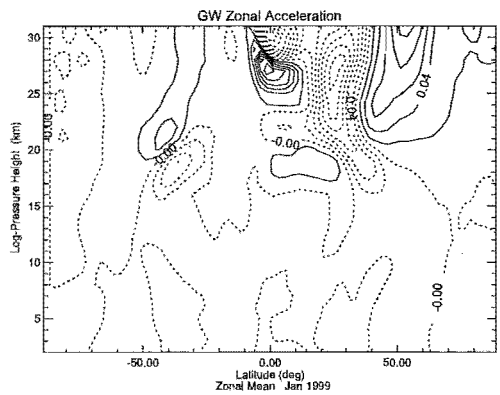

Figure 5.10: Difference in GW acceleration in January between *spectral* and *coupled* due to DSP. Contour interval is 0.02 m/s/day.

of zonal acceleration due to saturation of the orographically induced GWs for January is quantified in figure 5.11.

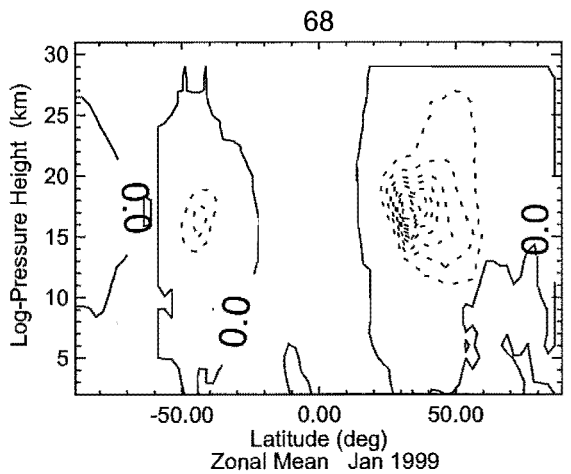

Figure 5.11: Zonal mean forcing due to 'saturation' of orographically induced GWs in *spectral* averaged over six years. Contour interval 0.5 m/s/day.

Figure 5.11 demonstrates that the forcing produced due to saturation of independently propagating orographic GWs in the *spectral* is quite substantial, amounting to -2 m/s/day. The value is also comparable to the values reported by (*Lilly et al.*, 1982). The relatively strong orographic gravity wave forcing acting independently in the *spectral* scheme damps the zonal mean wind.

A similar calculation for the *original* was also done to show that the 'saturation' of the orographic GWs produced the same amount of drag as compared to the *spectral*, as shown in fig. E.2.

This drag observed in both *spectral* and *original* is responsible for the damping of zonal mean zonal wind and also warmer temperatures in the midlatitude tropopause, which is absent in the *coupled*.

The stronger orographically-induced GW forcing in the *spectral* parameterization near the tropopause, in comparison to the *coupled* scheme, gives rise to a stronger residual mean circulation in that region. This is because of Coriolis forcing which drives the residual mean circulation, and plays an important role in momentum balance in the extratropical troposphere, as shown in table 5.1.

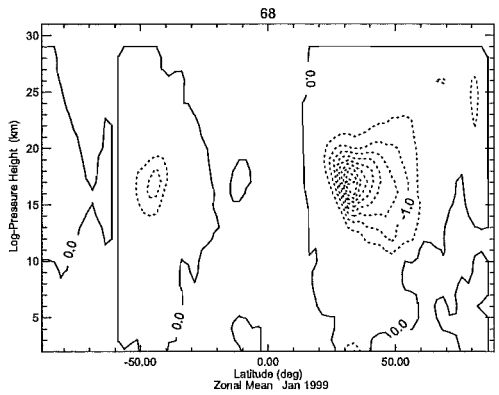

Figure 5.12: 6 years monthly mean ofzonal mean GW acceleration produced due to 'saturation' in *original* for January. Contour interval is 0.5 m/s/day.

Latitudes	$\frac{uu_\lambda}{a\cos\phi}$	$\frac{v(u\cos\phi)_\phi}{a\cos\phi}$	$-fv$	$\frac{\Phi_\lambda}{a\cos\phi}$	wu_z	X
0^0	0 ± 0.13	0.3 ± 0.36	0.02 ± 15	0.0 ± 14	-0.1 ± 0	-0.22 ± 0
50^0	0 ± 0.652	-0.37 ± 0.32	0.96 ± 12.7	0 ± 12.6	0.15 ± 0.25	-0.74 ± 0.3

Table 5.1: Zonal momentum budget at 15 km km at 0^0 and 50^0 latitude for northern hemisphere winter. The units are 86400 m/s/day, values less than 0.01 m/s/day are omitted.

Thus, the difference in GW acceleration is expected to bring a difference in the residual mean circulation in the troposphere between the two simulations. This is displayed in figure 5.13 which presents the six year average residual mean circulation for January for both the *spectral* and *coupled* simulations, and the difference between them.

From figure 5.13 it can be observed that both the *spectral* and *coupled* simulations show two thermally direct cells in the northern hemisphere troposphere, which is also discussed by *Holton* (1992). The difference in residual mean circulation, or diabatic circulation, between the two simulations not only shows a stronger circulation in the *spectral* at the lower troposphere but, a stronger sinking motion in the upper troposphere region can also be identified in it.

Due to its stronger residual mean circulation in the extratropical troposphere, the *spectral* simulation displays a warmer temperature than the *coupled*. A similar feature has also been observed by *McFarlane* (1987), *Milton and Wilson* (1996), *Gregory et al.* (1998) and *Yang et al.* (2000) by applying an orographic GW parameterization in their respective

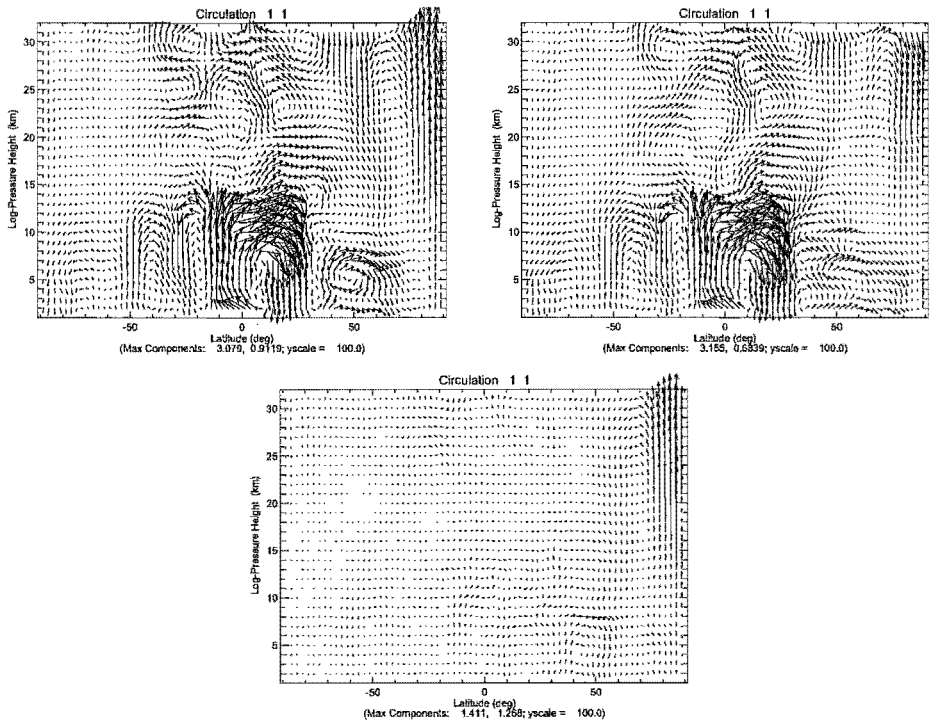

Figure 5.13: Mean meridional circulation for the month of January in *spectral* (left) and *coupled* (right) simulations and their difference (bottom). The vertical winds have been scaled by 100.0 and maximum components appear below each plot.

models.

The difference in GW acceleration between the *spectral* and *coupled* simulations, as shown in the previous section, affects tropospheric diabatic circulation. In addition, it can also induce changes in the meridional circulation, which can be verified by analyzing the terms of the zonal momentum balance equation from table 5.1. This reveals that the zonal momentum in the upper troposphere at the tropics and mid-latitudes is balanced by the Coriolis force $(-fv)$, mean meridional drift $(\frac{v(u\cos\phi)_\phi}{a\cos\phi}$ and $wu_z)$ and zonal acceleration (X) contributed by GWs, transient waves, and eddy forcings.

Hence, a change in X can also influence the meridional and vertical circulation in the troposphere, which can be represented by the Hadley and Ferrel cells (*Holton*, 1992) shown in figure 5.14. The reason behind studying the diagnostics for the month of January is that the meridional circulation in winter is much stronger than in summer, especially in the northern hemisphere (*Holton*, 1992). Also, saturation of orographic GWs produces the strongest acceleration during this period in the northern hemisphere.

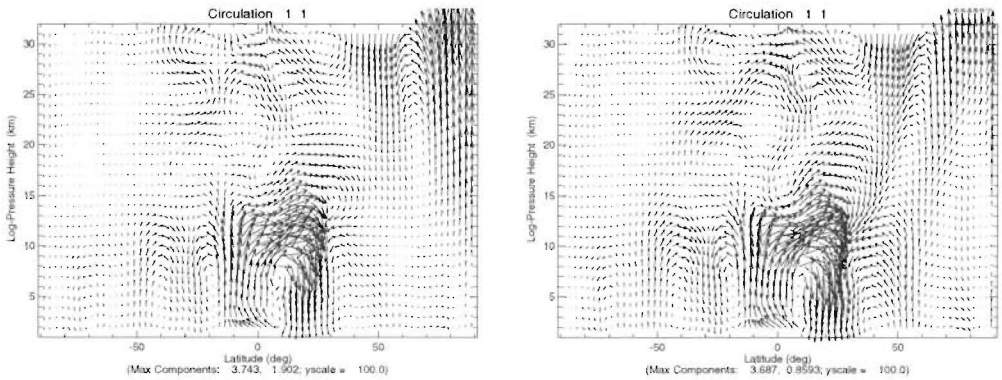

Figure 5.14: Mean meridional circulation for the month of January in *spectral* (left) and *coupled* (right) simulations. The vertical winds have been scaled by 100.0 and maximum components appear in the figure legend.

Figure 5.14 shows the presence of a thermally direct cell, also known as the Hadley cell, in the northern hemisphere tropics of both *spectral* and *coupled* simulations. Thermally indirect Ferrel cells can also be identified in the mid-latitudes of both simulations. It is noted that the Ferrel cell in the *coupled* simulation is stronger than that in the *spectral*. Similar circulations are also displayed in the southern hemisphere, although their strength is less than their northern hemisphere counterparts.

It is stated by *Holton* (1992) and *Grotjahn* (1993) that the tropical Hadley cell and mid-latitude Ferrel cell are driven mainly by diabatic heating, and eddy heat and momentum flux. The eddy heat and momentum flux can be quantified by calculating the divergence of EP-flux (explained in *Appendix C*). The EP-flux divergence for both the *spectral* and *coupled* simulations is presented in figure 5.15.

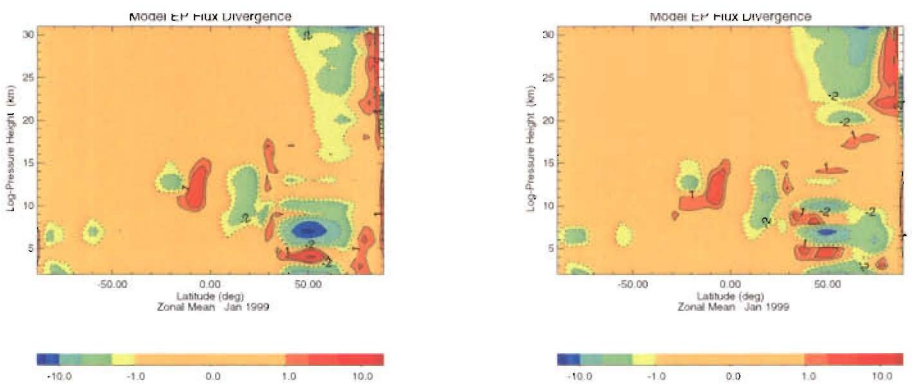

Figure 5.15: EP-flux divergence in *spectral* (left) and *coupled* (right) for the month of January. The contours are in logarithmic scale with contour intervals ranging from -20, -15, -10, -5, -2, -1, 1,2,5,10,15,20 m/s/day.

Monthly mean EP-flux divergence, in figure 5.15, is calculated by averaging daily EP-flux divergence values for the month of January. Figure 5.15 displays a strong convergence of EP-flux (negative values) that can be identified below 15 km in the northern hemisphere mid-latitudes in both the *spectral* and *coupled* simulations. Comparison of the values in that region show that the *spectral* simulation has a stronger convergence than that of the *coupled*.

The stronger EP-flux convergence value of the *spectral* simulation is linked with the stronger residual mean circulation, as on a seasonal time scale the zonal force due to the EP-flux divergence is nearly balanced by the Coriolis force part of the residual mean meridional function (*Holton*, 1992).

The GW acceleration in the northern hemisphere winter troposphere has induced differences in the tropospheric circulation between the *spectral* and *coupled* simulation. A detailed study has also been done on the southern hemisphere summer region. Due to the absence of land-sea contrast no noticeable difference has been found.

5.4 Comparison of *Spectral* and *Coupled* during southern hemisphere winter

To identify similar features during the southern hemisphere winter the zonal mean wind and temperature for both the *spectral* and *coupled* simulations are studied for July. Zonal mean wind and temperature for the *spectral* scheme and difference between the *spectral* and the *coupled* simulations for July are presented in figures 5.16 and 5.17.

It is apparent that there is no difference in the southern hemisphere zonal mean wind. However, a difference of approximately 3 K in temperature at the northern hemisphere polar latitudes can be seen in figure 5.17. This is again due to the saturation of orographic GWs in the *spectral* simulation as shown in figure 5.18. It is noteworthy that the orographic GW acceleration has decreased considerably during July at the same latitudes. The forcing produced by orographic GWs depends upon the background wind that filters them out (*Gregory et al.*, 1998). Hence, due to the weaker westerly jets in the troposphere during summer, the GW forcing has also weakened considerably. A similar feature has also been identified by *Osprey* (2001).

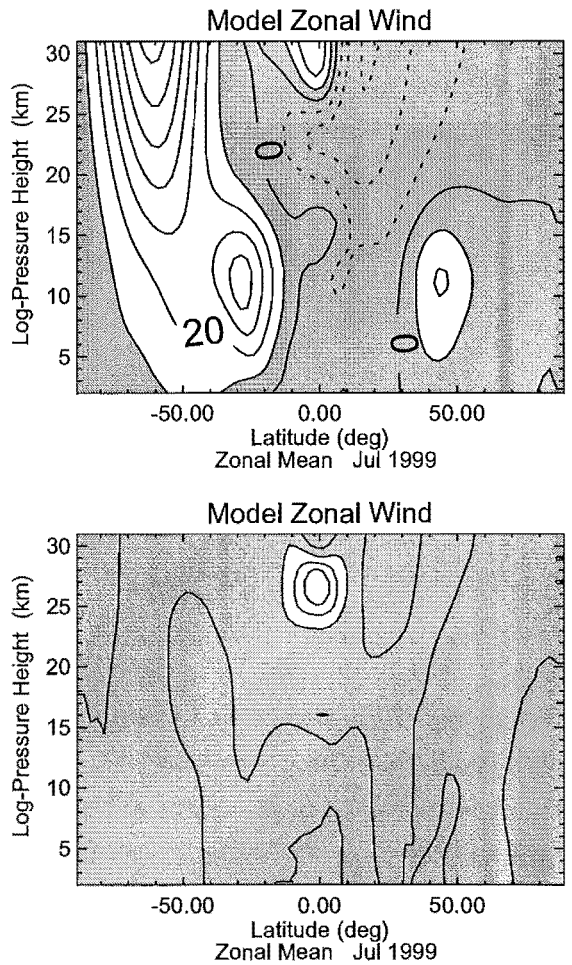

Figure 5.16: Zonal mean zonal wind for the *spectral* (top) and difference between *spectral* and *coupled* (bottom) for July averaged over six years. Contour interval is 10 m/s and 4 m/s respectively.

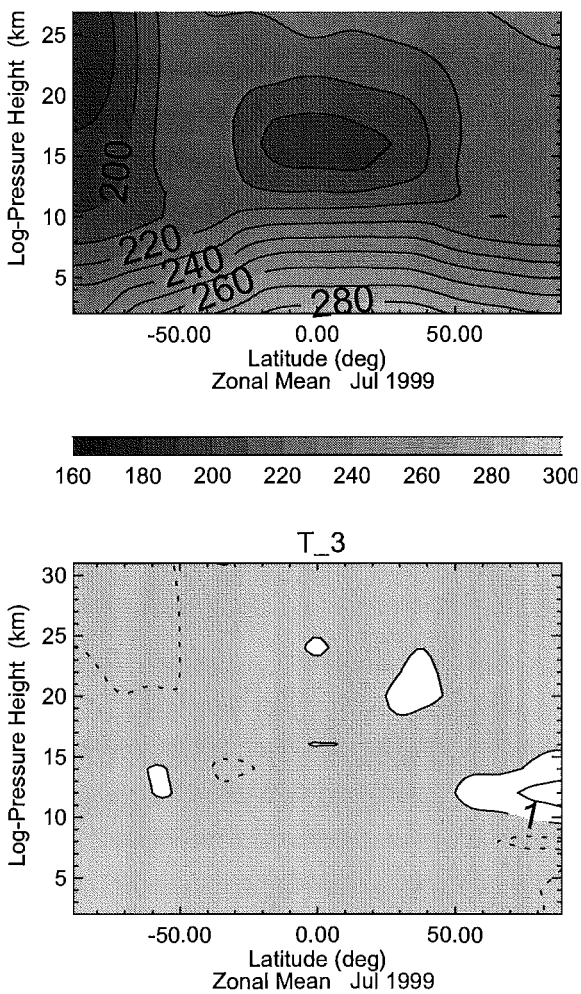

Figure 5.17: Zonal mean zonal temperature for the *spectral* (top) and difference between *spectral* and *coupled* for July (bottom) averaged over six years. Contour interval is 10 K and 2 K respectively.

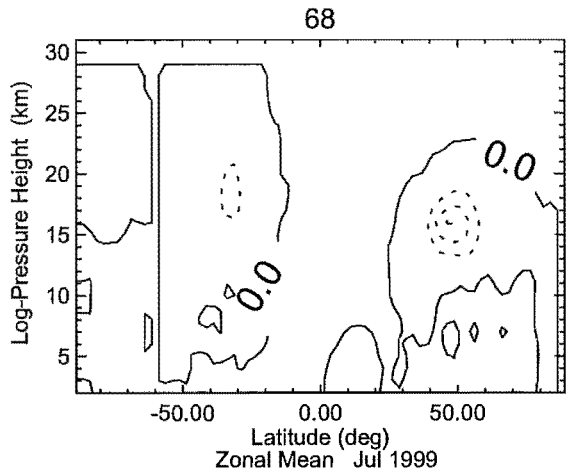

Figure 5.18: Zonal mean forcing due to 'saturation' of orographically induced GWs in *spectral* averaged over six years. Contour interval 0.5 m/s/day.

However, no difference in the zonal wind and temperature fields is identified in the southern hemisphere due to the scarcity of orographic features and very little land-sea contrast (*Gel*, 1992).

5.5 Summary

A qualitative comparison of the results from the *original* simulation and UKMO assimilated data has indicated a need for a better parameterization of GWs in the UM than the present one. The *spectral* and *coupled* schemes are incorporated in the UM and their effect in the troposphere and the lower stratosphere of the UM are studied in detail.

It can be summarized from the above study that GW acceleration differs considerably between the *spectral* and *coupled* schemes. In the northern hemisphere mid-latitudes, a damping of zonal wind and warmer temperature is observed in the *spectral* simulation during winter. The results show that this damping of zonal mean wind is caused by acceleration due to 'saturation regime' of independently acting orographic GWs in the *spectral* parameterization scheme.

The orographic part of the *coupled* orographic and broad spectrum waves breaks down at a relatively higher altitude, as shown in the the previous chapter with the aid of the test-bed. Hence, a similar effect in the tropospheric circulation is not identified in the

coupled simulation.

The stronger GW drag in the *spectral* scheme induces a stronger residual mean circulation in the mid-latitude troposphere in the *spectral* which increases the temperature at that region. The change in GW forcing in the troposphere also changes the forcing produced by resolved waves, which is observed to be stronger in the *spectral* as compared to the *coupled* scheme. No significant differences between the *spectral* and *coupled* schemes were seen during summer, nor were any differences observed in the southern hemisphere simulations.

It can therefore be inferred that the dynamics of the troposphere in the UM is sensitive to the two different GW parameterization schemes. In the following chapter the sensitivity of the middle atmosphere to GW parameterizations is discussed in detail.

Chapter 6

The Sensitivity of the Unified Model's Stratosphere

6.1 Introduction

The sensitivity of the UM's troposphere to changes in GW parameterization has been studied in the previous chapter, using *spectral* and *coupled* schemes. In this chapter, the behaviour of the model's middle atmosphere is analyzed using these parameterization schemes.

The results obtained from the *spectral* simulation are compared and contrasted qualitatively with the UKMO assimilated data in the next section before moving on to subtler differences between simulations using the different schemes. It should be noted in this context that UKMO assimilated data is one of the standard sets of data which has been used by, *Swinbank et al.* (1998), *Butchart and Austin* (1998), *Randel et al.* (1999), *Rep* (2001) and *Gregory et al.* (1998), to compare their respective model results. It is worth mentioning here that the UKMO assimilated data extends approximately only up to the stratopause, 56 km or 0.3 hPa.

The seasonal variation of the zonal mean wind and temperature in the middle atmosphere, as obtained from simulations using the two schemes are compared in section 2. The effect of differences in GW acceleration on model behaviour are also discussed, in the context of dynamical processes such as the Stratospheric Sudden Warming (SSW), equatorial oscillations and residual mean circulation.

Sensitivity results for the UM have already been presented by *Swinbank et al.* (1998), *Gregory et al.* (1998) and *Butchart and Austin* (1998). In these studies, the UM was simulated with different model lid heights and vertical resolutions. They used GW parameterization schemes based on *Gregory et al.* (1998) that extend up to 27 km; and above that height the Rayleigh friction scheme was used. The present work also reports results from the simulation of the UM with similar GW parameterization schemes in *Appendix D*. However, the main difference between these reports and the present work is the height

of the model lid, which extends up to 80 km, and the different GW parameterization schemes used.

The UM has been run over a period of six years with each parameterization scheme. Although this is a relatively short integration period for a GCM, it was reported by *Swinbank et al.* (1998), based on a 5 year model run, that the UM can successfully simulate the dynamic characteristics of the middle atmosphere within that span of time.

6.2 Comparison of the UKMO data with the results of *spectral* simulations

The results of the six year UM integration with *spectral* scheme, are compared with the UKMO assimilated data, (*Swinbank and O'Neill*, 1994). The UKMO data used for this study is also a six year average monthly mean data set. Diagnostic fields such as, zonal mean zonal wind, zonal mean temperature, zonal mean meridional wind, and zonal mean vertical wind for the months of January and July are qualitatively compared in the present section. As the UKMO assimilated data extends approximately only up to the stratopause, 56 km or 0.3 hPa, many features of the model which appear above 56 km cannot be compared with the data set.

The zonal mean zonal velocities for the months of January (the left hand side) and July (the right hand side) for UKMO data and *spectral* simulations (top to bottom) are shown in figure 6.1, respectively. This order has been maintained for all subsequent figures in the present section.

The zonal mean zonal wind in January and July show reasonably similar westerly wind shear in the troposphere in both hemispheres. However, the polar night jets in the northern hemisphere winter stratosphere show differences. The *spectral* simulation shows a stronger and more vertically upright jet compared to the UKMO data. This indicates a more stable stratosphere in the *spectral* simulation and hence lesser GW activity than that of the assimilated data.

One of the features of the *spectral* simulation in figure 6.1 is that polar stratospheric jet closes off in the mesosphere. This feature is produced by a successful representation of GW acceleration which induces a diabatic circulation in the polar middle atmosphere of

the *spectral* simulation. Another interesting feature that is not observed in the UKMO assimilated data is the alternating easterly and westerly wind in the tropics. This feature may be linked with the model's representation of QBO and SAO, which are discussed in detail in Chapter 8.

The strength of the January easterly jets in the southern hemisphere are similar for both cases. The zonal mean wind fields for the *spectral* simulation in July compare very well with the UKMO zonal wind fields in both hemispheres.

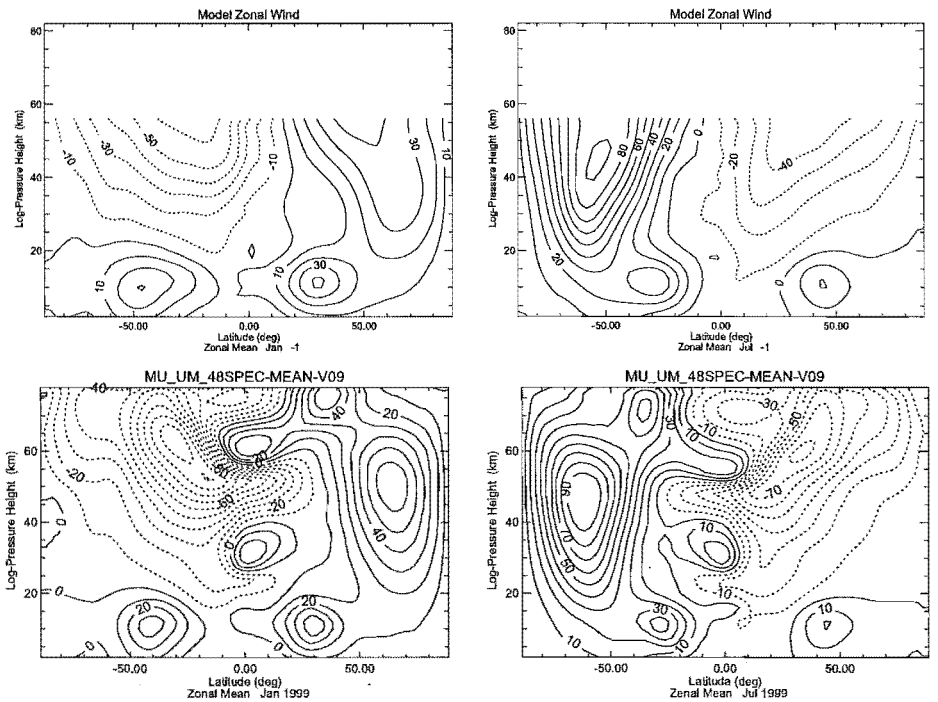

Figure 6.1: Zonal mean zonal wind for (top to bottom) UKMO data, *spectral* simulation for January (left) and July (right). The plots extend up to 80 km in $y-$ axis. Contour interval 10 m/s.

The zonal mean temperature fields are shown in figure 6.2. The temperature for the northern hemisphere lower stratosphere shows marked differences in January across the two cases. In comparison to the assimilated data, the minimum lower stratosphere temperature occurs higher in the atmosphere in the *spectral* simulation. The southern hemisphere January temperature fields agree very well with each other. There is a temperature inversion in the mesosphere observed in the *spectral* simulation which is again induced by the model's GW drag.

The temperature fields for July in the simulated results compare well with the assimi-

lated data, though the stratosphere is colder in the *spectral* simulation. This feature has been observed in many GCMs and has been reported widely by *Swinbank et al.* (1998), *Butchart and Austin* (1998), *Pawson et al.* (1998), *Langematz and Pawson* (1997), *Pope et al.* (2000), *McLandress* (1998) and *Yang et al.* (2000). The colder stratosphere in the model might be related to radiative heating of the model. *Pope et al.* (2000) have performed some experiments to improve this feature in the UM.

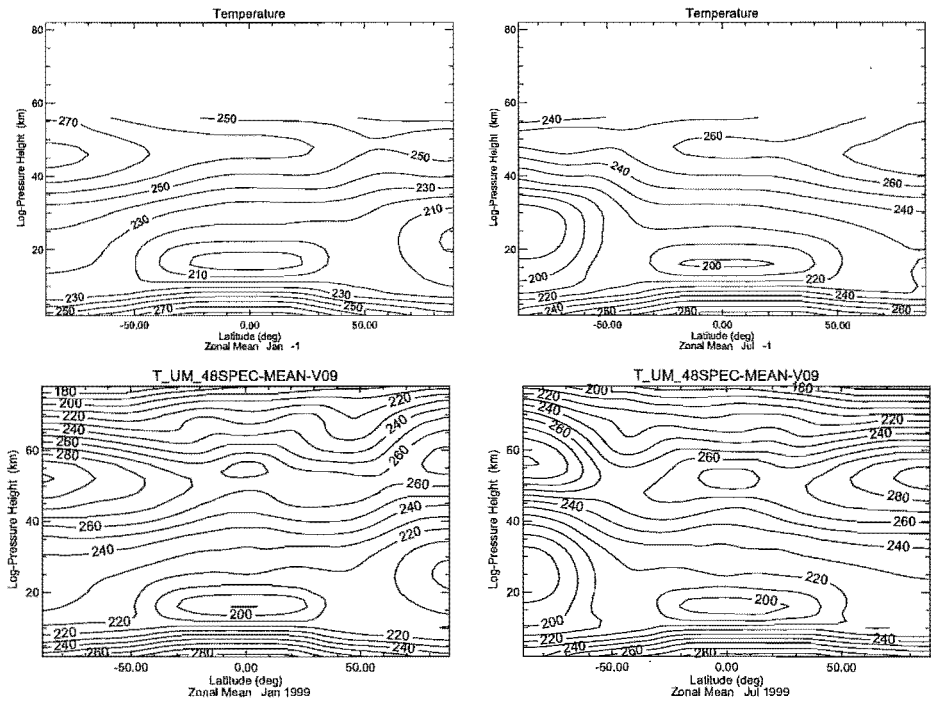

Figure 6.2: Zonal mean temperature for (top to bottom) UKMO data, *spectral* simulation for January (left) and July (right). Contour interval 10 K.

Figure 6.3 shows the mean meridional velocity for the UKMO data and the *spectral* simulation for the months of January and July. The January northern hemisphere polar region in assimilated data shows a positive wind shear that is not observed in the *spectral* simulation. Another difference between the two cases is the strength of the mean meridional velocity, which is greater in the assimilated data sets. This can again be related to the weaker GW acceleration in the middle atmosphere of the *spectral*.

The other features such as the positive wind shear in the tropical troposphere and stratopause region, observed in the UKMO data, is well represented in the *spectral* simulation. It also demonstrates a positive wind shear in the mesosphere from the southern hemisphere polar region to the northern hemisphere pole for the month of January and a

negative meridional flow from the northern hemisphere pole to the southern hemisphere pole for the month of July. This motion in the middle atmosphere is related to the diabatic circulation as described in Chapter 2.

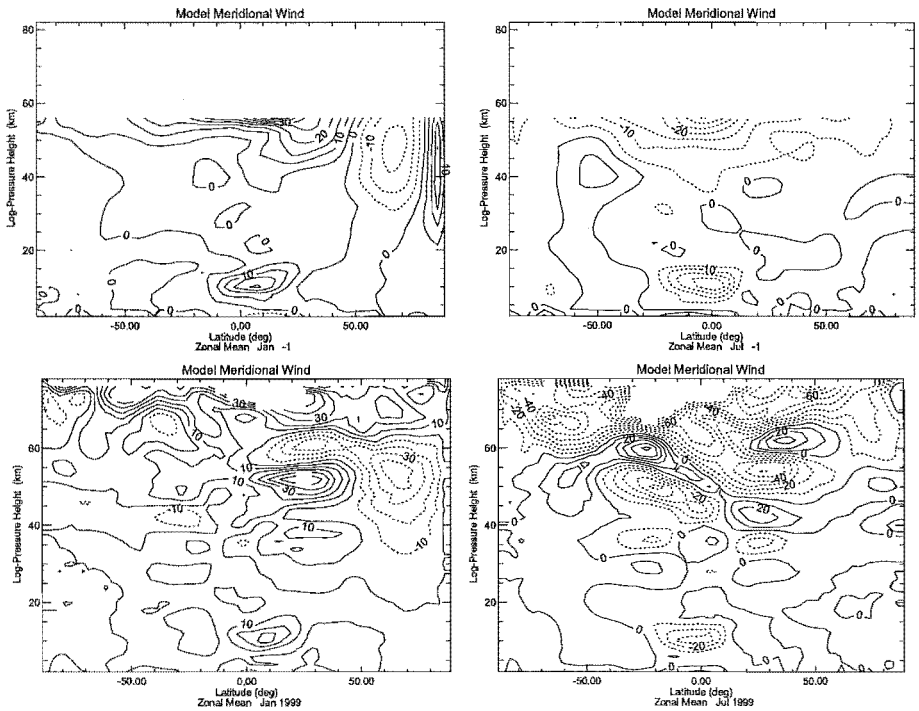

Figure 6.3: Zonal mean meridional wind for (top to bottom) UKMO data, *spectral* simulation for January (left) and July (right). Contour interval for the UKMO data is 5 decimeter/s and *spectral* is 10 decimeter/s.

The diabatic circulation as diagnosed using the zonal mean meridional velocity can also be identified in the zonal mean vertical velocity. Zonal mean vertical velocity for January and July are shown in figure 6.4 for the UKMO assimilated data and the *spectral* simulation. The contour intervals for the UKMO vertical velocity fields are 1 mm/s, while for the the *spectral* simulation is 5 mm/s.

The upwelling and the sinking features in the stratosphere, seen in the northern and southern hemispheres during both January and July, are related to the diabatic circulation. This feature can not be identified in the UKMO data as it extends only up to a height of 56 km.

However, a careful examination of these fields shows that the negative vertical velocity of the UKMO data in the northern and southern hemispheres during January and July

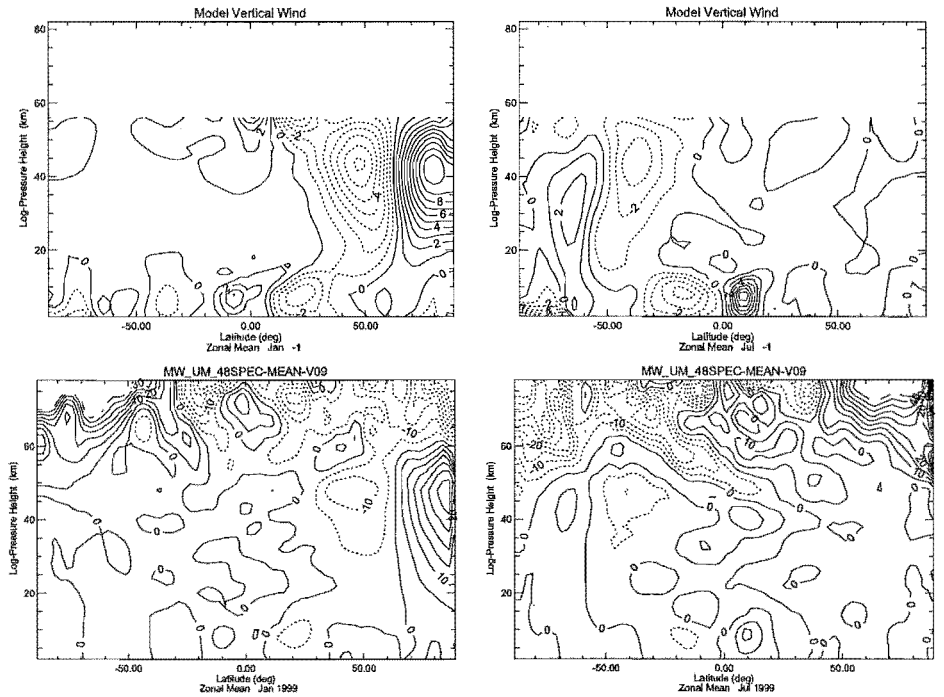

Figure 6.4: Zonal mean vertical wind for (top to bottom) UKMO data, *spectral* simulation for January (left) and July (right). Contour interval for UKMO assimilated data is 1 mm/s and for *spectral* is 5 mm/s.

is stronger than its counterpart in the *spectral* simulation. It can be related again to the weak GW acceleration in the model which is unable to induce strong vertical motion connected to the downward control process.

In January, there is an upward motion in the northern hemisphere polar stratosphere in all three cases which may be connected to a Statospheric Sudden Warming (SSW) event in the northern hemisphere winter stratosphere.

This qualitative study has revealed that there are several features in the *spectral* simulation that concur with the UKMO assimilated data. There are a few other features, such as the strength of zonal mean zonal wind speed and alternating easterlies and westerlies which do not agree very well with the UKMO assimilated data. Due to the lack of availability of assimilated data fields above 56 km, dynamical features in the mesosphere, such as the diabatic circulation, could not be compared with the model results.

It can be summarized here that the overall dynamic characteristics of the middle atmosphere are well represented by the model when simulated with the *spectral* scheme. Although the effect of a weak GW acceleration can be identified in a weak diabatic cir-

culation in the *spectral* simulation, the results successfully demonstrate the closing of easterly and westerly jets in both hemispheres during summer and winter.

In the next section, we move on to compare the results from the *spectral* run with the more complex *coupled* simulation to identify whether a change in GW acceleration (as reported in Chapter 4) has any effect on dynamical processes in the middle atmosphere.

6.3 Sensitivity of the Unified Model's middle atmosphere

6.3.1 Northern hemisphere winter

Figure 6.5 shows a six year average of monthly mean zonal wind climatology based on the *spectral* and *coupled* simulations and the difference between them for January. Preliminary examination of the results shows that the northern hemisphere winter westerly is much stronger in the *spectral* simulation than that of the *coupled.* The values of the easterly wind fields in the southern hemisphere summer are similar for both cases.

The polar night jets have also moved towards the North pole in the *spectral* simulation which can be identified from the dipole feature in January at an altitude of approximately 60 km. A stronger westerly in the *coupled* simulation at lower stratosphere and upper troposphere is also noticed during the same time in the northern hemisphere.

The six-year climatological average zonal mean temperature for the *spectral* and the *coupled* simulations, and their differences, are shown in figure 6.6. On initial examination of figures 6.6, the only apparent difference that can be noticed is that the *coupled* simulation is relatively warmer in the northern hemisphere stratosphere. Also, the equatorward gradient of the temperature above the stratosphere in the *spectral* simulation is greater than that of *coupled.* This explains the stronger polar night jet in the *spectral* simulation via the thermal wind relation as explained in Appendix 2.

The difference between the *spectral* and *coupled* simulations shows a dipole feature in the winter middle atmosphere. This suggests that the stratosphere has warmed up considerably and the mesosphere has cooled down in the *coupled* simulation compared to the *spectral,* producing an effect of descending stratopause. This feature indicates that the winter middle atmosphere in *coupled* simulation is more disturbed or unstable than that of *spectral.*

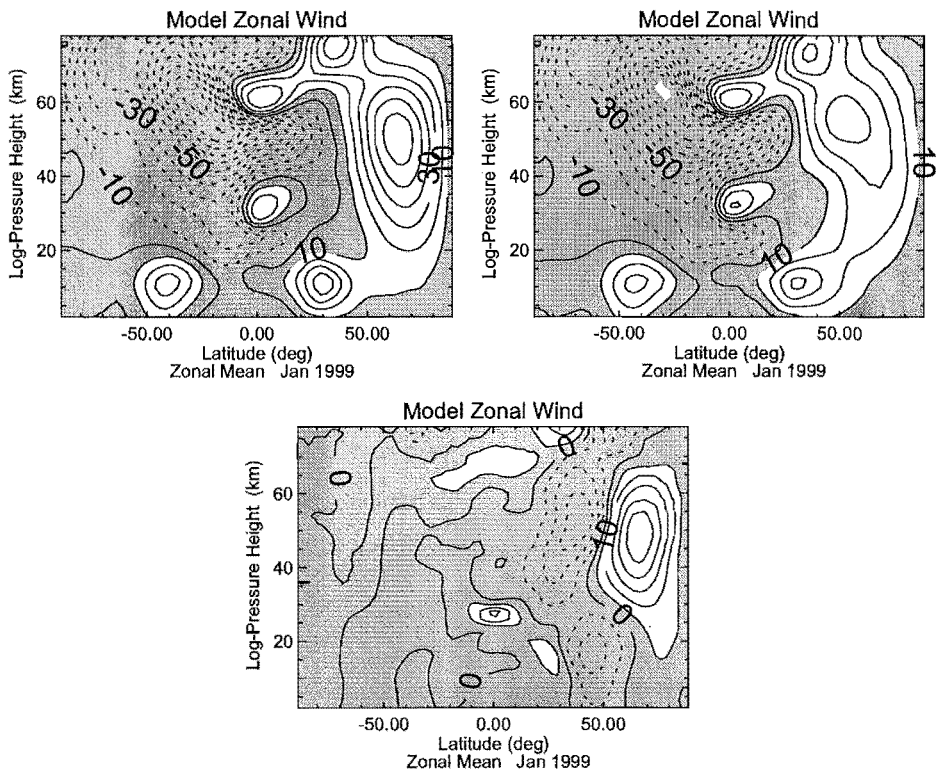

Figure 6.5: Zonal mean zonal wind for the *spectral* (top left), *coupled* (top right) run averaged over six years and the difference (bottom) between them for January. Contour interval is 10 m/s and 5 m/s for the difference.

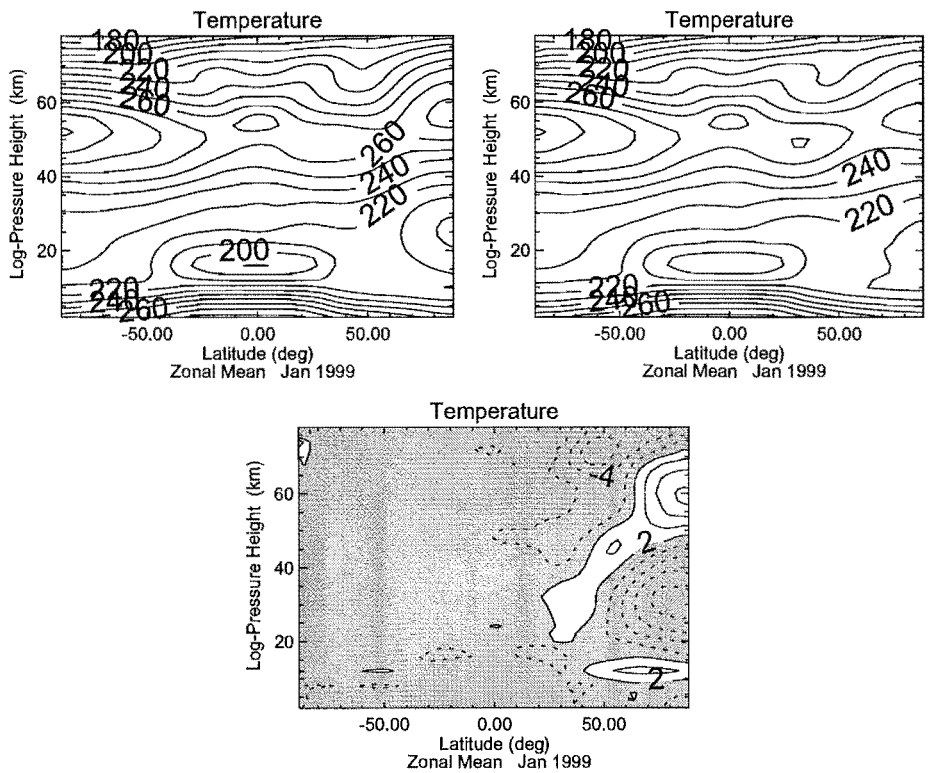

Figure 6.6: Zonal mean zonal temperature for the *spectral* (top left) and *coupled* (top right) runs averaged over six years and difference (bottom) between them for January. Contour interval is 10 K and 3 K for the difference.

In order to verify that the disturbance in the middle atmosphere of the *coupled* simulation is greater than the *spectral* simulation, standard deviations of the zonal mean wind for both simulations during January are studied. A similar test has also been reported by *Lawrence* (1997b). Figure 6.7 shows the standard deviation of the zonal mean wind for both the *spectral* and *coupled* simulations for the month of January.

Figure 6.7 clearly demonstrates the differing nature of the simulations. The *spectral* simulation shows a much lesser variability than that of the *coupled* simulation. The *spectral* simulation also shows maximum variability around the single polar night jet and at the tropics, whereas the inter-annual variability in the *coupled* simulation displays two peaks of variability in the northern hemisphere. The less prominent variability in the *spectral* simulation compared to the *coupled* simulation indicates a lack of early and midwinter warmings in the *spectral* simulation which has also been observed by *Butchart and Austin* (1998). It should be pointed out, in this context, that the SSW events for both the simulations are studied in detail in the next chapter.

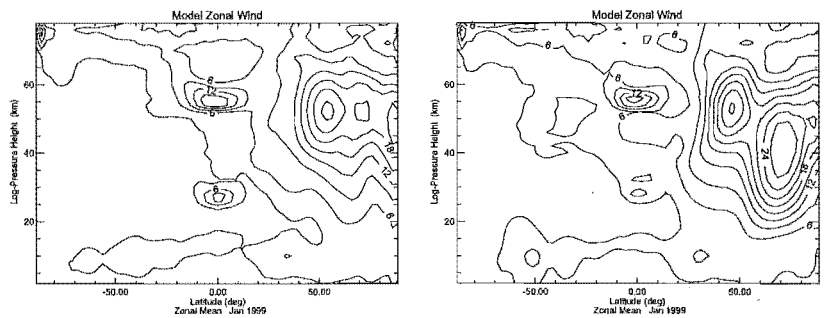

Figure 6.7: Standard Deviation of January zonal mean wind for *spectral* (left) and *coupled* (right) simulation. Contour interval is 3 m/s.

Hence, it can be interpreted that the northern hemisphere polar middle atmosphere shows maximum interannual variability in zonal mean wind compared to the southern hemisphere for both the *spectral* and *coupled* simulations. It should also be noted that less prominent variability in the *spectral* simulation, compared to the *coupled* simulation, in the northern hemisphere, may indicate a relative lack of early and midwinter warmings in the *spectral* (*Butchart and Austin*, 1998).

The characteristics of the zonal mean wind and temperature in both the *spectral* and *coupled* simulations, as well as their differences, are caused by their parameterized GW

accelerations. However, before analyzing the difference in GW acceleration between the *spectral* and *coupled* simulations, it is necessary to know the processes that balance the forcing induced by GW acceleration in the extratropical middle atmosphere.

Table 6.1 shows zonal momentum balance terms for the northern and the southern hemisphere mid-latitudes during January for the *spectral* simulation. It should be clarified here that table 6.1 is provided only to show the dynamical processes that balance the forcing induced by GW acceleration in summer and winter middle atmosphere extratropics, and not to compare the difference in GW acceleration between the two simulations.

Latitude	$\frac{uu_\lambda}{a\cos\phi}$	$\frac{v(u\cos\phi)_\phi}{a\cos\phi}$	$-fv$	$\frac{\Phi_\lambda}{a\cos\phi}$	wu_z	X
50^0 N	0 ± 0.12	-8.23 ± 0.1	16.1 ± 11.0	0 ± 6.5	7.84 ± 0.03	-15.71 ± 3.95
50^0 S	0 ± 0.69	-0.61 ± 0.15	-10.1 ± 12.6	0 ± 12.7	0.34 ± 0.025	9.83 ± 0.3

Table 6.1: Zonal momentum budget at 75 km and 50^0 N and 50^0 S during January for *spectral* simulation. The units are 86400 m/s/day, values less than 0.01 are omitted.

It is obvious from the terms in table 6.1 that forcing due to GWs in the middle atmosphere extratropics is mainly balanced by Coriolis forcing in both summer and winter. However, meridional and vertical advection terms also play an important role in maintaining the zonal momentum balance.

Another important point to note, here, is that the acceleration produced by GWs in the extratropical winter hemisphere middle atmosphere is easterly (negative). This acceleration induces a forcing opposite to the zonal westerly flow and is responsible for weakening of polar night jet in the winter hemisphere as shown in figures 6.5. GW acceleration in the middle atmosphere extratropical summer hemisphere is westerly (positive), which is again opposite to the direction of easterly zonal mean wind. This forcing due to this acceleration contributes to the weakening of easterly zonal wind jets in the mesosphere during summer.

These features are exhibited in figure 6.8 which shows zonal mean GW acceleration for the *spectral* and *coupled* simulations, and the difference between them, respectively, in logarithmic scale during January.

In figure 6.8, a striking difference in the strength and position of GW acceleration be-

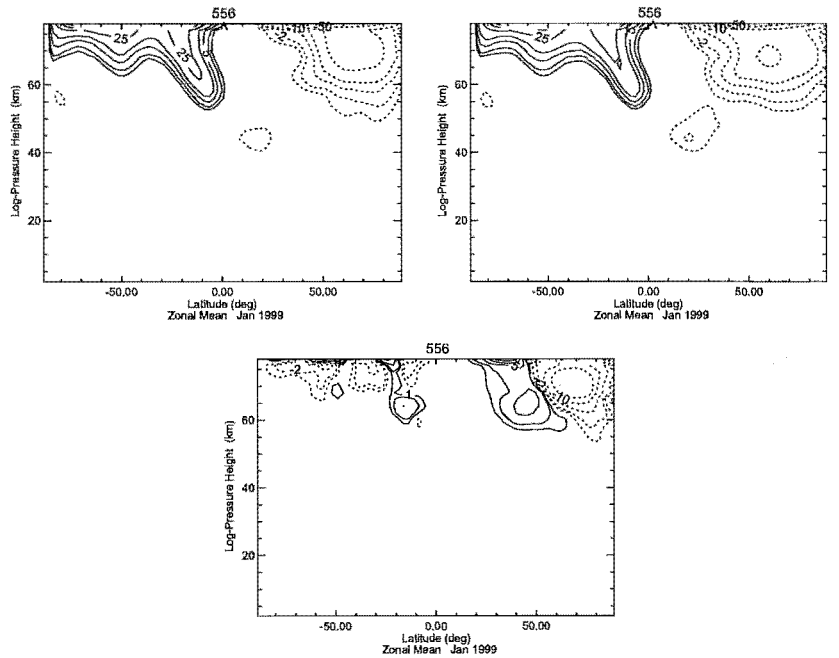

Figure 6.8: GW acceleration in *spectral* (top left), *coupled* (top right) and the difference (bottom) between them for the month of January. The contours are in logarithmic scale with contour intervals for the first two plots going from (−100, −75, −50, −25, −10, −5, −2, −1, 1, 2, 5, 10, 25, 50, 75, 100) m/s/day. The contour interval for the final (difference) plot going from (−20, −15, −10, −5, −2, −1, 1, 2, 5, 10, 15, 20) m/s/day. The dotted lines indicate negative numbers.

tween the *spectral* and *coupled* simulations is observed. The GW acceleration is stronger towards the northern hemisphere polar region but is weaker in the extra-tropics for the *spectral* simulation. In the southern hemisphere, the *coupled* simulation shows a uniformly stronger acceleration than the *spectral*. However, the difference in the southern hemisphere is negligible in comparison to the differences in the northern hemisphere.

These features have been noted in the discussion of the single column test bed in Chapter 4. The waves in the *coupled* simulation start dissipating at a relatively lower altitude in the presence of orography than the *spectral* simulation. As a result, the magnitude of GW acceleration in *coupled* at the model's mesosphere is less compared to the *spectral* simulation. The GW acceleration in the *coupled* simulation at stratospheric levels is not evident from figure 6.8, due to the relatively higher density of the atmosphere in stratospheric levels than mesospheric levels (explained in Chapter 4, equation 4.1).

Residual mean circulation or diabatic circulation, as discussed in Chapter 2, is intimately connected to the GW circulation and causes a warm winter mesosphere and a cold summer mesosphere when solstice conditions prevail. This feature is displayed in both the *spectral*

and *coupled* simulations with the aid of figures 6.6. During January, both simulations show a warm mesosphere in the northern hemisphere polar latitudes and cold mesosphere in the southern hemisphere polar latitudes.

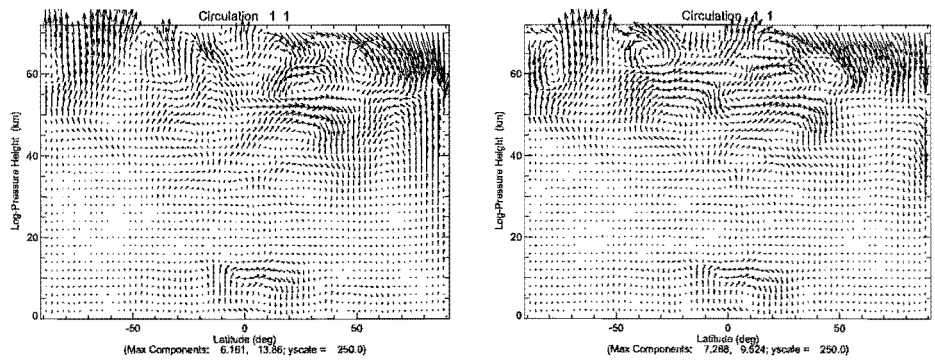

Figure 6.9: Residual mean circulation for the month of January in *spectral* (left) and *coupled* (right) simulations. The vertical winds have been scaled by 250.0 and maximum components appear in the figure legend.

Figure 6.9 shows the residual mean circulation for the *spectral* and *coupled* simulations for the month of January. The upward motion observed in the southern hemisphere mesosphere induces adiabatic cooling and the downward motion in the northern hemisphere induces adiabatic heating. This circulation plays an important role in altering the horizontal temperature gradient in the mesosphere of both the *spectral* and *coupled* simulations, which also contributes to the closing of polar jets in the mesosphere, (*Geller*, 1997).

The stratosphere in the *spectral* simulation (figure 6.9) exhibits a rising motion in the northern hemisphere pole. A similar feature is, however, not identified in the northern hemisphere stratosphere of the *coupled* simulation. This feature in *spectral* simulation may be associated with a SSW event during mid-January (which is explained in the next chapter), inducing an adiabatic motion in the northern hemisphere polar stratosphere (*Rosier et al.*, 1994).

The effect of stronger GW acceleration in the *spectral* simulation in the middle atmosphere of the northern hemisphere polar region can be perceived in the difference between the mean flow (zonal mean temperature and zonal mean wind) of the *spectral* and *coupled* simulations. The change in the mean flow of the middle atmosphere further affects large scale planetary waves in the atmosphere (*Andrews et al.* (1987) and *O'Neill and Pope* (1988)). Hence, apart from residual mean circulation, GW acceleration has a bearing on large scale planetary wave circulation.

According to linear wave theory (*Matsuno*, 1970) and (*Andrews et al.*, 1987), planetary waves propagate on a refractive index that is governed by background wind. Background wind can therefore be assumed as a wave guide that plays an important role in changing the direction of propagation of the planetary waves. *Lawrence* (1997a) also suggested that the effect of GWs can be interpreted as a 'damping' on the non-linear planetary waves. Although this feature has not been studied in detail in the present context, an interesting result is presented below.

To study the effect of GW acceleration on the planetary waves in the *spectral* and *coupled* simulations, the signature of planetary wave−1 is calculated based on monthly mean geopotential heights for January. A one-dimensional Fourier analysis is performed on the zonal mean geopotential height for the month of January.

The wave−1 signature in the geopotential height fields of the *spectral* and *coupled* simulations is presented in figure 6.10. The *spectral* simulation shows a smaller amplitude of wave−1 than the *coupled* simulation.

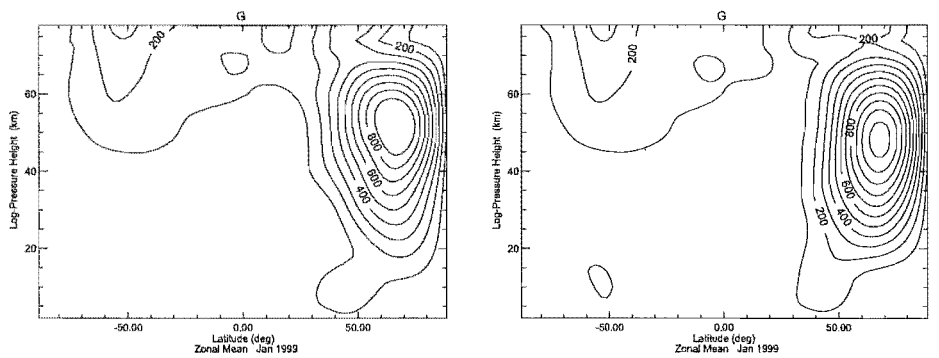

Figure 6.10: Wave−1 amplitude in geopotential height field for the month of January for *spectral* (left) and *coupled* (right) simulations respectively. Contour interval 100.

It should be further noted that the planetary wave amplitude in the southern hemisphere summer is negligible compared to the northern hemisphere winter middle atmosphere. The difference in planetary wave amplitudes in the *spectral* and *coupled* simulations critically affect the evolution of SSW events in the northern hemisphere winter middle atmosphere. A detailed analysis of the SSW is presented in Chapter 7.

It has been demonstrated in this section, that the difference in GW acceleration in the

winter hemisphere has affected the middle atmosphere circulation in the two simulations. The position of the GW acceleration and its strength for the *coupled* simulation (figure 6.8) has made the winter middle atmosphere more disturbed and unstable compared to the *spectral* simulation. The coupling of the broad spectrum and orographic GW has led to the dissipation of the coupled waves at a lower level compared to the uncoupled waves in the *spectral* simulation.

The summer hemisphere in this section has not displayed any noticeable difference. This can be attributed to the lack of orographic features and land-sea contrast in the Southern hemisphere. The orographic parts of the spectra in the *spectral* and *coupled* schemes have not played any important role in the southern hemisphere GW acceleration, and thus have not significantly affected the middle atmosphere circulation.

The next section discusses results from the southern hemisphere winter middle atmosphere. They have been studied in detail to analyze the effect of differences in GW acceleration between the two schemes.

6.3.2 Southern hemisphere winter

The strength and the position of the westerly wind fields in the southern hemisphere winter do not show much difference between the *spectral* and *coupled* simulations, as shown in figure 6.11. Once again this is due to the absence of orographic features in the southern hemisphere, which effectively limits the role of the orographic part of the spectrum in both schemes.

The easterly wind field in the summer hemisphere (figure 6.11) does not show any noticeable difference across the two schemes, in spite of the presence of orography. This feature has been discussed in Chapter 4 with the aid of test-bed.

The only difference in zonal mean zonal wind is seen in the tropical mesosphere, where a stronger westerly wind in the *spectral* simulation above an altitude of 70 km can be noticed. The seasonal variability in the wind fields of both the schemes can again be shown by using the six-year year mean standard deviation for July (figure 6.12).

Although the maximum variability in July simulations is displayed in the upper stratosphere at 50^0S, it is not as strong as that of the northern hemisphere winter variability,

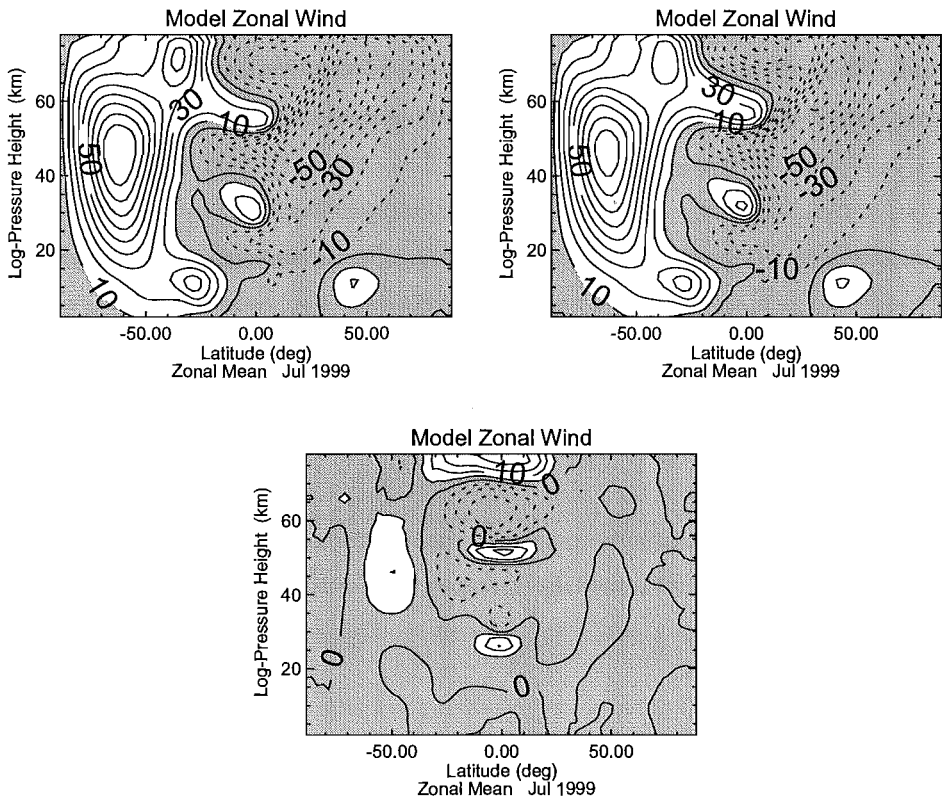

Figure 6.11: Zonal mean zonal wind for the *spectral* (top left), *coupled* (top right) run averaged over six years and the difference (bottom) between them for July. Contour interval is 10 m/s and 5 m/s for the difference.

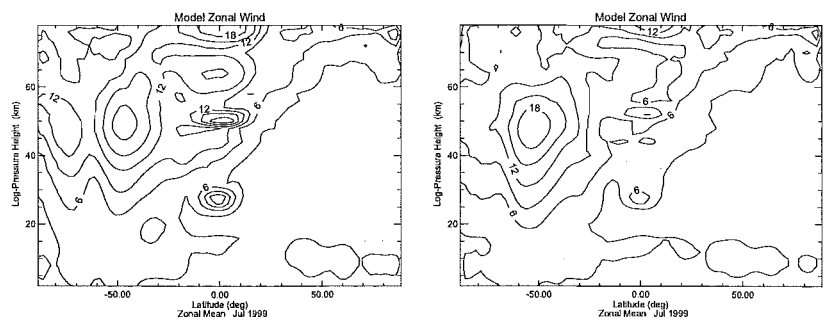

Figure 6.12: Standard Deviation of July zonal mean wind for *spectral* (left) and *coupled* (right) simulation. Contour interval is 3 m/s.

shown in figure 6.7. Also, unlike the northern hemisphere winter, there is no difference in the variability of the two simulations. It can therefore be stated that the southern hemisphere winter middle atmosphere is much more stable than that of the northern hemisphere's.

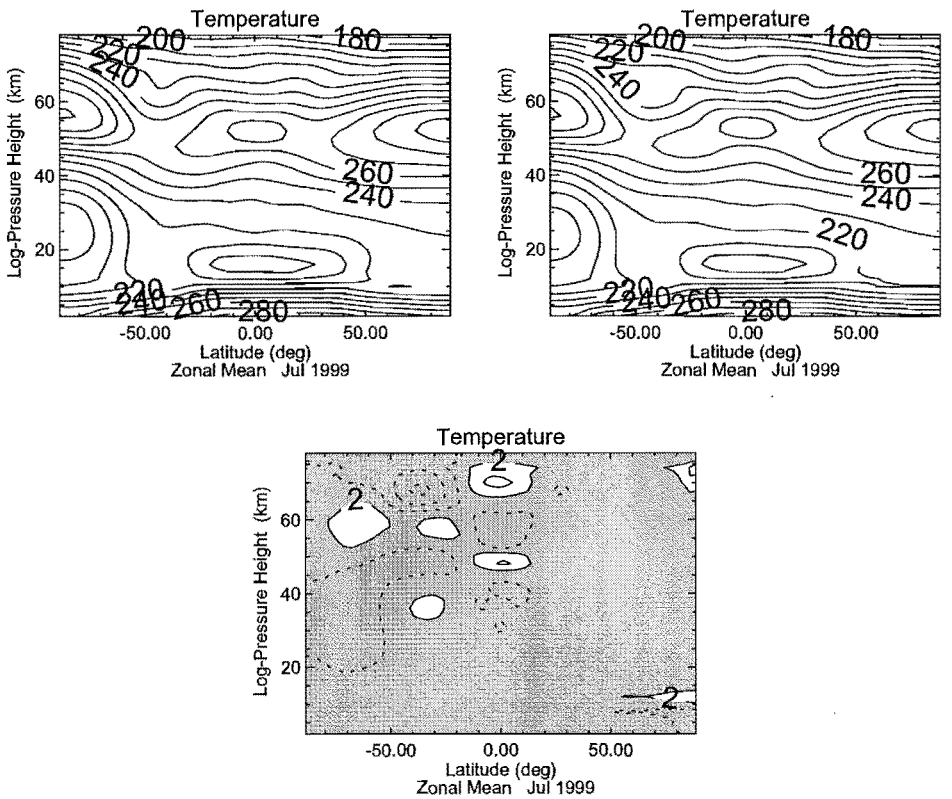

Figure 6.13: Zonal mean zonal temperature for the *spectral* (top left) and *coupled* (top right) simulations averaged over six years and difference (bottom) between them for July. Contour interval is 10 K and 3 K for the difference.

The zonal mean temperature for the two simulations, along with the difference between the two, for the month of July is shown in figure 6.13. The temperature field does not show any marked difference between the schemes; however, the mesosphere in the *coupled* simulation is colder in the mid-latitudes compared to the *spectral* simulation. The difference in temperature is also seen in the tropical mesosphere. This feature has been studied and is explained in the next chapter.

Zonal mean GW acceleration for the *spectral* simulation and the difference between the same fields for the *spectral* and *coupled* simulations are shown in figure 6.14. It is evident

from that the zonal GW acceleration in the southern hemisphere winter mesosphere is stronger for the *spectral* simulation than that of the *coupled*. The coupling of orographic and broad spectrum GWs has induced instability in the coupled waves at a much lower altitude than when uncoupled. In the *spectral* simulation, the GWs start depositing their momentum at a higher altitude than *coupled* simulation, and its effect gets magnified due to the reduced density in the atmosphere at that height. It is worth pointing out here that a similar feature has also been observed in the northern hemisphere winter and has been explained in the 'single column test-bed' in Chapter 4.

It has already been discussed that GW acceleration and diabatic circulation are closely related. A difference in GW acceleration in the winter mesosphere between the *spectral* and *coupled* simulations (figure 6.14) can therefore induce a difference in the residual mean circulation. Furthermore, the residual mean circulation is associated with adiabatic heating and cooling at the poles, which may lead to differences in the gradual warming of the mesosphere from winter to summer.

To study these effects, the residual mean circulation for both the *spectral* and *coupled* simulations during June is discussed in detail. The results for the other winter months are not displayed to avoid repetition. Figure 6.15 shows the six-year mean residual mean circulation for the two simulations and the differences between them.

It is evident that a rising motion in the northern hemisphere mesosphere is associated with the deposition of positive zonal acceleration, and a sinking motion in the southern hemisphere mesosphere is associated with the negative values of zonal acceleration, as shown in figure 6.15. The difference in the residual mean circulations of the two simulations is identified in the southern hemisphere middle atmosphere, where the *spectral* simulation shows a stronger downward motion than the *coupled* simulation.

This stronger downward motion (w^*) is associated with the stronger GW acceleration in the *spectral* simulation, as shown in figure 6.14, and can be expressed by the following equation (*McIntyre* (1989) and *Haynes et al.* (1991)):

$$w^*(z_0) = -\frac{1}{\rho_s(z_0) a \cos\phi} \frac{\partial}{\partial \phi} \left[\frac{\cos\phi}{f} \int_{z_0}^{z_T} \rho_s(z) X(z) dz \right], \tag{6.1}$$

where $w^*(z_0)$ is the vertical motion due to GW parameterization at a height z_0, ϕ is the latitude, ρ_s is the standard density, f is the Coriolis parameter, a is the radius of the

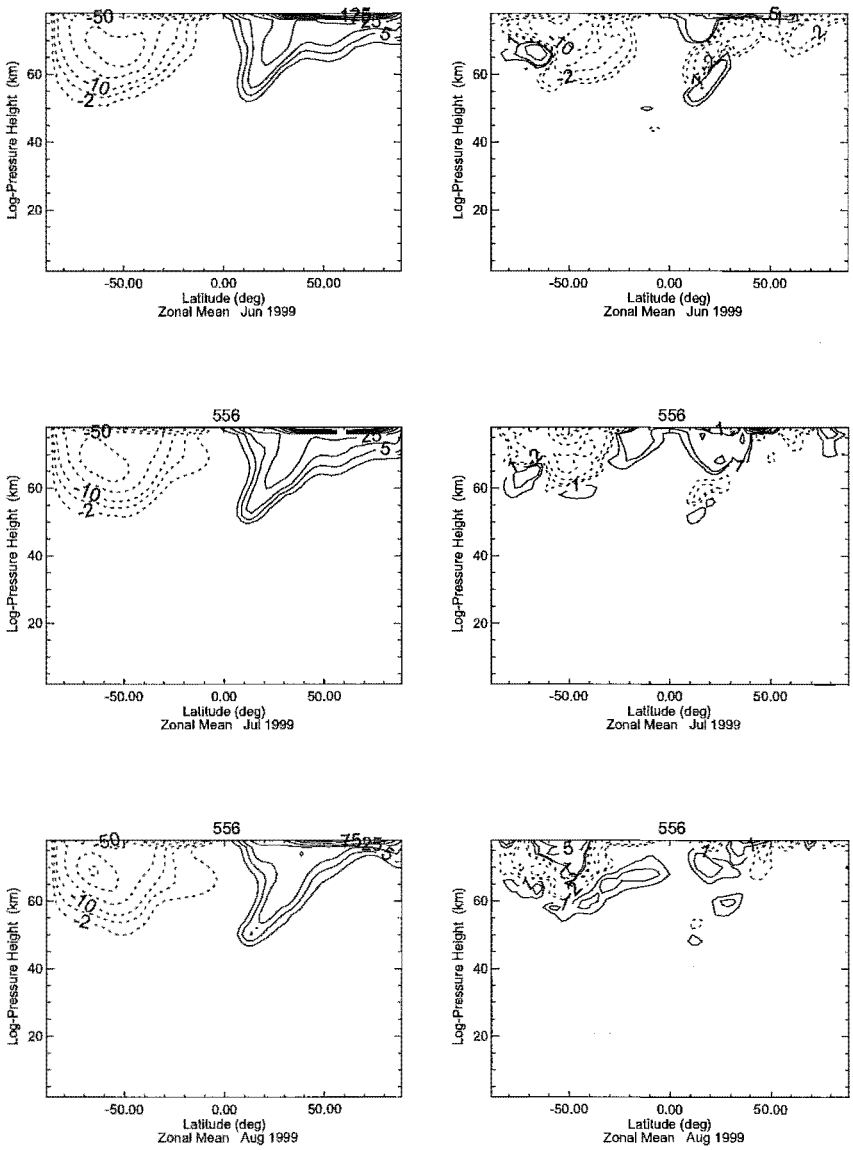

Figure 6.14: The plots in the left are the monthly mean GW zonal acceleration for the months of June, July and August, averaged over 6 years for *spectral* plotted in a logarithmic scale. Contour intervals are: −150, −125, −100, −75, −50, −25, −10, −5, −2, −1, 1, 2, 5, 10, 25, 50, 75, 100, 125, 150 m/s/day The right hand side plots are the difference in GW zonal acceleration for the months of June, July and August, between *spectral* and *coupled* simulations averaged over 6 years. Contour intervals are : −30, −25, −20, −15, −10, −5, −2, −1, 1, 2, 5, 10, 15, 20, 25, 30 m/s/day. The plots from top to bottom are for the months of June, July and August.

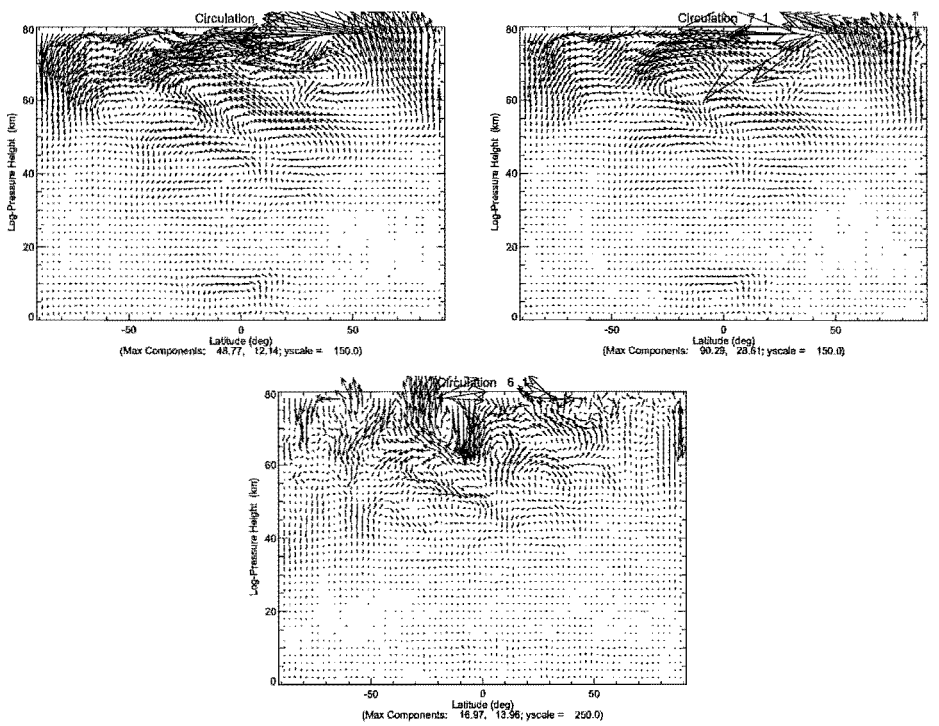

Figure 6.15: Residual mean circulation for the month of June in the *spectral* (top left) and *coupled* (top right) simulations and the difference between them (bottom) for the same month. The vertical winds for the first two plots have been scaled by 150.0 and the last plot has been scaled by 250.0. Maximum components appear in the figure legend.

earth and X is the body force per unit mass due to parameterization and other numerically resolved tendencies. Hence, the stronger GW acceleration in the *spectral* simulation produces a stronger w^* than the *coupled* simulation.

The effect of stronger residual mean vertical motion in the southern hemisphere winter polar mesosphere of the *spectral* simulation compared to the *coupled* simulation is reflected in the adiabatic heating of the same region.

The adiabatic heating can be calculated from the thermal balance equation as explained in Chapter 2:

$$\frac{DT}{Dt} = Q, \tag{6.2}$$

where $\frac{D}{Dt} \equiv \frac{\partial}{\partial t} + u\frac{\partial}{\partial x} + v\frac{\partial}{\partial y} + w\frac{\partial}{\partial z}$, T is the temperature in Kelvin, Q is the diabatic heating term, which in the middle atmosphere is net radiative heating rate per unit mass $Q \equiv (J/c_p)e^{\kappa z/H}$ (*Andrews et al.*, 1987) and the term $w\frac{\partial T}{\partial z}$ is the vertical component of the adiabatic heating rate.

This equation has to be solved to calculate the adiabatic heating rate, which requires both short wave and long wave radiation data to calculate the terms of the equation. In the present work, these data have not been directly accessed from the model. Instead, the model diagnostics have been re-gridded to accommodate input the data from MADPO (*Lawrence*, 1997a), an external module, in order to calculate components of adiabatic heating rate.

The vertical component of the adiabatic heating rate for the *spectral* simulation for the months of June, July, August and September are shown in figure 6.16. The difference in adiabatic heating rate between the *spectral* and *coupled* simulations are shown in figure 6.17.

If the horizontal and meridional component of adiabatic heating is considered negligible, the terms in the equation 5.3 can be rewritten as,

$$\frac{\partial T}{\partial t} = Q - w\frac{\partial T}{\partial z} \tag{6.3}$$

Hence, it can be easily identified from equation 6.3 that heating is associated with negative values of the vertical component of adiabatic heating, while cooling is associated with positive values of the same field.

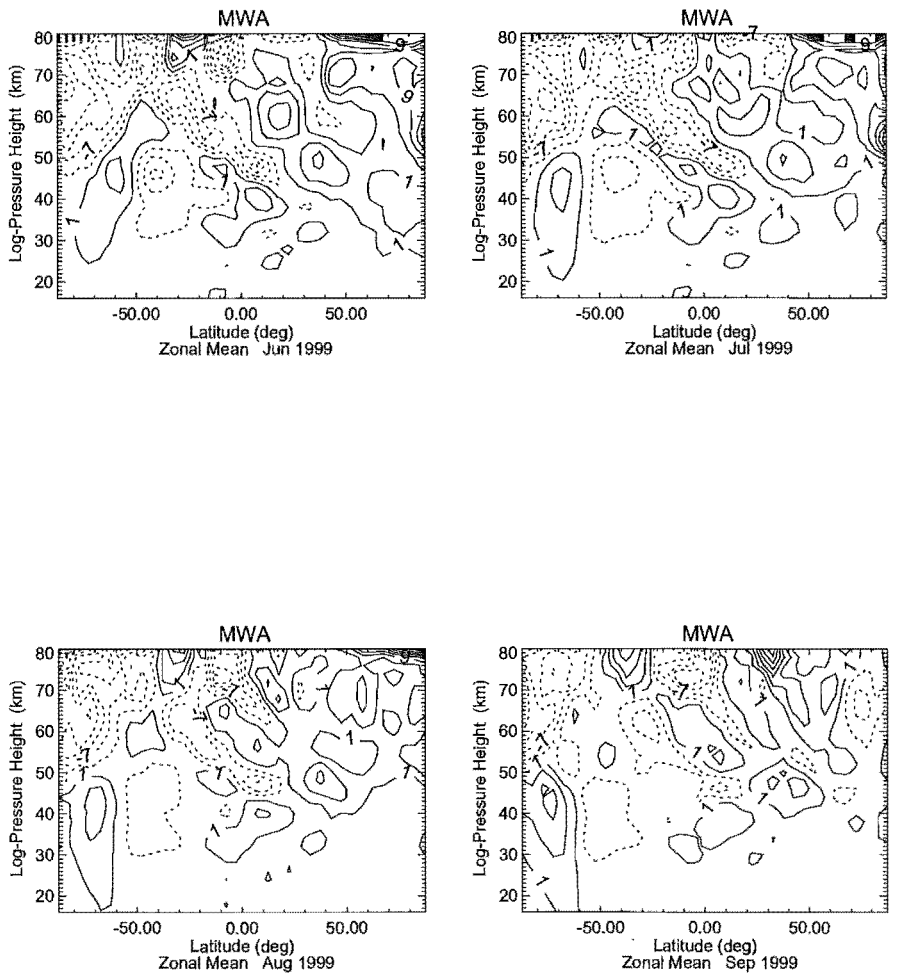

Figure 6.16: Adiabatic heating in *spectral* for the months of June (top left), July (top right), August (bottom left) and September (bottom right). Contour interval is 4^0C/day.

Figure 6.17 shows that the southern hemisphere middle atmosphere in the *spectral* simulation is receiving a considerably larger amount of adiabatic heating than that of the *coupled* simulation.

The stronger vertical advection of temperature in the middle atmosphere of the *spectral* simulation throughout its southern hemisphere winter causes a gradual increase in the polar temperature which becomes evident in the spring, as shown in figure 6.18. The increase in temperature in the southern hemisphere middle atmosphere gradually progresses down from the mesosphere to the stratosphere in the *spectral* simulation (*Swinbank et al.*, 1998). This increase in temperature weakens the polar night jet (via the thermal balance as explained in *Appendix B*) in the *spectral* simulation much earlier than the *coupled* sim-

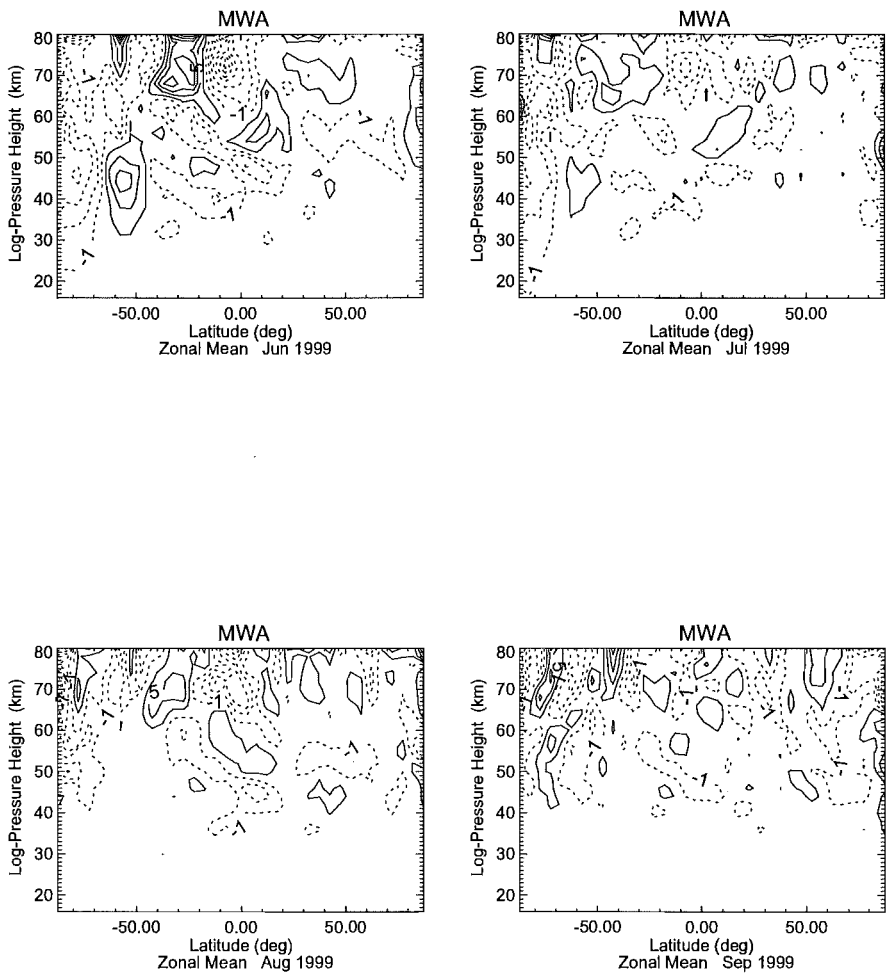

Figure 6.17: Difference between *spectral* and *coupled* in adiabatic heating for the months of June (top left), July (top right), August (bottom left) and September (bottom right). Contour interval is 3^0C/day.

ulation which is displayed in figure 6.19.

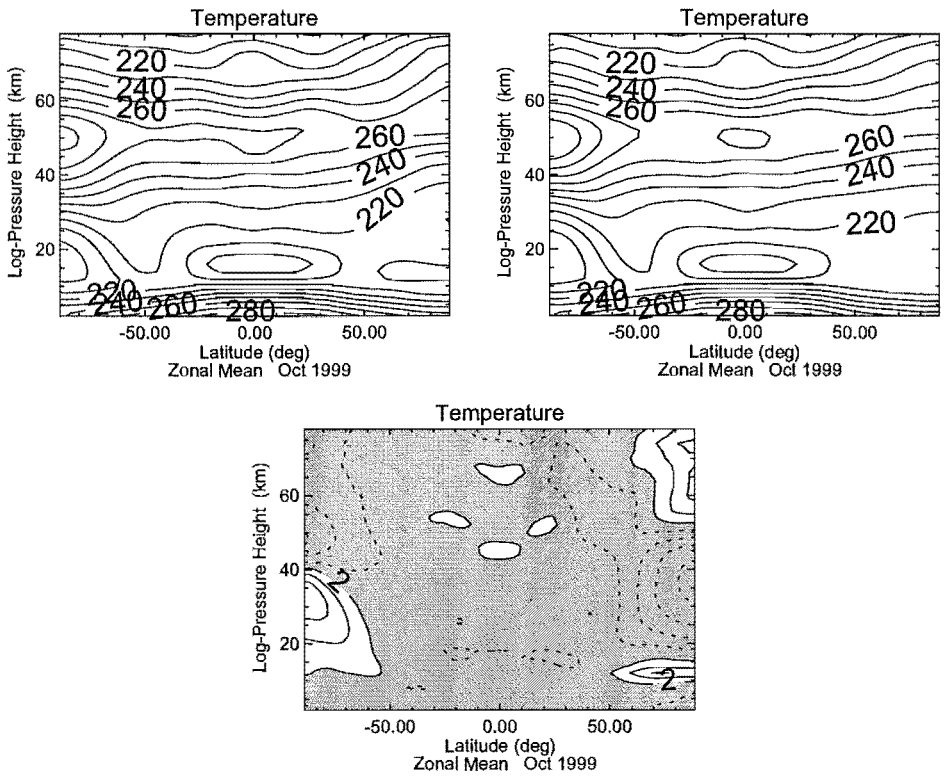

Figure 6.18: Zonal mean zonal temperature for the *spectral* (top left) and *coupled* (top right) runs averaged over six years and difference between them (bottom) for July. Contour interval is 10 K and 3 K for the difference.

It can therefore be summarized from these results that the GW acceleration at the model's uppermost levels in the *spectral* simulation is comparatively stronger than that of the *coupled* simulation. This leads to a deeper vertical advection in the *spectral* simulation between the pole and mid-latitudes in the southern hemisphere. The stronger vertical velocity causes the winter stratosphere in the *spectral* simulation to warm earlier in the spring compared to the *coupled* simulation.

6.4 Summary

The preceding sections discuss the effects of GWs in the middle atmosphere of both the *spectral* and *coupled* simulations, which is the major thrust of the present research. Differences in various dynamical processes are analyzed in view of the differences in GW

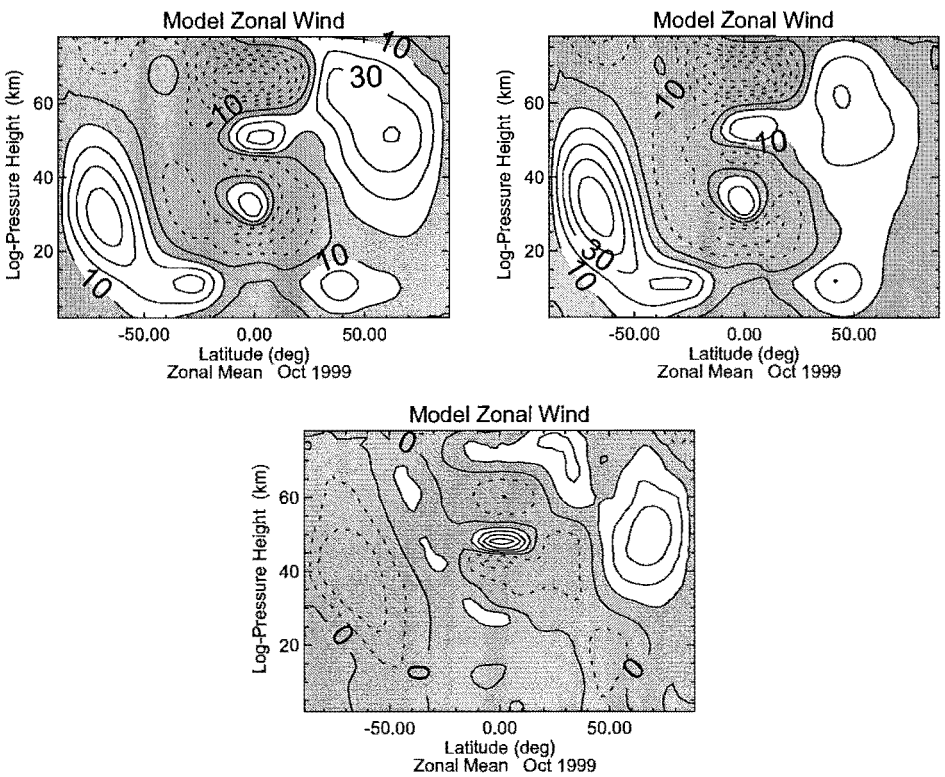

Figure 6.19: Zonal mean zonal wind for the *spectral* (top left), *coupled* (top right) simulation averaged over six years and the difference between them (bottom) for July. Contour interval is 10 m/s and 5 m/s for the difference.

acceleration across the two simulations.

Differences in the northern hemisphere summer have not been very noticeable across the two cases. However, during winter a relatively unstable middle atmosphere is exhibited by the *coupled* simulation compared to the *spectral* simulation. This is caused by the dissipation of GWs at different altitudes, and also at different latitudes in the two simulations. The relatively more unstable middle atmosphere in the *coupled* simulation may also indicate more frequent SSW events.

The southern hemisphere summer and winter have not shown much difference between each other in the context of the different schemes. However, earlier progress towards spring with the change in temperature gradient and corresponding change in the wind shear in the *spectral* simulation compared to the *coupled* simulation has been attributed to the difference in GW acceleration of the two schemes.

The next chapter focuses on high frequency data from an arbitrary year (1991 – 1992) northern hemisphere winter. This study can assist in understanding the difference in the northern hemisphere winter middle atmosphere circulation between the *spectral* and *coupled* simulations induced by the different GW parameterization schemes.

Chapter 7

Case Study of the Northern Hemisphere Winter Middle Atmosphere

7.1 Introduction

In this chapter a case study of the northern hemisphere winter middle atmosphere from an arbitrary year 1992 – 1993 has been studied using both the *spectral* and *coupled* parameterization schemes. It has been noted in Chapter 6 that, due to the difference in GW acceleration between the two simulations, the winter middle atmosphere in *coupled* simulation is more unstable than that of the *spectral* simulation.

This chapter looks at the events in the northern hemisphere winter middle atmosphere in both the simulations that may potentially cause the disturbances, such as SSW. The dynamical features that can play an important role during the SSW events, such as the behaviour of transient planetary waves and equatorial oscillations (as already explained in Chapter 2) are studied in detail.

7.2 Monthly mean time series of zonal mean zonal wind

The frequency of the occurrence of SSW events in the *spectral* and *coupled* simulations can be seen by studying the monthly mean time series of zonal mean wind. Time-series of the vertical structure of monthly mean zonal mean wind for both simulations at 63.75° N are expressed in figure 7.1. It is evident that zonal mean westerly wind in the *spectral* simulation is stronger and more prominent than that in the *coupled*, which is consistent over all 6 years of the simulation.

This evidence supports the argument that stronger GW acceleration in the *spectral* simulation in the mesosphere has indirectly reduced the SSW events resulting in a stronger westerly wind jet structure during northern hemisphere winter (*Lawrence*, 1997a). This also applies to the northern hemisphere winter of the *coupled* simulation, where weaker

gravity wave acceleration in the northern hemisphere winter mesosphere has produced a stronger planetary wave activity. This has increased the frequency of the SSW events and has eventually rendered the westerly jets weaker than those observed in the *spectral* simulation. It has also made the middle atmosphere of the *coupled* simulation more unstable than the *spectral* simulation.

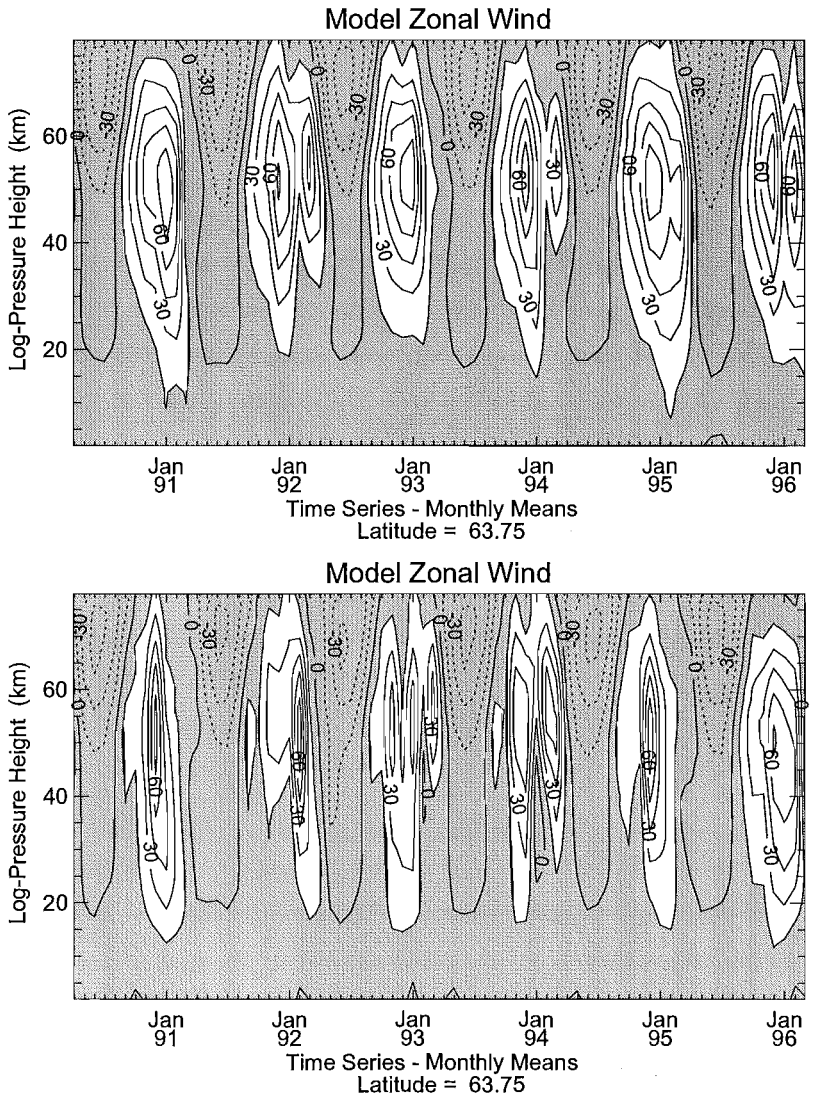

Figure 7.1: Time-series of the vertical structure of monthly mean zonal mean wind at 63.75^0 N for *spectral* (top) and *coupled* (bottom). Shaded regions represent easterly wind jets (negative values). Contour interval is 15 m/s.

To analyze SSW events in both the *spectral* and *coupled* simulations, daily data for a single year, 1992 – 1993, are studied. It should be mentioned here that 1992 – 1993 is a notional year associated with the UM's simulation and does not correspond to the actual

calendar year. Another noteworthy point is that daily data for all six years could not be stored due to the lack of computer disk space. However, it is evident from figure 7.1 that weaker and less prominent zonal mean westerly wind feature of *coupled* simulation is repeated for all years. It must also be mentioned in this context that there is no one-to-one comparison between the two simulations for any given year.

7.2.1 SSW events from daily data

The SSW events in 1992 for both *spectral* and *coupled* simulations are shown in figures 7.2 and 7.3. Output of the model diagnostics, zonal mean wind and zonal mean temperature, have been collected every six hours and averaged over a day.

Figure 7.2 shows the time-series of the vertical structure of temperature at 83.75^0 N and that of the zonal mean wind at 68.75^0 N for the *spectral* simulation. A significant warming of stratospheric temperature during January, which also changes the westerly jets at that altitude to easterly, is displayed in figure 7.2. It should also be noted that the temperature and the wind are both restored to their typical winter values after the event.

Figure 7.3 shows the time-series of the vertical structure of temperature at 83.75^0 N and that of the zonal mean wind at 68.75^0 N for the *coupled* simulation. There are three significant warming events - one in December and the other two in February. The warming in December does not show a reversal of wind at 10 hPa pressure level (32 km) however, there is a change in the shear of westerly wind above that. The second event shows a reversal of the wind shear above 32 km during the warming period, while the warming during the end of February shows a full reversal of the phase of westerly zonal wind to easterly below 32 km.

It is evident that the *spectral* simulation shows only one 'major' warming (see section 2.5.2) in the month of January, figure 7.3. The *coupled* simulation shows three warmings, one in December and the others in February. The first two warmings can be termed 'minor', while the last one is a 'major' warming which is associated with the reversal of zonal mean zonal wind at 32 km (figure7.2).

Although the occurrence of the SSW events is displayed in the time-series plots of daily zonal mean zonal wind and zonal mean temperature, they do not reveal the synoptic structure of the vortex breakdown and restoration. To obtain a deeper insight into the

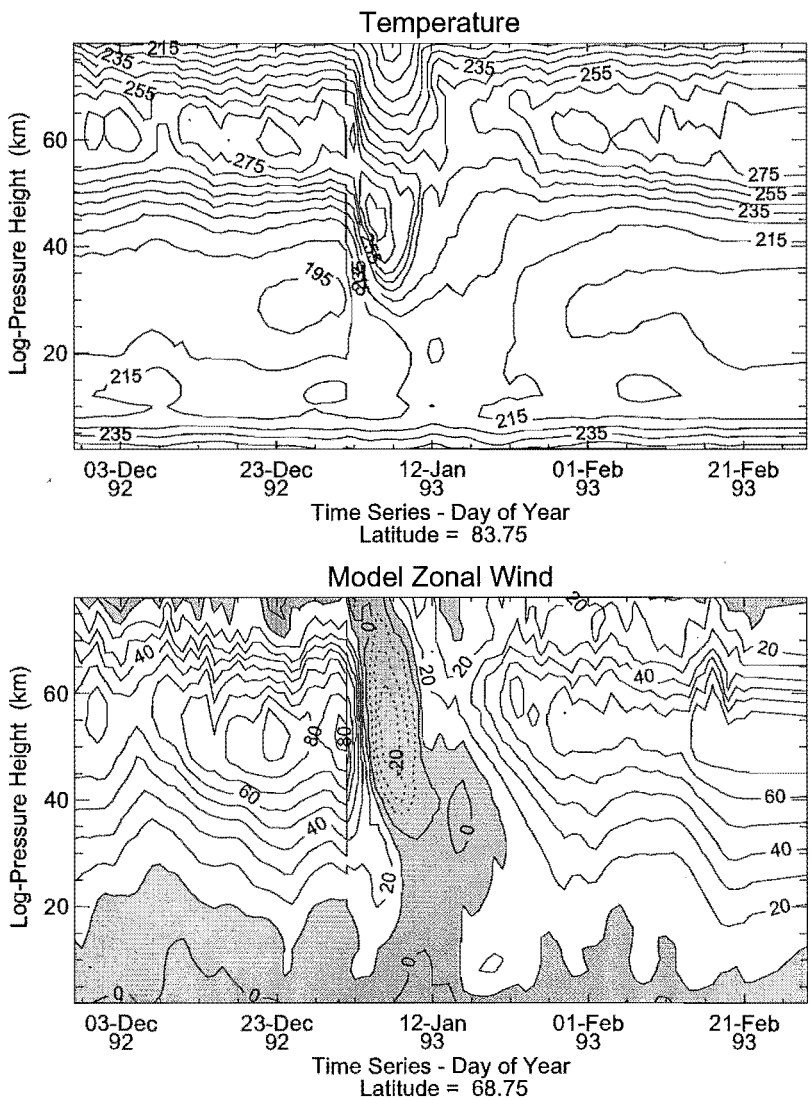

Figure 7.2: Time-series of the vertical structure of temperature at 83.75^0 N (top) and zonal wind at 68.75^0 N (bottom) for *spectral* simulation. Note the change in the change in zonal wind shear during the warming of temparture in January. Contour intervals are 5 K for temperature and 10 m/s for the zonal wind.

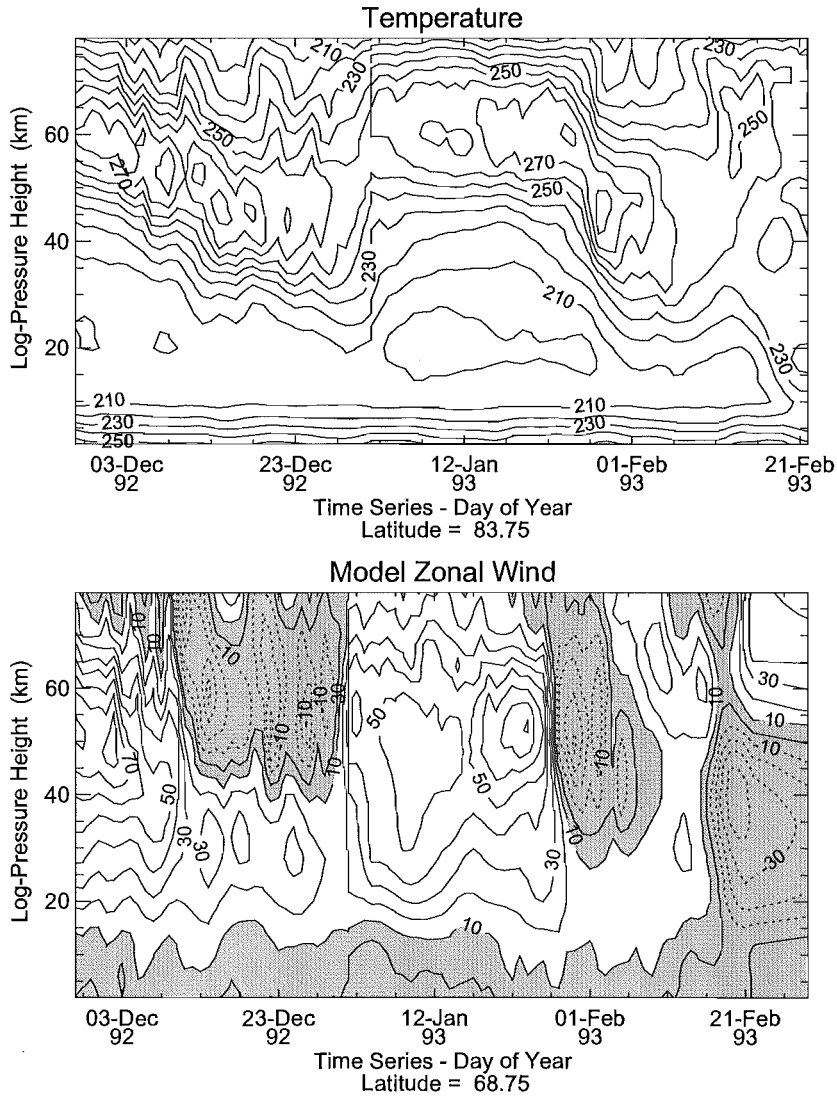

Figure 7.3: Time-series of the vertical structure of temperature at 83.75^0 N (top) and zonal wind at 68.75^0 N (bottom) for *coupled* simulation. Note the change in zonal wind shear during the warming in the end of February. Contour intervals are 5 K for temperature and 10 m/s.

dynamics of SSW events, isentropic maps of Ertel's potential vorticity (*Andrews et al.*, 1987) and geopotential height fields need to be studied. Ertel's potential vorticity and potential temperature fields represent quasi-Lagrangian tracers over periods of a few days, and both are conserved by air parcels in an adiabatic frictionless flow (*Andrews et al.*, 1987).

In the following sections, synoptic maps of isentropic potential vorticity, geopotential height and temperature fields for the *spectral* and *coupled* simulations are studied in detail to identify polar vortex breakdown during SSW events.

7.3 SSW events seen in synoptic plots of temperature and geopotential fields

7.3.1 The spectral simulation

It may be recalled that figure 7.2 shows a SSW event in the time-series of zonal mean wind and zonal mean temperature around day 9 to day 18 in January 1993 in the *spectral* simulation. Isentropic potential vorticity maps at the 850 K isentrope or approximately 10 hPa, shown in figure 7.4, are used to study this event.

It is observed in figure 7.4 that the high potential vorticity has moved away from the pole and has become elongated on day 8. On day 11 it has split into two parts and has started an eastward rotation. Further propagation of the vortex towards the east can be observed on day 12. By the end of the warming event on day 17, the vortex is seen to have moved further eastward and exhibits a reduction in strength.

The change in atmospheric circulation during the same period is also reflected in the geopotential height at the 10 hPa level (figure 7.5). The geopotential height fields are calculated using the MADPO module (*Lawrence*, 1997a) based on temperature and geopotential height fields at 10 hPa. The results are presented for days 8, 11, 12 and 17 of January 1993.

Day 8 of figure 7.5 shows the formation of a small region of high pressure along the eastern side of the low pressure region. The high pressure starts moving longitudinally and pushes the low pressure region away from the pole by day 11. The high pressure region has further moved longitudinally on day 12. On day 17 the shape of the low pressure

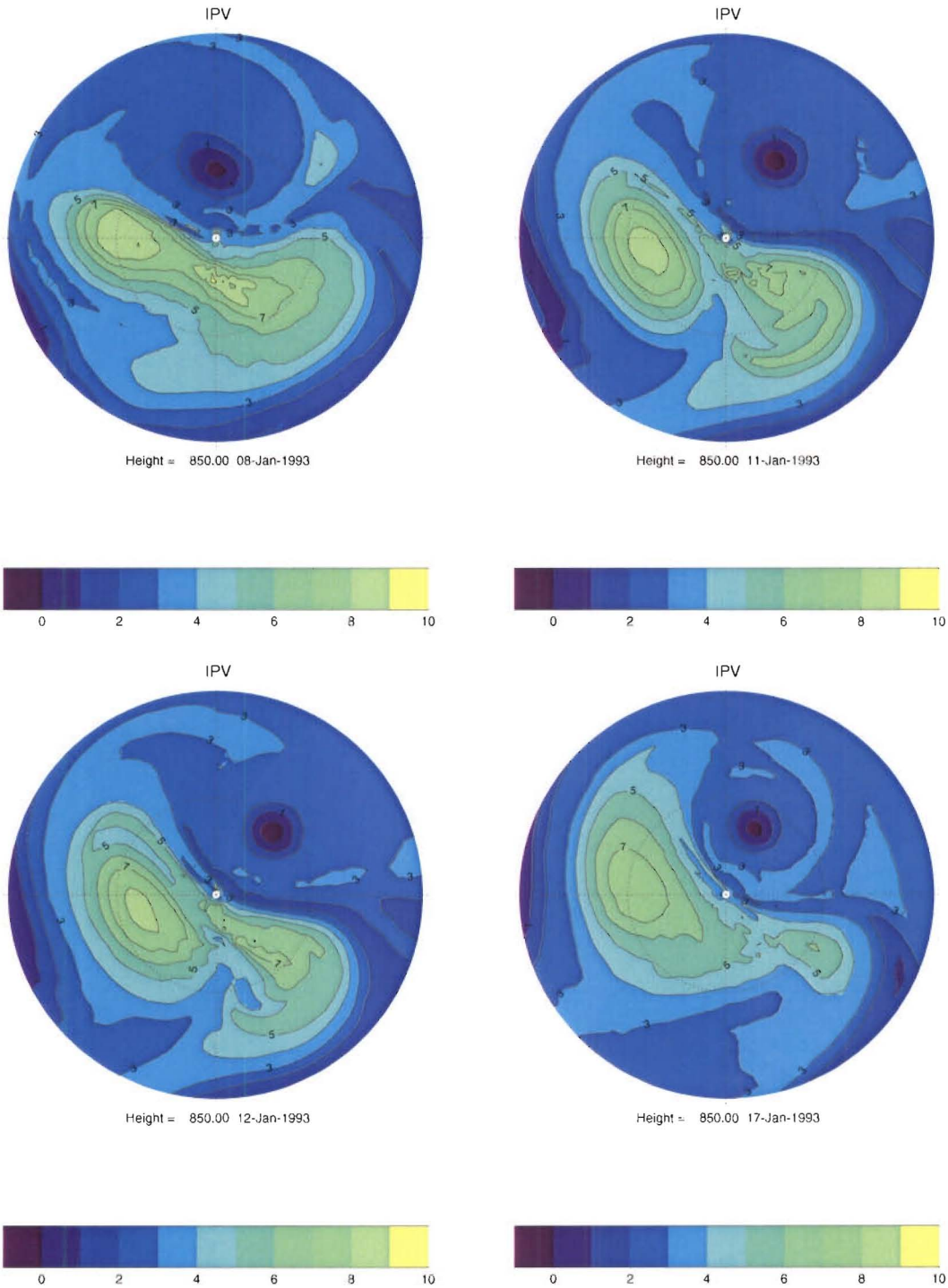

Figure 7.4: Polar-stereographic map of potential vorticity of *spectral* (10^{-4} $Km^2/s/kg$) on 850 K isentrope. The circles extend up to 60^0 N and contour interval is 1 $Km^2/s/kg$. The plots are (from left to right) for days 8 (top left), 11 (top right), 12 (bottom left) and 17 (bottom right) of January 1993.

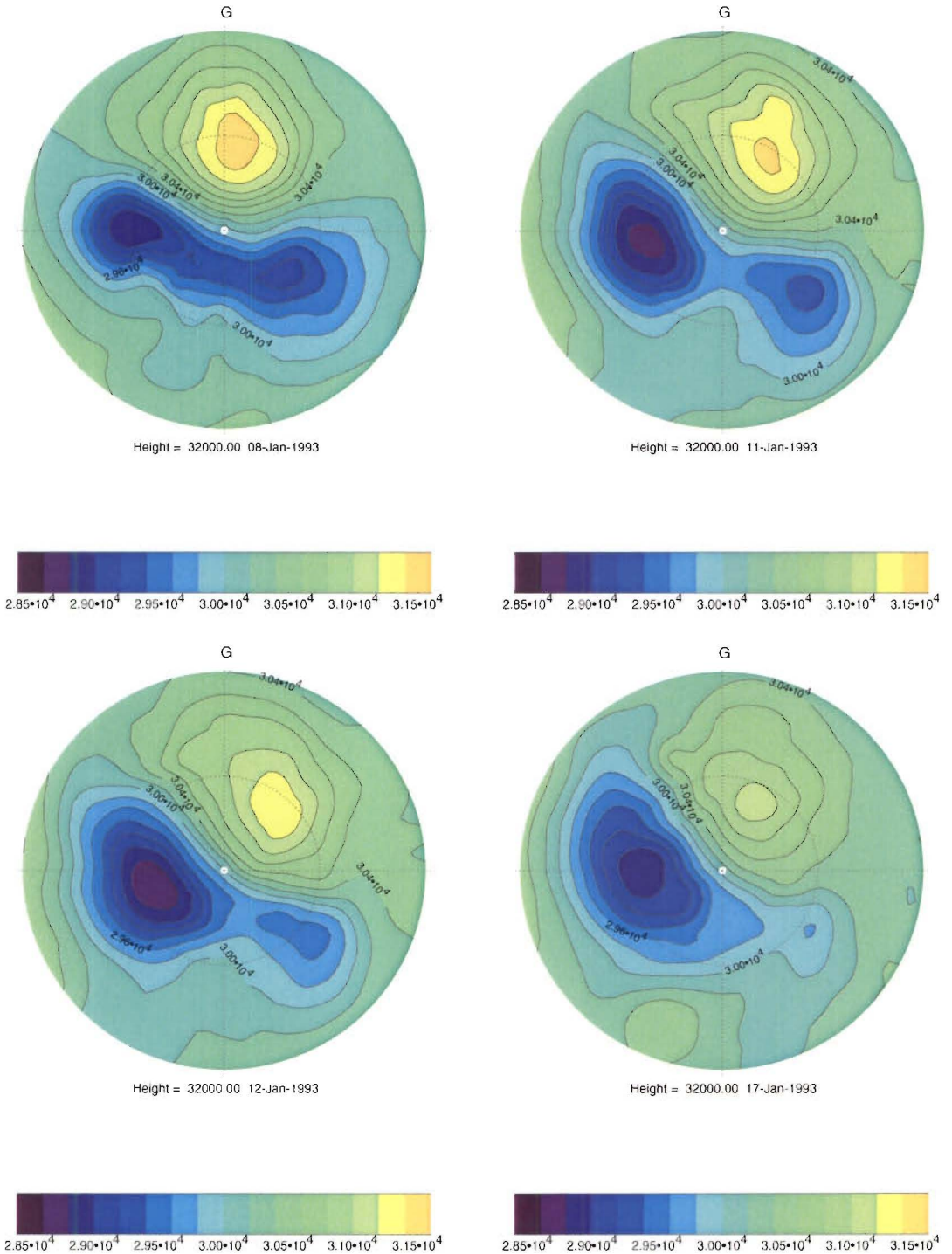

Figure 7.5: Polar-stereographic map of the simulated *spectral* geopotential height at 32 km. The circles extend up to 60^0 N and contour interval is 200 m. The plots are for days 8 (top left), 11 (top right), 12 (bottom left) and 17 (bottom right) of January 1993.

region has elongated and the model simulates a secondary anticyclone [1]. However, the geopotential height fails to reproduce departure of the low-pressure region from the pole during the warming event. A similar feature has also been identified by *Swinbank et al.* (1998) using the UM during early January.

In addition to the isentropic potential vorticity and the geopotential height, SSW events can also be diagnosed using synoptic maps of temperature. The synoptic maps of temperature at the 10 hPa level for the present SSW event are presented in figure 7.6 for days 8, 11, 12 and 17 of January 1993.

It can be observed in figure 7.6 that a high temperature region has pushed the low temperature region away from the pole on day 8. On days 11 and 12, the low temperature region has moved further away from the polar latitudes. On day 17 the low temperature region shows a warming effect and the high temperature region also shows a considerable reduction in its size.

7.3.2 The coupled simulation

The *coupled* simulation also shows SSW events; however, the occurrence of the SSW in the *coupled* simulation is more frequent than that of the *spectral* simulation. The first warming is observed to start in mid-December and extends to almost the end of December, as opposed to the early January SSW event in the *spectral* simulation. However, this warming has not reversed the westerly wind shear below 10 hPa. In the second event, observed in late January, the temperature in the polar region does not revert to typical polar winter temperature values. This is followed by a 'major' warming event in late February which reverses the polar night jet shear as in figure 7.3.

The first SSW event of the *coupled* simulation is studied in detail using synoptic maps of isentropic potential vorticity, geopotential height and temperature fields in this section.

The potential vorticity fields at the 850 K isentrope for the days 24, 25, 26 and 28 of December 1992 are shown in figure 7.7. On day 24 of December, the high vorticity region of the pole is visibly elongated and rotating eastward. The high vorticity region elongates even more and starts rotating on day 25. A further elongation and rotation of the vortex

[1] This secondary anticyclone is often advected around the polar vortex to merge with the Aleutian High (*O'Neill et al.*, 1994)

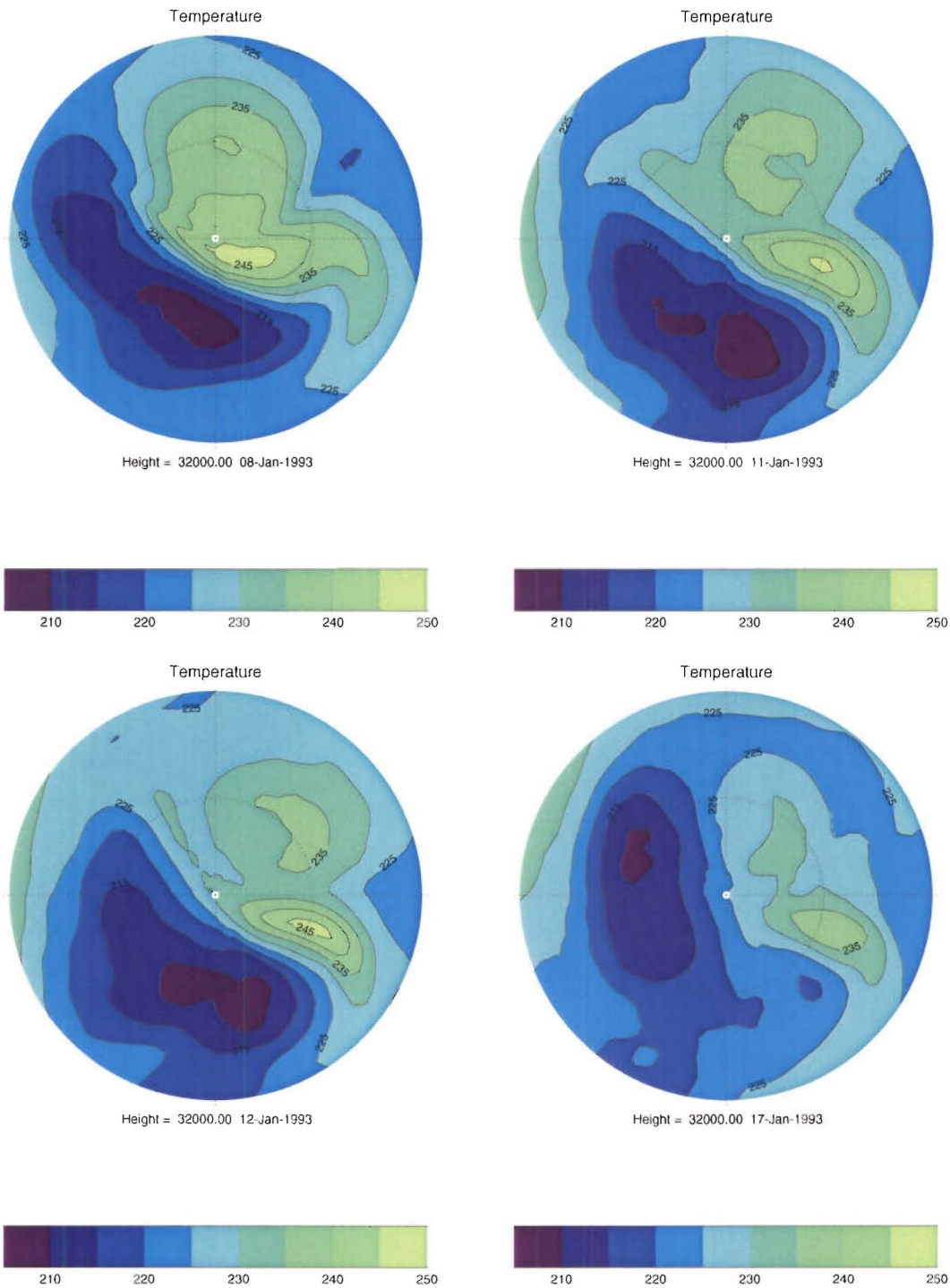

Figure 7.6: Polar-stereographic map of the simulated *spectral* temperature at 32 km. The circles extend up to 60^0 N and contour interval is 5 K. The plots are for days 8 (top left), 11 (top right), 12 (bottom left) and 17 (bottom right) of January 1993.

towards the east is noticed on day 26. On day 28 the high potential vorticity region is split into two parts and a reduction in its strength is observed.

Synoptic maps of geopotential height at 32 km, for the above-mentioned days, are presented in figure 7.8. An anticyclonic region is observed to have pushed the cyclonic core away from the north pole on day 24. On the following day, the anticyclone has grown stronger and has pushed the cyclonic vortex even further away from the pole. The cyclonic vortex has also elongated in shape. The low pressure cyclonic vortex is split into two parts and the high pressure anticyclone grows stronger on day 26. Finally, on day 28 it is observed that the anticyclone has pushed the vortex towards the east from its initial position and it stays away from the pole.

Synoptic maps of temperature at 32 km for the days 24, 25, 26 and 28 of December 1992 are also studied in figure 7.9. On day 24 the low temperature zone is pushed away from the pole by a high temperature zone. An increase in temperature in the high temperature zone is displayed on day 25. On day 26 the low temperature core starts rotating towards the west. Finally, day 28 shows a considerable warming at the pole. The high temperature region is seen to be covering most of the polar region and the low temperature zone is pushed away from the pole.

Studies of the SSW events from the two simulations have revealed that the *coupled* simulation shows more frequent SSW events compared to the *spectral* simulation. The difference in GW acceleration in the two simulations is the main reason behind this. The synoptic behaviour of the formation of the event and subsequent breakdown of the polar vortex has been noticed in both simulations. It can be noted here that GW acceleration has not only changed the middle atmosphere circulation in a climatological time frame, but it has also affected the circulation at daily time scales.

The transient planetary waves have been identified in *Andrews et al.* (1987) as playing an important role in the SSW events in the northern hemisphere winter. In the next section, behaviour of these waves during the SSW events is studied.

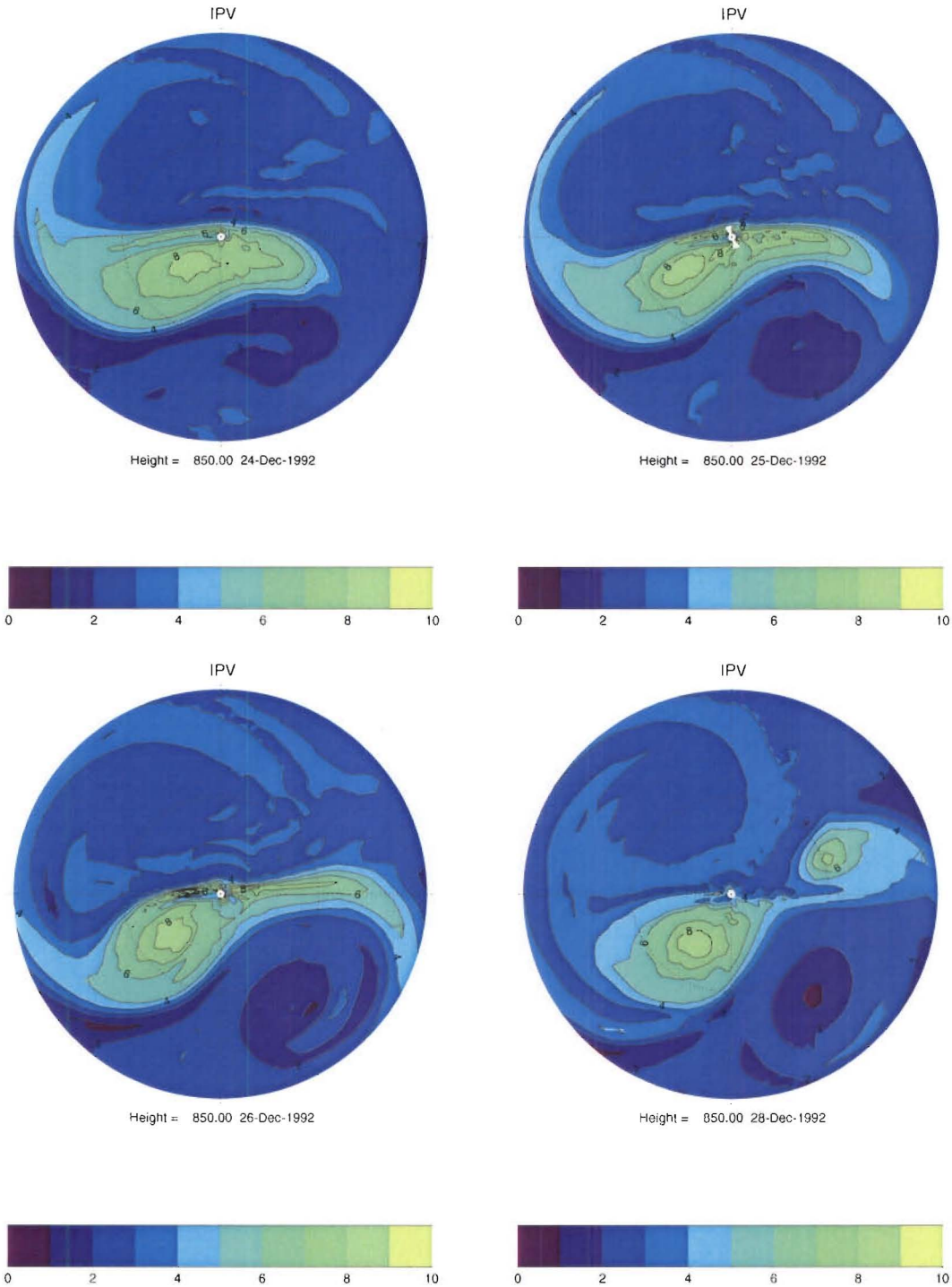

Figure 7.7: Polar-stereographic map of potential vorticity of *coupled* (10^{-4} $Km^2/s/kg$) on 850 K isentrope. The circles extend up to 60^0 N and contour interval is 1 $Km^2/s/kg$. The plots are (from left to right) for days 24 (top left), 25 (top right), 26 (bottom left) and 28 (bottom right) of December 1992.

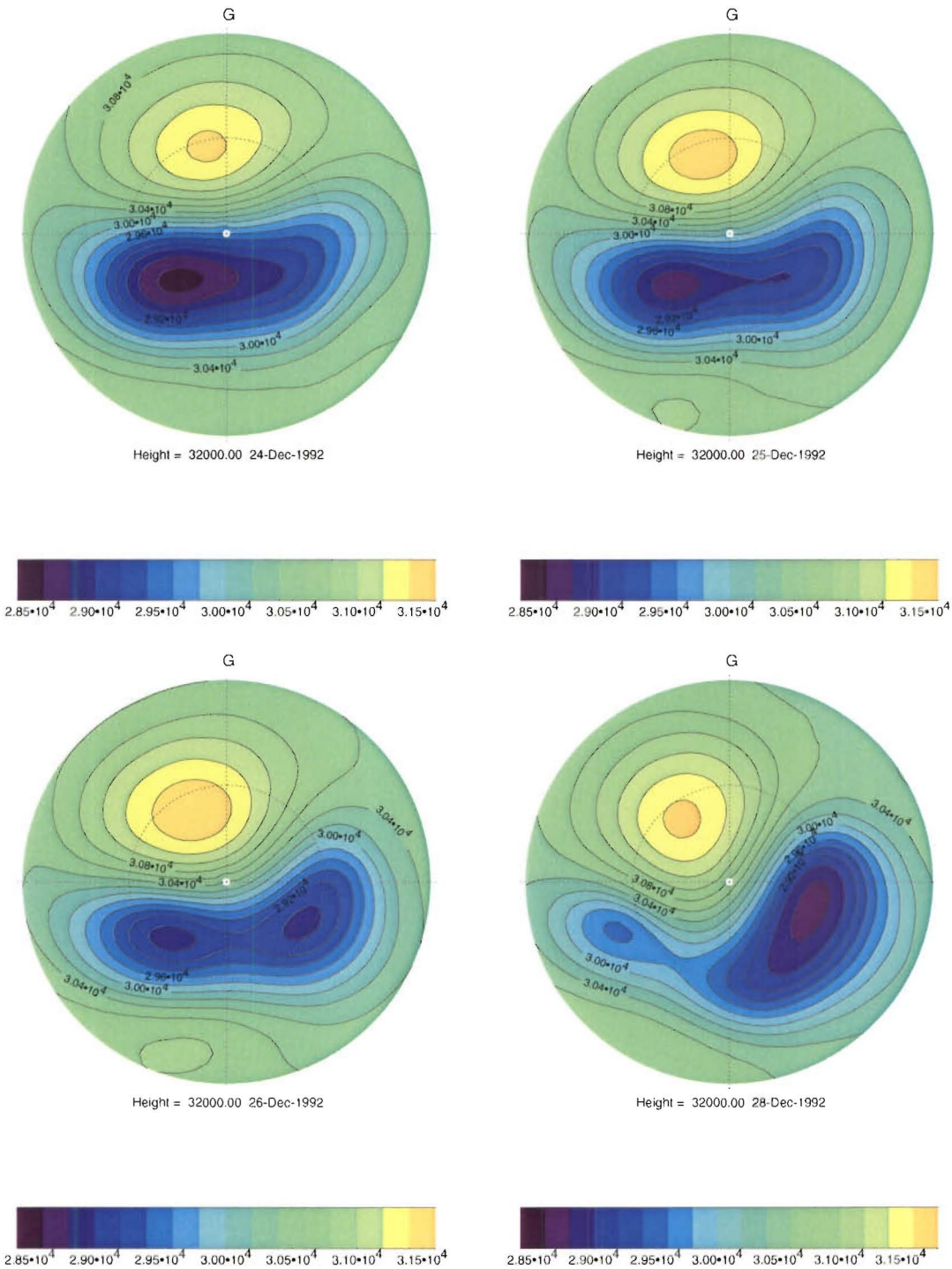

Figure 7.8: Polar-stereo-graphic map of the simulated *coupled* geopotential height at 32 km. The circles extend up to 60^0 N and contour interval is 200 m. The plots (from left to right) are for days 24 (top left), 25 (top right), 26 (bottom left) and 28 (bottom right) of December 1992.

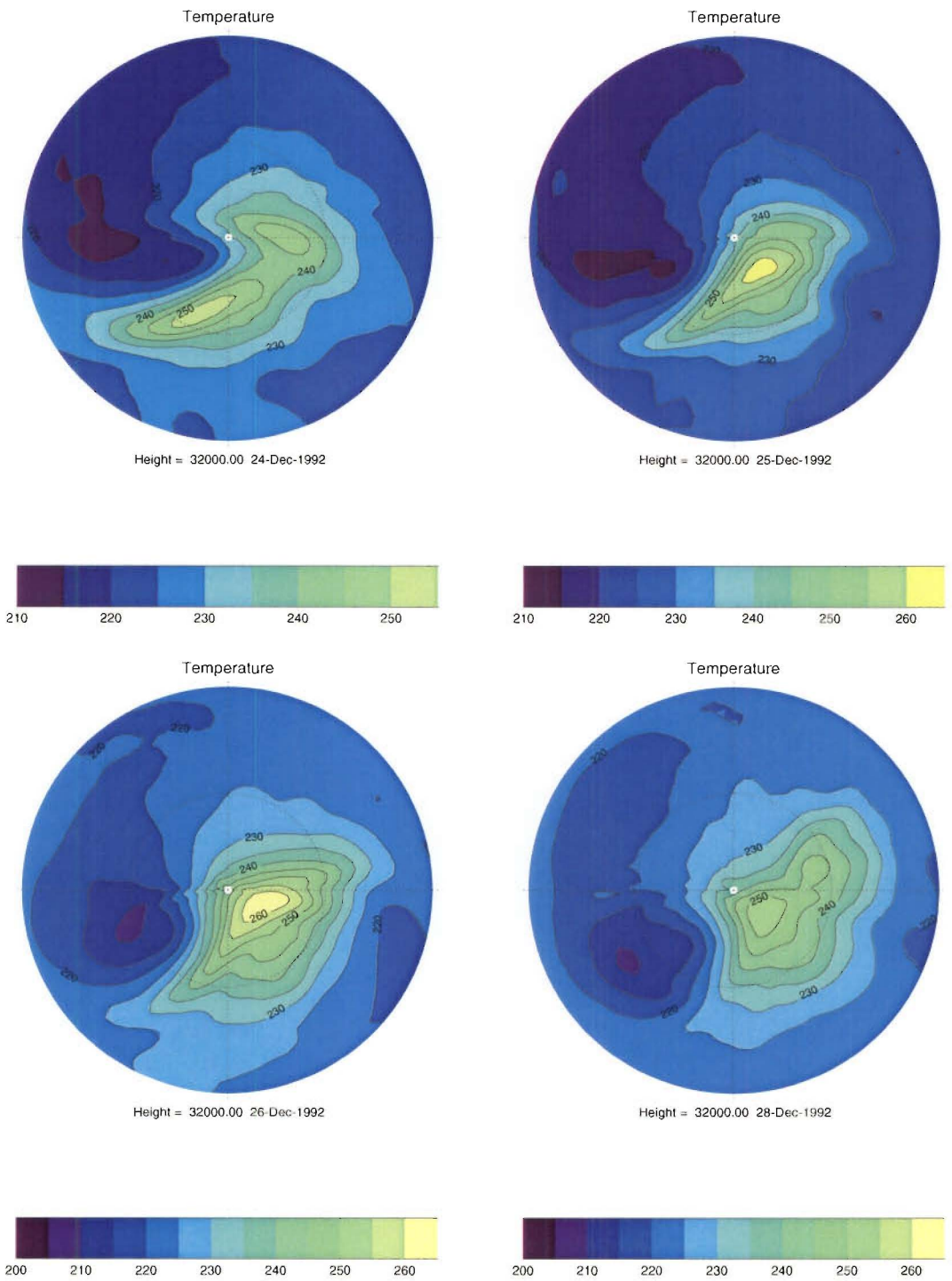

Figure 7.9: Polar-stereo-graphic map of the simulated *coupled* temperature at 32 km. The circles extend up to 60^0 N and contour interval is 5 K. Days 24 (top left), 25 (top right), 26 (bottom left) and 28 (bottom right) of December 1992 are presented (from left to right).

7.4 Behaviour of transient planetary waves during SSW events

It has been reported by *Andrews et al.* (1987) that a change in the behaviour of transient planetary waves can be observed prior to and after a SSW event, as explained in Chapter 2. The waves propagate and converge at the northern polar lower stratosphere just before the warming. Divergence of the waves can be observed in the same region immediately after the warming.

These features can be identified by studying the divergence of Eliassen-Palm flux (EP-flux, described in *Appendix C*). In the following figures, positive values represent divergence and negative values represent convergence of EP-flux.

Figures 7.10 and 7.11 show values of EP-flux divergence during the SSW events in the *spectral* and *coupled* simulations. The days in figures 7.10 and 7.11 are selected because they demonstrate the change in the behaviour of transient planetary waves before and after the SSW events. It should be noted that the y-axis (height) of the figures range from ground to 32 km in the atmosphere.

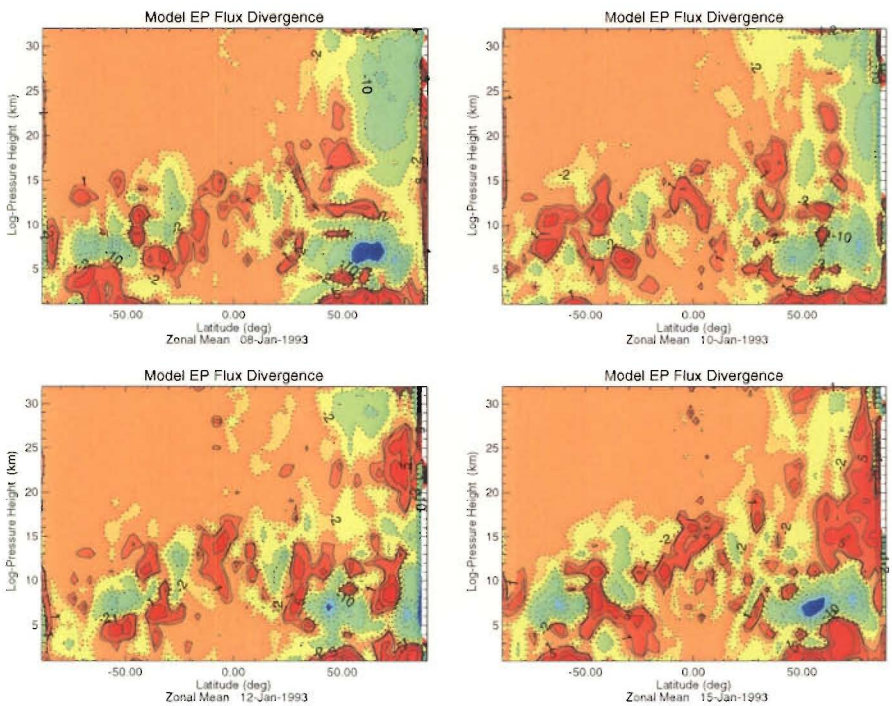

Figure 7.10: EP-flux divergence for *spectral*. Days 8 (top left), 10 (top right), 12 (bottom left) and 15 (bottom right) in January 1993 are shown here. The contours are in logarithmic scale with contour intervals going from −60, −50, −40, −30, −20, −10, −5, −2, −1, 1, 2, 5, 10, 20, 30, 40, 50 m/s/day.

Figure 7.10 shows EP-flux divergence for days 8, 10, 12 and 15 of January 1993 for the

spectral simulation during the first warming. Day 8 shows a significant convergence of the EP-flux from troposphere to the lower stratosphere and this repeats itself on day 10. On day 12 the strength of the convergence of EP-flux in the northern hemisphere lower stratosphere (15 to 25 km) is considerably reduced and a divergence zone is beginning to form. The results of day 15 clearly show a strong divergence zone observed before the warming at the same latitude and height (15 to 25 km).

A similar trend in EP-flux divergence is also displayed in the *coupled* simulation in figure 7.11. The days selected are 18 and 19 of December 1992 and days 1 and 2 of January 1993 from the first SSW event in the *coupled* simulation.

A strong convergence is observed in figure 7.11 on days 18 and 19 in the northern hemisphere polar lower stratosphere (15 to 30 km) before the warming. Immediately after the warming event, on days 2 and 3, a divergence zone is observed to develop at the same latitude in the lower stratosphere (20 to 30 km).

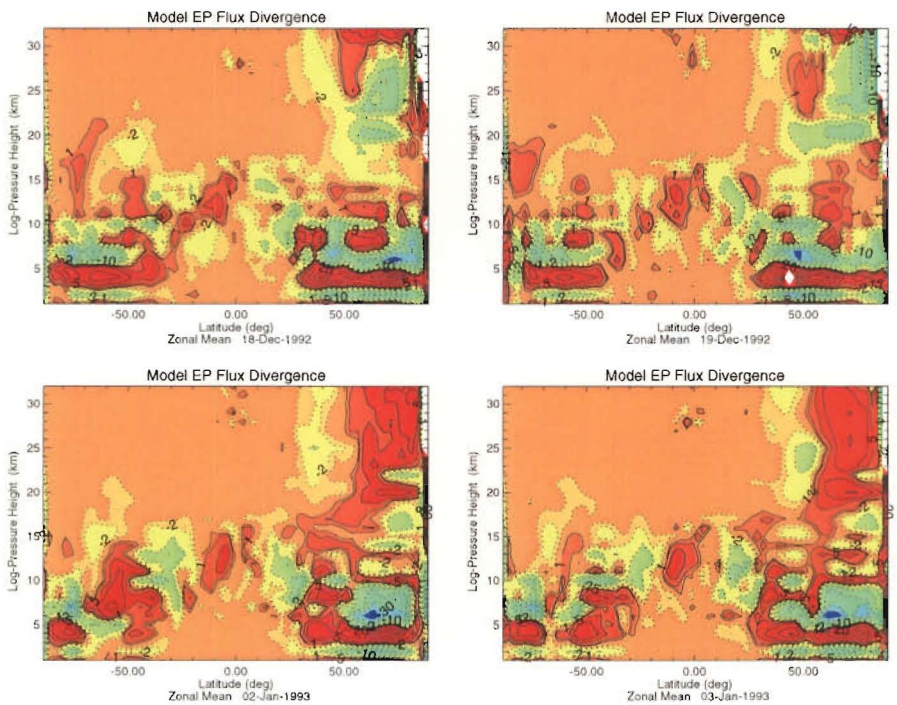

Figure 7.11: EP-flux divergence for *coupled* for the days 18 (top left) and 19 (top right) in December 1992, and days 1 (bottom left) and 2 (bottom right) in January 1993 are shown here. The contours are in logarithmic scale with contour intervals going from −60, −50, −40, −30, −20, −10, −5, −2, −1, 1, 2, 5, 10, 20, 30, 40, 50 m/s/day.

Hence, it is evident from the results that a significant change in the transient wave activity occurs immediately before and after the SSW event, which supports the theory of

Andrews et al. (1987) among others. It can also be deduced that as the frequency of SSW events are more frequent in the *coupled* simulation compared to the *spectral* simulation, the change in the transient wave activity is greater in the *coupled* simulation than the *spectral* simulation. This may be an indirect effect of the difference in GW acceleration in the lower stratosphere between the two simulations.

In addition to transient wave activity, equatorial circulation has also been considered to have a bearing on SSW events (*Dunkerton and Baldwin*, 1991). The equatorial circulations of both the *spectral* and *coupled* simulations are studied in the following section.

7.5 The equatorial oscillations and SSW

Figure 7.12 and figure 7.13 show the time-series of the vertical structure of zonal mean zonal wind for both simulations at 1.25^0 South. As noted in Chapter 6, neither simulation exhibit the presence of QBO or SAO. The difference between these fields for the two simulations is shown in figure 7.12. It is obvious from figure 7.14 that the easterly wind shear in the *coupled* is stronger than in the *spectral* between 25 to 30 km altitude.

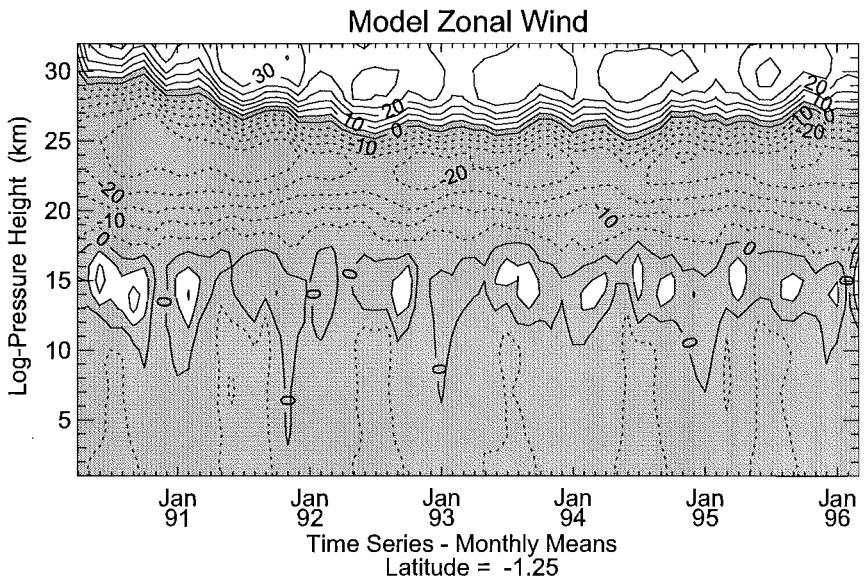

Figure 7.12: Time-series of vertical structure of zonal mean zonal wind at 1.25^0 South in *spectral*. Note the absence of QBO and the descent of westerly shear zone early in the simulation. Contour interval 5 m/s.

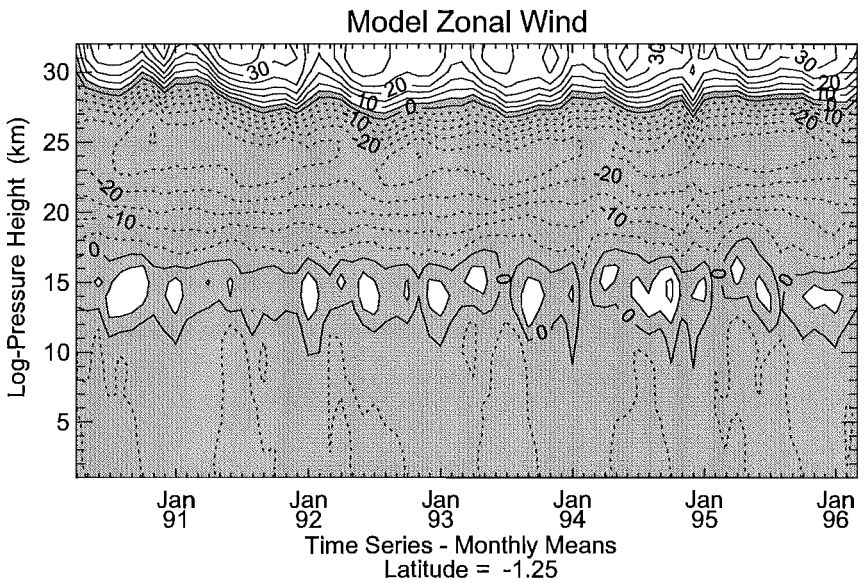

Figure 7.13: Time-series of vertical structure of zonal mean zonal wind at 1.25^0 South in *coupled*. Absence of QBO is noticed.Contour interval 5 m/s.

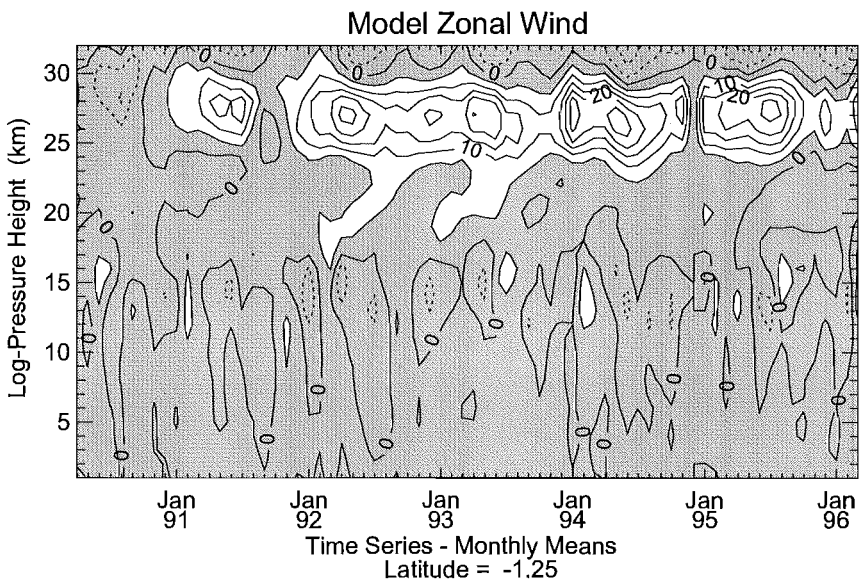

Figure 7.14: Time-series of the difference between the zonal mean zonal wind in *spectral* and *coupled*. Note the difference in zonal wind between $25 - 30$ km. Contour interval 5 m/s.

This difference in the zonal mean zonal wind supports the study by *Dunkerton and Baldwin* (1991). They found that a weaker than normal polar night jet and a warmer than normal polar night temperature could be associated with an easterly phase of QBO at 27 km. Thus the results in this section might provide an additional indication of higher temperature and weaker polar night jet in the *coupled* simulation than in the *spectral* simulation.

However, it should be noted that the simulation of QBO has been deliberately avoided here by not including a large amplitude gravity wave flux, because the effects of QBO might contaminate the analysis of other physical phenomena of the middle atmosphere. Further work with the same GW parameterization schemes needs be performed to simulate QBO and analyze its effect on the middle atmosphere dynamics.

7.6 Summary

The SSW events of both the *spectral* and *coupled* simulations have been studied in detail in this chapter with the aid of daily time-series and synoptic data. It has been revealed that the frequency of the SSW events in the *coupled* simulation is higher than that of the *spectral* simulation. This is explained by the GW acceleration, which is stronger in the mesosphere of the *spectral* simulation compared to the *coupled*.

Due to the dissipation of waves at a comparatively lower altitude in the *coupled* simulation than the *spectral*, a difference in the transient wave activity has also been noted between the two schemes. The transient wave activity is also closely connected to the SSW events, as discussed in Chapter 2. In addition to transient wave activity, differences have also been noted in the equatorial oscillations. Although QBO has not been observed in either of the cases, a difference in wind shear has been observed which may indicate a more unstable winter in the *coupled* simulation than that of the *spectral*.

It can therefore be stated that, in addition to changes in the climatological scales, the GW drag has also induced changes in the daily scale circulation. In addition to the direct effect, such as residual mean circulation, it has indirectly affected the winter middle atmosphere by inducing changes in the equatorial circulation and transient wave activity.

Chapter 8

Summary

In this chapter, a comprehensive summary of all the major contributions of the present work is provided along with discussions on further work.

The main objective of this thesis is to investigate how the simulated climate of the Unified Model (UM), a state-of-the-art General Circulation Model (GCM), responds to more physically realistic gravity wave parameterization, beginning with the addition of a broad spectrum gravity wave scheme then progressing to a scheme which couples orographic and broad spectrum gravity waves. The UM simulates gravity waves with an orographically induced gravity wave scheme that works up to an altitude of 27 km in the model; and above that, it uses a Rayleigh friction scheme.

To achieve the goal, two gravity wave parameterization schemes (in addition to the existing gravity wave scheme in the UM) working on different physical assumptions have been incorporated in the UM to simulate their effects in the model's climatology. The two schemes are: the DSP scheme (based in the premise that gravity waves form a broad spectrum waves) and 'coupled interactive' broad spectrum and orographic scheme (based on the premise that broad spectrum and monochromatic gravity waves interact with each other (*Hines*, 1997a,b). Although, many modelling studies have been performed by incorporating the DSP scheme in GCMs, results from simulations using a 'coupled interactive' scheme in GCMs have not been reported.

Using these two schemes, several key aspects of GW behaviour have been simulated in the UM, which has led to model sensitivity results that have not been previously reported. However, it should be noted that no attempt has been made to asses the superiority of one scheme or the other.

Before incorporating the gravity wave parameterization schemes in the UM, they were tested in a single column test bed. The test bed was developed on the basis of the UM's architecture but with fewer parameter spaces than the original model. The results ob-

tained from the test bed throw light on the evolution and subsequent dissipation of the gravity waves of the two schemes in an ideal atmosphere. The results have been analyzed to determine if they reasonably reproduce the conventional gravity wave breaking phenomena. The differences between propagation of gravity waves within the two schemes has also been analyzed.

8.1 Summary of test bed results

To analyze gravity wave propagation as represented by these physical regimes, six idealized experiments were conducted with the UM's original GWD scheme and the two new schemes in the test bed. The zonal mean winds were changed for each case to represent a typical quasi-biennial profile, a typical mid-latitude summer hemisphere wind profile, and a typical mid-latitude winter hemisphere wind profile. The other atmospheric parameters such as meridional wind, temperature, static stability and humidity were kept constant for all experiments.

The study showed that the orographic GWs in the UM contributed to damping in the tropopshere and the lower stratosphere. While with the UM's original GWD scheme, the damping of zonal wind is extended up to the model's upper most levels.

The next experiments were conducted to analyze the effect of the troposphere on a vertically propagating broad spectrum of gravity waves. The gravity wave spectrum was launched from two different altitudes, corresponding to the model surface level and the tropopause. The results show that when gravity waves are launched from the ground, local wind shear in the troposphere induces a spectral imbalance by filtering some part of the spectrum. Therefore, the forcing produced by gravity waves launched at ground level is different from that produced when the waves are launched at the tropopause. The broad spectrum waves were also launched in the presence of high mountains; however, the results do not show any change.

In addition to that, effects of broad spectrum wave launched from ground is also studied with and without the combination of orography. It is seen that when orographic waves work parallely with the broad spectrum wave, there is a deposition of stress and resultant drag at both tropopause and lower mesosphere. The amount of drag at the tropopause is equal to that produced by the UM's original GWD, while the drag at the model's top

levels are much stronger than the original GWD scheme. Without orography, the broad spectrum waves produce drag only in the lower mesosphere of the model. The amount produced by the broad spectrum waves alone at the lower mesosphere is equal to that generated by the combination of both broad sectrum and orographic waves.

This scheme was then extended to couple the UM's built-in orographic gravity waves with the broad spectrum waves. The last experiments on the test bed were conducted to analyze the effect of orography on propagation of coupled interactive broad spectrum and monochromatic gravity waves. These waves were launched from the ground in the presence of high and low mountains. Results from these experiments were compared with the UM's original GWD scheme and the broad spectrum gravity waves launched from the ground. It can be summarised from the study that the coupled waves generated drag at the tropapause level similar to the UM's original GWD scheme, however it is weaker than that of the UM's original GWD scheme. The damping due to the coupled waves were far stronger than the original GWD. However, the drag produced by the coupled waves were generated from a lower altitude than the broad spectrum waves. Also, the drag at the model's top most level in the coupled scheme is weaker than that of the broad spectrum scheme at the same levels.

It was also found that the coupled interactive scheme in the summer hemisphere does not induce any significant change in gravity wave zonal acceleration, as compared to the broad spectrum gravity wave scheme.

However, during winter the spectrum of coupled interactive waves starts dissipating at lower altitudes, which leads to the conclusion that the spectrum is predisposed towards instability with the inclusion of orographic gravity waves that are monochromatic in nature. This is equivalent to using a different global mean gravity wave source.

To examine if these features are also reflected in a GCM, the schemes were incorporated in the UM and run for six years each. Results from the two simulations were analyzed and compared to see if the change in their respective gravity wave forcing has any direct, or indirect effect in the global circulation.

8.2 Summary of results from the Unified Model

Simulations with the spectral and coupled gravity wave schemes in middle atmosphere models have been extensively reported, for example, *Manzini and McFarlane* (1998) and *Osprey and Lawrence* (2001). However, the models in both these cases did not have a troposphere, which is the main difference between these reports and the present work. Detailed study of the effects of both spectral and coupled schemes has shown differences in the model's tropospheric circulation arise from differences in GW parameterization.

The tropospheric westerly wind in the winter northern hemisphere is seen to be weaker in the broad spectrum simulation than the coupled interactive simulation. This can be attributed to the acceleration produced by independently propagating orographically induced gravity waves of the UM. A similar phenomenon due to orographic waves has also been reported by *Gregory et al.* (1998) and *Milton and Wilson* (1996).

The difference in gravity wave acceleration in the troposphere between the two schemes also induces changes in the forcing of resolved waves in the northern hemisphere extratropics during winter. A stronger forcing due to resolved waves is identified in the broad spectrum simulation compared to the coupled interactive simulation. This results in a stronger residual mean circulation in the extratropical troposphere of the broad spectrum simulation, which leads to a warming of the tropopause in spectral simulation in comparison to the coupled interactive simulation.

The effects of gravity waves were then studied in the middle atmosphere of the model. The results obtained from the spectral simulation were initially compared with a standard set of UKMO assimilated data. A qualitative comparison of zonal mean wind, meridional wind, vertical wind and temperature fields with the UKMO data shows that the model can resolve the main features of the middle atmosphere dynamics. However, the temperature fields in the winter stratosphere of both simulations have lower values than the UKMO data, which might indicate the necessity for using a stronger global mean gravity wave source. This feature has also been identified by *Swinbank et al.* (1998); *Pope et al.* (2000).

The broad spectrum simulations are then compared with the more complex coupled interactive simulations. The study indicates that the effective gravity wave acceleration in the northern hemisphere mesosphere during winter for the coupled interactive simulation

is smaller than that of the broad spectrum simulation, as identified in the test bed.

The difference in gravity wave acceleration between the schemes induces changes in the zonal mean wind, zonal mean temperature and the strength of stationary planetary waves in the northern hemisphere middle atmosphere. The coupled simulation was found to have a more unstable middle atmosphere compared to the spectral simulation.

The southern hemisphere stratosphere also shows differences in gravity wave acceleration between the two schemes during winter. This is demonstrated by an earlier breakdown of the westerly jet in the southern hemisphere pole in the broad spectrum simulation during spring. The stronger gravity wave acceleration in the broad spectrum simulation forces a stronger residual mean circulation in the southern hemisphere middle atmosphere, induces a stronger vertical advection of temperature in the winter middle atmosphere compared to that of the coupled interactive simulation. The stronger advection gradually warms the middle atmosphere in the broad spectrum simulation and effectively breaks down the zonal westerly jet earlier than that predicted in the coupled interactive simulation.

Further studies of the daily synoptic data during northern hemisphere winter have revealed that the SSW events have varying frequencies across the two schemes. The coupled interactive simulation shows more frequent warming events in the northern hemisphere winter than produced by the broad spectrum simulation. The daily data have also shown an indirect effect of gravity wave acceleration on the model's resolved waves and equatorial circulation.

It can therefore be suggested that the difference in gravity wave forcing between the two schemes not only has induces changes on climatological time scales, it also affects the middle atmosphere circulation on daily scales.

Although QBO was not simulated in the lower stratosphere by either scheme, the broad spectrum simulation shows a stronger westerly in the tropical lower stratosphere than that displayed by the coupled interactive simulation.

The results of these studies are quite encouraging, and it can be concluded that it is not only possible to parameterize broad spectrum gravity waves in a GCM, but parameterization of coupled interactive broad spectrum and monochromatic gravity waves can also be performed. The results of the two schemes successfully simulate atmospheric cir-

culation, and demonstrate sensitivity in the atmospheric dynamics due to difference in forcing induced by the gravity wave acceleration of the two schemes. Nevertheless, more experiments could be carried out to further refine the results, which were restricted due to limitations in computational resources available for the present work.

8.3 Further work

There are a number of areas in which the present work could be usefully extended. The behaviour of the two parameterization schemes could be further explored by varying values of tunable parameters used in the schemes, different source strengths of gravity waves, etc. These experiments could be useful in resolving a critical issue as to the superiority of the schemes. This implies some verification against observations.

Further work could be performed to study SSW events in the northern hemisphere polar winter across the two simulations. Gravity wave acceleration in both simulations could also be varied to validate their effects with the results presented in this thesis.

New experiments could also be performed by changing the parameters of the two schemes to simulate equatorial oscillations such as quasi-biennial oscillations and semiannual oscillations. It would be interesting to investigate whether one scheme can reproduce these oscillations better than the other, due to the differing nature of dissipation of gravity waves. Effects of these oscillations in the climatology could be studied and contrasted.

Differences in gravity wave parameterization clearly affect tropospheric circulation as has been discussed before. Further studies could be performed to analyze differences in tropospheric circulation and interactions between troposphere and middle atmosphere circulations induced by employing different gravity wave parameterization schemes in the UM.

It is clear that gravity wave parameterization schemes play a major role in simulating the troposphere as well as middle atmosphere dynamics in GCMs. With continued advancements in information technology, more powerful GCMs with higher resolution, are envisaged in the near future, which might be able to resolve gravity waves within their grids. Until then, gravity wave parameterization schemes are necessary for simulation of a real atmosphere which justifies continuing studies on the effects of different gravity wave

parameterization schemes in the climatology of the Earth's atmosphere.

Appendix A

The Unified Model

A.1 Primitive equations in the UM

The UM is a primitive equation model and all quantities are expressed in the SI units. The lower boundary of the model is defined as $p = p_\star$. The equations are expressed in the spherical polar coordinates (λ,ϕ), longitude and latitude respectively. The global models are based on the earth's axis of rotation and $\lambda = 0$ at the North and the South Poles. In order to use the same model for limited area, the equations are written for a general position of the coordinate pole. (λ_A,ϕ_A) are actual latitude and longitude. (λ_0,ϕ_0) are the actual longitude and latitude of the coordinate pole; (*Cullen et al.*, 1993).

The horizontal wind components in 'actual' latitude and longitude are given by (u_A,v_A) and the same relative to the coordinate pole. The conversion between these components is expressed as:

$$\begin{aligned} u &= \cos(ROT)u_A + \sin(ROT)v_A \\ v &= \cos(ROT)v_A - \sin(ROT)u_A \end{aligned} \tag{A.1}$$

or

$$\begin{aligned} u_A &= \cos(ROT)u - \sin(ROT)v \\ v_A &= \cos(ROT)v + \sin(ROT)u \end{aligned} \tag{A.2}$$

where,

$$\begin{aligned} \cos(ROT) \;=\; & \sin\lambda \sin(\lambda_A - \lambda_0)\sin\phi_0 + \\ & + \cos\lambda\cos(\lambda_A - \lambda_0) \end{aligned}$$

$$\sin(ROT) = -\cos\phi_0 \sin(\lambda_A - \lambda_0)/\cos\phi \tag{A.3}$$

The above mentioned equations only appear in the Coriolis terms given by:

$$\begin{aligned} f_1 &= 2\Omega\cos\phi_A \sin(ROT) \\ &= -2\Omega \sin\lambda \cos\phi_0 \\ f_2 &= 2\Omega\cos\phi_A \cos(ROT) \\ &= 2\Omega(\cos\phi\sin\phi_0 - \sin\phi\cos\lambda\cos\phi_0) \\ f_3 &= 2\Omega(\sin\phi\sin\phi_0 + \cos\phi\cos\lambda\cos\phi_0) \\ &= 2\Omega\sin\phi_A \end{aligned} \tag{A.4}$$

The zonal and meridional momentum balance, hydrostatic, thermal balance and continuity equations are then written as:

$$\begin{aligned} &\partial u/\partial t + (u/r_s\cos\phi)\partial u/\partial\lambda + (v/r_s)\partial u/\partial\phi + \dot{\eta}\partial u/\partial\eta + \\ &+ (1/r_s\cos\phi)[\partial\Phi/\partial\lambda + \frac{R(T_v+\mu T_s)}{p}\partial p/\partial\lambda] - \\ &- f_3 v + f_2\tilde{w} - (u/r_s)(v\tan\phi - \tilde{w}) = F_u \end{aligned} \tag{A.5}$$

$$\begin{aligned} &\partial v/\partial t + (u/r_s\cos\phi)\partial v/\partial\lambda + (v/r_s)\partial v/\partial\phi + \dot{\eta}\partial v/\partial\eta + \\ &+ (1/r_s)[\partial\Phi/\partial\phi + \frac{R(T_v+\mu T_s)}{p}\partial p/\partial\phi] + \\ &+ f_3 u - f_1\tilde{w} + (u^2/r_s)\tan\phi + v\tilde{w}/r_s = F_v \end{aligned} \tag{A.6}$$

$$\begin{aligned} &\partial\theta_L/\partial t + (u/r_s\cos\phi)\partial\theta_L/\partial\lambda + (v/r_s)\partial\theta_L/\partial\phi + \dot{\eta}\partial\theta_L/\partial\eta - \\ &- (1/\pi)\frac{(L_c q_c^L) + (L_c + L_f)q_c^F}{c_p T}(RT\omega/c_p p) = F_\theta \end{aligned} \tag{A.7}$$

$$\partial q_T/\partial t + (u/r_s\cos\phi)\partial q_T/\partial\lambda + (v/r_s)\partial q_T/\partial\phi + \dot{\eta}\partial q_T/\partial\eta = F_q \tag{A.8}$$

$$\partial/\partial\eta(r_s^2\partial p/\partial t) + (1/\cos\phi)\partial/\partial\lambda(ur_s\partial p/\partial\eta) + \partial/\partial\phi(vr_s\cos\phi\partial p/\partial\eta) + \\ + \partial/\partial\eta(\dot{\eta}r_s^2\partial p/\partial\eta) = 0 \qquad \text{(A.9)}$$

The quantities F_u, F_v, F_θ and F_q are source terms. They also include any diffusion term necessary for computational reasons. The hydrostatic relation is given by:

$$\begin{aligned} \partial\phi/\partial\eta &= -[R(T_v + \mu T_s)/p]\partial p/\partial\eta \\ &= -c_p(\theta_v + \mu\theta_s)\partial\Pi/\partial\eta \end{aligned} \qquad \text{(A.10)}$$

where $\Pi = (p/100000)^\kappa$ and θ_v is the virtual potential temperature. The approximate vertical velocity $\tilde{w}$ is defined as:

$$\begin{aligned} \tilde{w} = \\ &- (RT_s/gp)[-(1/r_s^2\cos\phi)\int_0^n [\partial/\partial\lambda(ur_s\partial p/\partial\eta) + \partial/\partial\phi(vr_s\cos\phi\partial p/\partial\eta)]d\eta + \\ &+ (u/r_s\cos\phi)\partial p/\partial\lambda + (v/r_s)\partial p/\partial\phi] \end{aligned} \qquad \text{(A.11)}$$

The detailed derivation of the finite difference schemes, the advection scheme and diffusion and divergence damping are given in (*Cullen et al.*, 1993).

A.2 Grid and coordinate system

The vertical coordinate system of the UM is terrain-following near the surface but uses constant pressure surfaces higher up (*Swinbank*, 1989). The lower boundary follows the Earth's topography where the surface pressure is defined. Up to 100 hPa, the boundaries of these layers follow a generalized σ coordinate. From 100 hPa upwards these coordinate surfaces are constant pressure surfaces. The lower layers have equal divisions in pressure p, and above 100 hPa the layers have equal divisions in log pressure, as in figure A.1. The σ-coordinate system can be expressed as

$$(\sigma = p/p_\star), \qquad \text{(A.12)}$$

where p_s is the surface pressure. The idea of the hybrid pressure level was proposed by (*Arakawa and Lamb*, 1977). A suitable terrain-following coordinate η can be defined as the monotonic function of pressure p and depends on p_s.

$$\eta(p, p_s), \text{where} \tag{A.13}$$

$$\eta(0, p_s) = 0 \tag{A.14}$$

and

$$\eta(p_s, p_s) = 1. \tag{A.15}$$

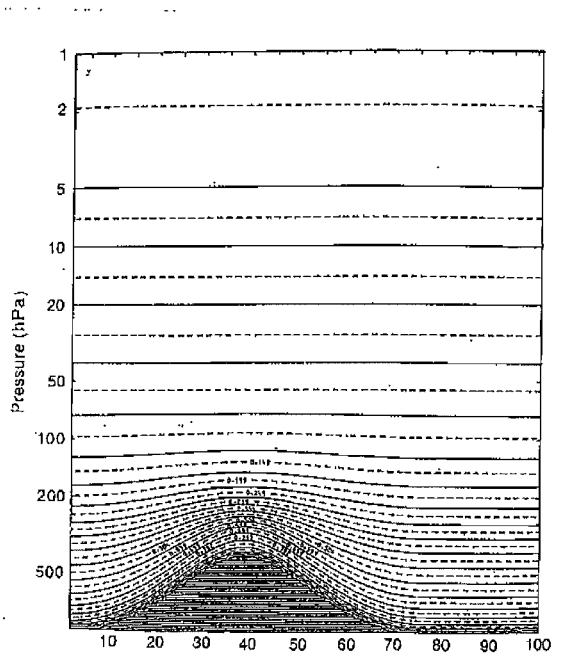

Figure A.1: Hybrid vertical coordinates of the UM. The vertical levels of the climate mode of the UM extends up to 0.01 hPa.

The simple relation used to define pressure in η surface is

$$p = Ap_0 + Bp_s, \tag{A.16}$$

where $A = 0$ near the surface and $B = 0$ in the stratosphere. The transition from σ to pressure can be specified by choosing suitable values of A and B. The reference pressure $p_0 = 1000$ hPa and η is defined, for convenience, as

$$\eta = A + B.$$

The horizontal grids are defined using spherical polar coordinates with latitude (*phi*) and longitude (*lambda*) (*Gadd*, 1985). The variables in the horizontal are arranged according to the Arakawa B-grid. The surface pressure ($p_\star$), potential temperature (θ) and humidity mixing ratio (q) are provided at the corner points, while the geopotential (Φ) and the vertical velocity (w) are diagnosed at the corner points. The horizontal components of the wind velocity (u, v) are predicted at the centre of the grid boxes. Figure A.2 illustrates the distribution of the variables in the horizontal coordinates.

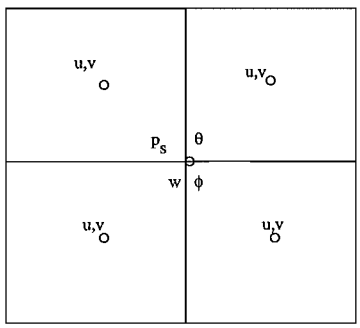

Figure A.2: Grid structure to show the positions of the variables

Appendix B

Geostrophic Assumption

The scale analysis of the momentum equations, 2.1 and 2.2, indicates that the Coriolis force is approximately equal to the pressure gradient force which implies that they are in geostrophic balance. That is, $u \equiv u_g$ and $v \equiv v_g$ where u_g and v_g are geostrophic winds and can be expressed as;

$$u_g = -\frac{1}{fa}\frac{\partial \Phi}{\partial \phi} \tag{B.1}$$

and

$$v_g = \frac{1}{fa\cos\phi}\frac{\partial \Phi}{\partial \lambda} \tag{B.2}$$

The above equations are called the *geostrophic equations.* The simplified equations, 2.6 and 2.7, can be applied for large scale, low frequency extratropical flows. The geostrophic wind equations can be used to estimate the horizontal wind if geopotential fields are known.

The geostrophic equations (above) can then be combined with the *hydrostatic equation,* equation 2.3, to obtain the *thermal wind* relation;

$$\frac{\partial u_g}{\partial z} = -\frac{R}{Hfa}\frac{\partial T}{\partial \phi} = -\frac{R}{Hf}e^{-\kappa z/H}\frac{\partial \theta}{\partial y} \tag{B.3}$$

and

$$\frac{\partial v_g}{\partial z} = -\frac{R}{Hfa\cos\phi}\frac{\partial T}{\partial \lambda} = \frac{R}{Hf}e^{-\kappa z/H}\frac{\partial \theta}{\partial x} \tag{B.4}$$

The *thermal wind* equations relate the shear of the geostrophic wind in a vertical layer to the horizontal gradient of the mean temperature of the layer.

Appendix C

Zonal-Mean Theory and Eliassen-Palm Flux

The atmospheric phenomena involve interactions of the mean flow with disturbances due to small scale waves and eddies which are superimposed on the mean flow. Hence, the primitive equations can be reformulated on the basis of a "mean flow" term and a "perturbation" term, such as

$$u(\lambda, \phi, z, t) \equiv \bar{u} + u' \tag{C.1}$$

where $\bar{u}$ is the mean flow term, u' is the perturbation term and

$$\bar{u}(\phi, z, t) = \frac{1}{2\pi} \int_0^{2\pi} u(\lambda, \phi, z, t) \tag{C.2}$$

The above formulation is called 'quasi geostrophic formulation' and the primitive equations, equations $A.1$ to $A.5$ can be reformulated with the above approximation. The equations are known as 'Eulerian-mean equations', (*Andrews et al.*, 1987). It is useful for large-scale, slow moving dynamical structures. However, the quasi-geostrophic equations provide very little information about the behaviour of the system in the presence of small scale motions, such as, gravity waves. The response of the zonal mean flow due to a specified 'eddy momentum flux' $\overline{v'u'}$ or 'eddy heat flux' $\overline{v'\theta'}$ is limited with the quasi-geostrophic approximation. Also, the physical properties of the small scale waves which control these wave fluxes cannot be anticipated from the 'Eulerian-mean equations'.

These drawbacks are dealt with by standard 'Transformed Eulerian Mean' (TEM) equations, (*Andrews and McIntyre*, 1976), at first by defining a 'residual mean meridional circulation' or 'diabatic circulation' $(0, \bar{v}^*, \bar{u}^*)$, as

$$\bar{v}^* \equiv \bar{v} - \frac{R}{\rho_0 H} \frac{\partial}{\partial z} (\rho_0 \frac{\overline{v'T'}}{N^2}) \tag{C.3}$$

and

$$\bar{w}^* \equiv \bar{w} - \frac{R}{Ha \cos\phi} \frac{\partial}{\partial \phi} (\frac{\overline{v'T'}}{N^2} \cos\phi) \tag{C.4}$$

The values of $\bar{v}$ and $\bar{w}$ in *Eulerian-mean equations* are substituted by v^* and w^* to produce

Transformed Eulerian Mean (TEM) equations,

$$\frac{\partial \bar{u}}{\partial t} + \frac{\bar{v}^*}{a\cos\phi}\frac{\partial(\bar{u}\cos\phi)}{\partial\phi} - f\bar{v}^* + \bar{w}^*\frac{\partial \bar{u}}{\partial z} - \bar{X} = \frac{\nabla F}{\rho_0 a\cos\phi}, \tag{C.5}$$

$$\bar{u}(f + \bar{u}\tan\phi/a) + \frac{1}{a}\frac{\partial \bar{Phi}}{\partial\phi} = G, \tag{C.6}$$

$$\frac{\partial\bar{\Phi}}{\partial z} - \frac{R\bar{T}}{H} = 0, \tag{C.7}$$

$$\frac{\partial \bar{v}^*}{\partial\phi} + \frac{\bar{v}^*\tan\phi}{a} + \frac{\partial(\rho_0\bar{w}^*)}{\rho_0\partial z} = 0, \tag{C.8}$$

$$\frac{\partial\bar{T}}{\partial t} + \frac{\bar{v}^*}{a}\frac{\partial\bar{T}}{\partial\phi} + \bar{w}^*N^2 - \frac{\bar{J}}{c_p} = -\frac{\partial}{\rho_0\partial z}[\rho_0(\frac{\partial\bar{T}}{\partial\phi}\frac{v'\bar{T}'}{N^2} + w'\bar{T}')] - \frac{\kappa\bar{w}'\bar{T}'}{H} \tag{C.9}$$

Here, G represents all the terms that lead to a departure from the gradient-wind balance between $\bar{u}$ and $\bar{\Phi}$, however, the dynamical effects of G are not primarily important (*Andrews et al.*, 1987).

$F \equiv (0, F^\phi, F^z)$ is the 'Eliassen-Palm Flux' (E-P flux), which has components,

$$F^\phi = \rho_0 a\cos\phi[-\bar{v'u'} - \frac{R}{H}\frac{\partial\bar{u}}{\partial z}\frac{\bar{v'T'}}{N^2}] \tag{C.10}$$

and

$$F^z = \rho_0 a\cos\phi[(f - \frac{1}{a\cos\phi}\frac{\partial(\bar{u}\cos\phi)}{\partial\phi})\frac{R}{H}\frac{\bar{v'T'}}{N^2}] \tag{C.11}$$

N is the buoyancy frequency and can be defined as the frequency of oscillation of an air parcel displaced vertically from its equilibrium level to a stable stratified level.

$$N^2 = g\frac{T}{T_s}\frac{\partial\ln\theta}{\partial z} = \frac{R}{H}\frac{\partial T}{\partial z} + \frac{\kappa T}{H} \tag{C.12}$$

Here, N^2 is the measure of static stability of the atmosphere; if $N^2 < 0$, the atmosphere is statically stable. θ in the above equation is the potential temperature defined as the temperature a parcel of dry air at pressure p and temperature T would have if it were expanded or compressed adiabatically to a standard pressure p_s. The expression is given below

$$\theta = T(p_s/p)^{R/c_p} \tag{C.13}$$

The main advantage of the TEM formulation is that a wave driving conservation law can be applied such as

$$\frac{\partial A}{\partial t} + \nabla \cdot F = D + o(\alpha^3) \tag{C.14}$$

where, A is the wave action density and D represents diabatic frictionless effects. According to the above expression, the wave driving will be zero ($\nabla \cdot F = 0$) if the waves present in the system are steady, ($\frac{\partial A}{\partial t} = 0$) and conservative, ($D = 0$). For a linear steady conservative waves, the RHS of the equation vanishes.

Appendix D

Extra Results from Single Column Testbed

D.1 Tropospheric filtering of gravity waves: A typical summer hemisphere wind profile

D.1.1 Zonal momentum flux and acceleration

Figures D.1 and D.2 show a typical summer hemisphere zonal wind, total zonal momentum flux and zonal acceleration for the gravity wave spectrum launched from the ground (SUR) and from the tropopause (TRO), respectively.

The net zonal momentum flux in the troposphere is negative for SUR due to the westerly shear of the tropospheric zonal wind which filters out the waves with similar phase, (*Manzini and McFarlane*, 1998). In the upper tropospheric and the lower stratospheric regions, the value of the eastward momentum flux is strongly reduced and the value is even lower than TRO in a similar region, figure D.2. The zonal momentum flux is positive in the summer hemisphere above the tropopause, for both SUR and TRO.

The zonal acceleration in SUR has a value ($350 m/s/day$) much smaller than that of TRO ($600 m/s/day$).

The results are interpreted as follows. The gravity wave spectra gets filtered out by the tropospheric jets in SUR, as already suggested. Hence, when the zonal wind shear changes in the mesosphere, no change in the momentum flux is observed and the total zonal forcing is experienced at the top most layer of the model. Whereas, for TRO, the gravity wave spectrum has not been filtered out by the westerly wind at the troposphere. Hence, when the change of the wind shear takes place in the mesosphere, the part of the spectra which has not been filtered out by tropospheric wind starts breaking down producing a forcing at a lower altitude than observed in SUR. It can be inferred from the results that tropospheric filtering of waves reduces zonal acceleration at the uppermost model level.

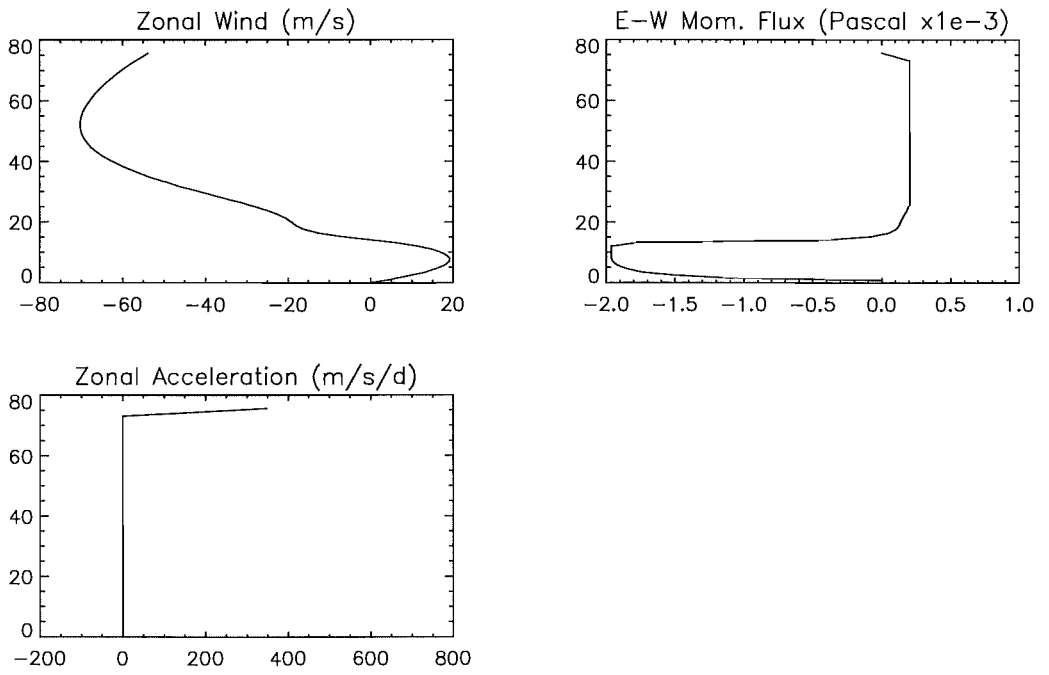

Figure D.1: Typical summer mid-latitude wind profile, zonal momentum flux and zonal acceleration when spectra are launched from ground

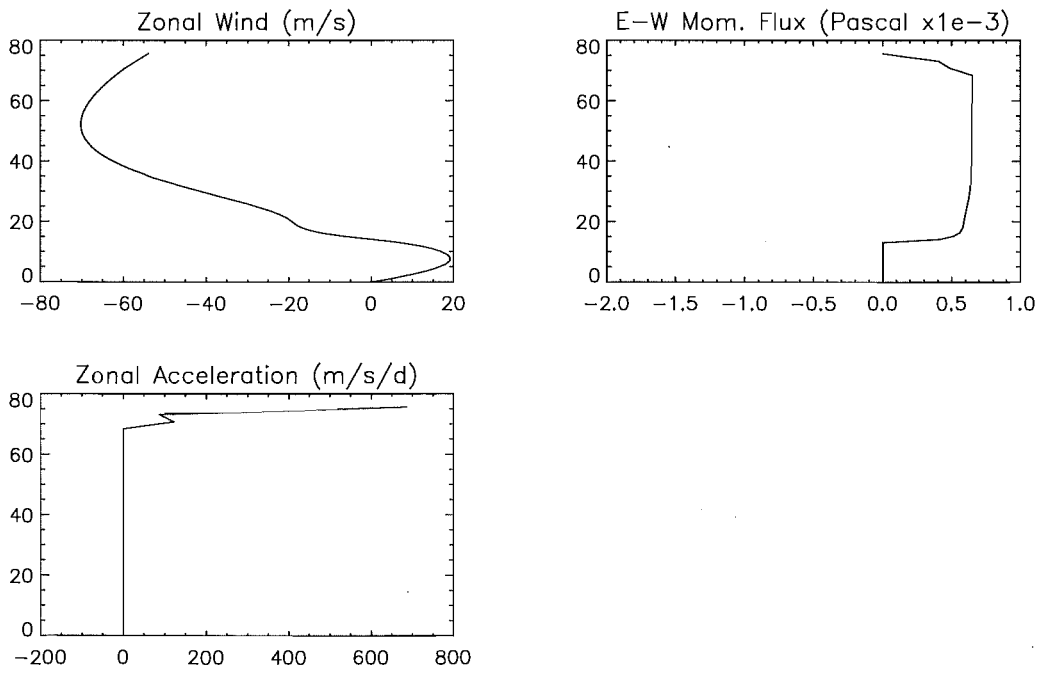

Figure D.2: Summer hemisphere zonal wind, zonal momentum flux and zonal acceleration with summer wind profile when spectra are launched from tropopause.

D.1.2 Meridional momentum flux and acceleration

Meridional momentum flux and acceleration due to broad spectrum of waves launched from the ground (*SUR*) and from the tropopause (*TRO*)are exhibited in figures D.3 and D.4, respectively.

From the figure D.3, it is seen that a negative meridional momentum flux is deposited in the upper troposphere and lower stratosphere region for *SUR* due to filtering of the gravity wave spectrum by positive shear of meridional wind. In *TRO*, the meridional momentum flux in the lower stratosphere has a positive value. The spectrum gets directly filtered through the stratospheric wind which allows only the positive part of the spectrum to travel upwards, as shown in fig. D.4. Above that height, the magnitude of meridional momentum flux are similar in both cases while their signs are different, as shown in figures D.3 and D.4. The value of meridional acceleration in *SUR* is much smaller than *TRO*.

Comparison between *SUR* and *TRO* shows that the meridional momentum and acceleration values are negative in *SUR* due to low level filtering of broad spectrum waves by meridional wind. It should be emphasized here that momentum flux deposition of gravity waves can directly affect planetary waves either by damping or by providing a generation mechanism. It may even influence planetary waves indirectly through the changes it induces on zonal mean flow, (*Manzini and McFarlane* (1998) and *Osprey and Lawrence* (2001)).

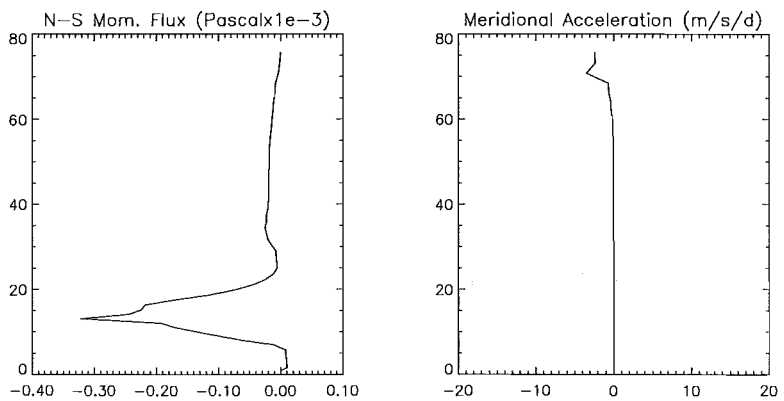

Figure D.3: Meridional momentum flux and acceleration with summer wind profile and spectra launched at ground.

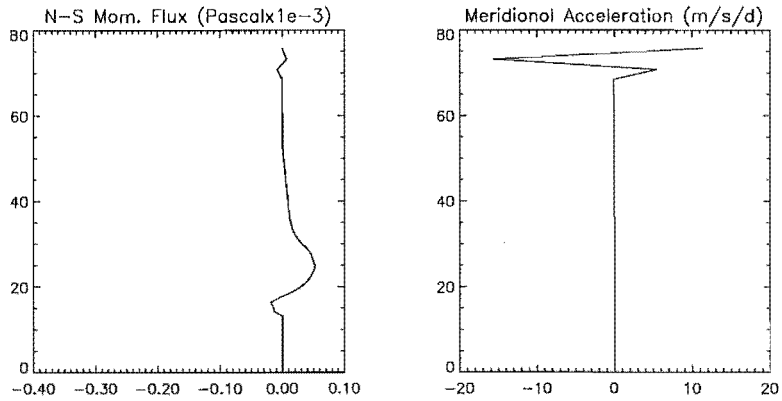

Figure D.4: Meridional momentum flux and acceleration with summer wind profile and spectra launched at tropopause.

D.2 Tropospheric filtering of gravity waves: A typical winter hemisphere wind profile

D.2.1 Zonal momentum flux and acceleration

Zonal momentum flux and acceleration due to a typical winter hemisphere wind profile is shown in figure D.5 and figure D.6. The zonal momentum flux for spectra launched from the ground in *SUR* is stronger than in *TRO*. The mid-latitude zonal momentum flux in the upper stratosphere and the lower mesosphere is negative as is expected in the winter hemisphere. This is because the westerly zonal wind in both troposphere and stratosphere filters out part of the incident spectrum which has the same phase as the zonal wind.

It can also be observed from the figures D.5 and D.6 that zonal momentum flux deposition has commenced at a lower altitude in *SUR* than that of *TRO*. This is reflected in the zonal mean acceleration of both cases.

The zonal acceleration in *SUR* initiates at a lower altitude than in *TRO*. The stronger acceleration due to gravity waves at a lower altitude in *SUR* can contribute to a stronger deceleration of the zonal mean flow as compared to *TRO*, *Manzini and McFarlane* (1998).

Comparison of the figures D.1 and D.5, and D.2 and D.6 reveals that the tropospheric zonal wind shear (westerly in all the cases) filters out a part of the gravity wave spectrum creating a spectral imbalance right at the bottom of the model. A negative momentum flux is observed during both summer and winter,figures D.1 and D.5, below 16km due to

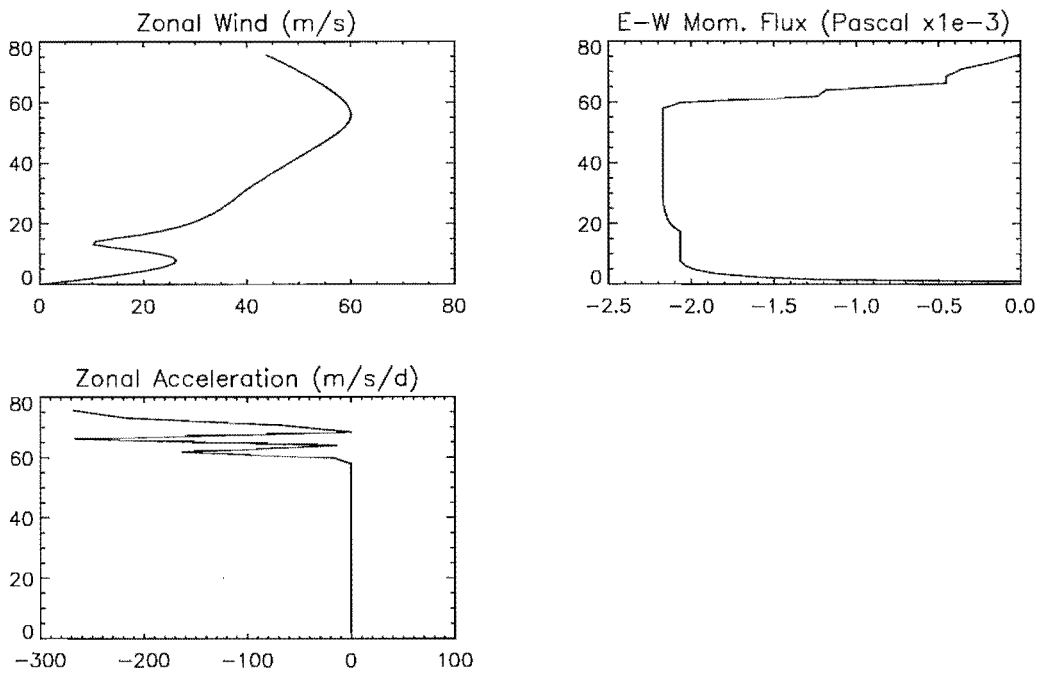

Figure D.5: Mid-latitude winter hemisphere zonal wind, momentum flux and acceleration when spectra are launched from the ground.

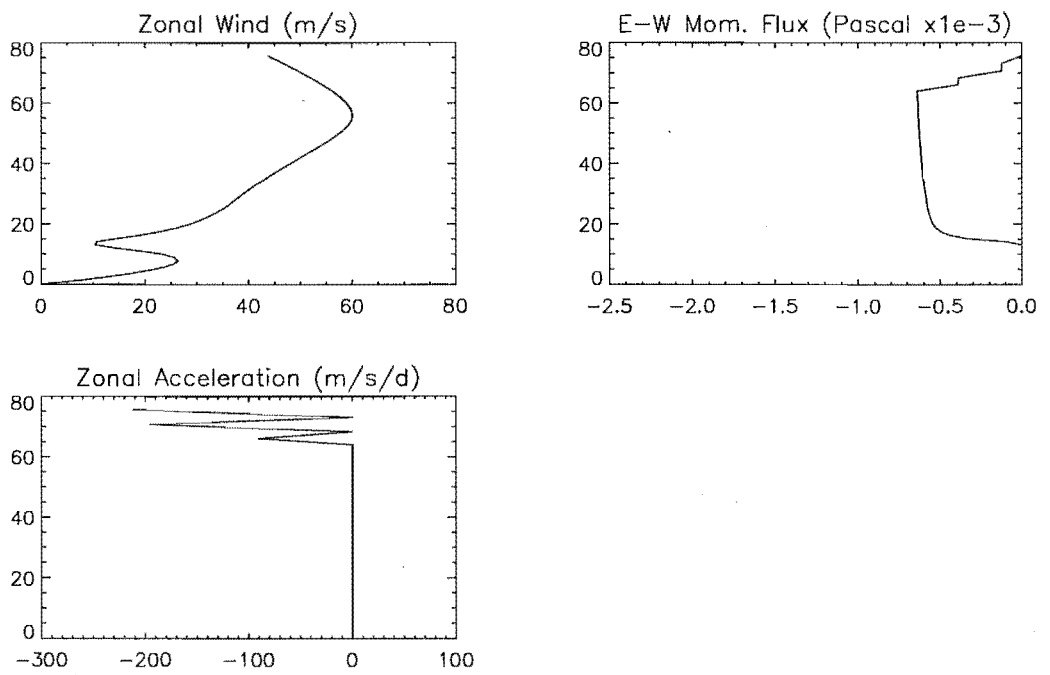

Figure D.6: Zonal momentum flux and acceleration when spectra are launched from tropopause.

the tropospheric filtering of the waves.

D.2.2 Meridional momentum flux and acceleration

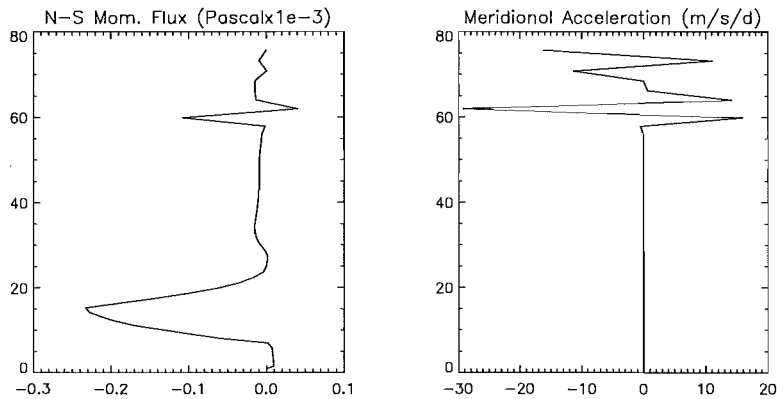

Figure D.7: Meridional momentum flux and acceleration with winter wind profile and spectra launched at ground.

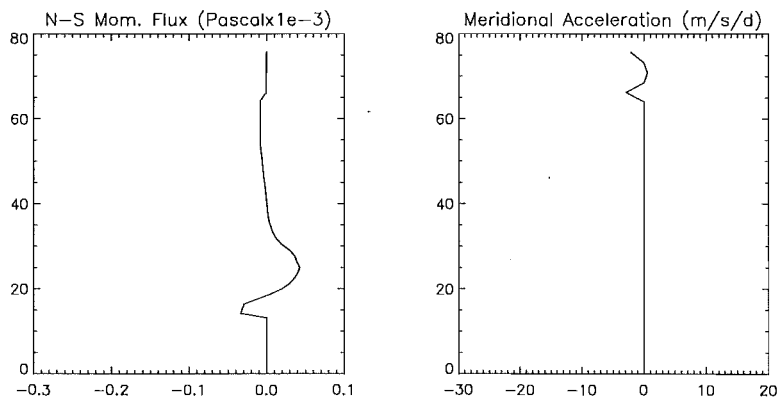

Figure D.8: Meridional momentum flux and acceleration with winter wind profile and spectra launched at tropopause.

Meridional momentum flux for *SUR* and *TRO* are shown in figures D.7 and D.8, respectively.

The meridional flux is negative in the upper troposphere and lower stratosphere region for *SUR* (-0.25×10^{-3} N/m^2). This value goes down to almost -0.01×10^{-3} N/m^2 above $30km$. In *TRO*, there is a deposition of negative meridional momentum flux in the lower

stratosphere region which is weaker ($-0.03 * 10^{-3}$ N/m^2) than in *SUR*. The flux becomes positive with the change in the meridional wind shear, and above the stratopause the meridional momentum flux has a negative value till it reaches 80 km height. The values of meridional momentum flux in summer of *SUR* compares well with that of winter, figures D.3 and D.7. The same is true for *TRO*.

However, the acceleration values at the mesospheric levels for *SUR* are much stronger than *TRO*. This may be caused due to rapid fluctuations in the meridional momentum flux at mesospheric altitudes.

From the above analyses (figures D.1 and D.5, and D.2 and D.6) it can be inferred that the tropospheric zonal wind shear (westerly for all cases) filter out a part of gravity wave spectra creating a spectral imbalance right at the bottom of the model - an effect which has been discussed earlier. Due to tropospheric filtering of the waves, a negative zonal momentum flux is observed below 16 km in both figures D.1 and D.5. The change in momentum flux due to tropospheric filtering of broad spectrum waves contributes to a change in the zonal acceleration which can induce changes in the zonal mean flow.

D.3 Coupled-interactive gravity wave scheme in the presence of high mountains

D.3.1 A typical summer hemisphere wind profile

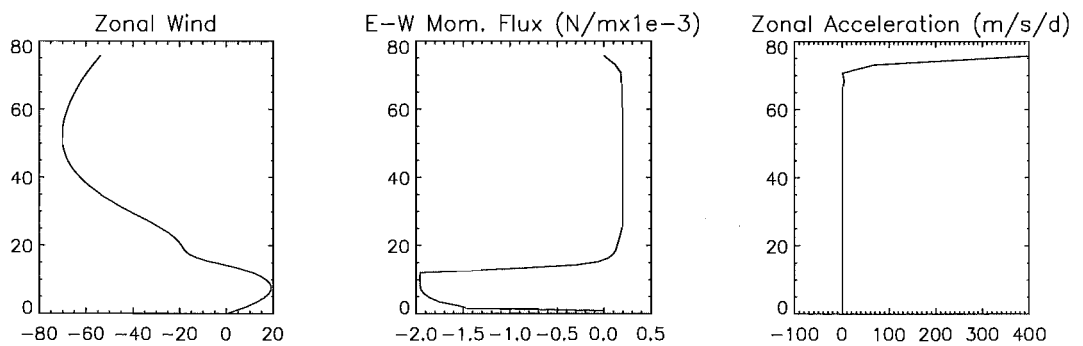

Figure D.9: Mid-latitude summer hemisphere zonal wind, momentum flux and acceleration in the presence of high mountains.

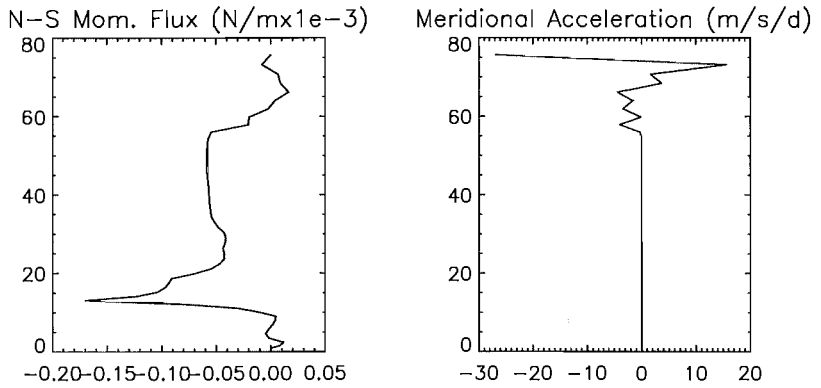

Figure D.10: Meridional momentum flux and acceleration with summer zonal wind profile in the presence of high mountains.

D.4 Coupled-interactive gravity wave scheme in the presence of high mountains

D.4.1 A typical winter hemisphere wind profile

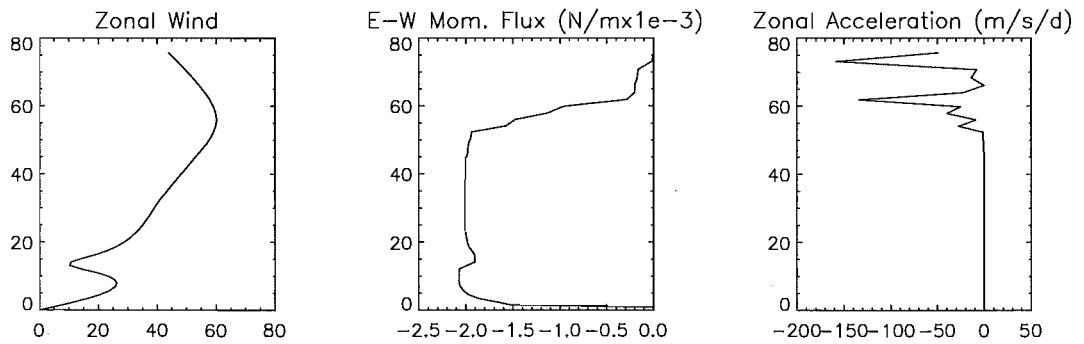

Figure D.11: Mid-latitude winter hemisphere zonal wind, momentum flux and acceleration in the presence of high mountains.

D.5 Coupled-interactive gravity wave scheme in the presence of high mountains

D.5.1 A typical summer hemisphere wind profile

The zonal wind depicting mid-latitude summer wind profile, zonal and meridional momentum fluxes and forcings are shown in the figure D.13. Values of zonal stress and

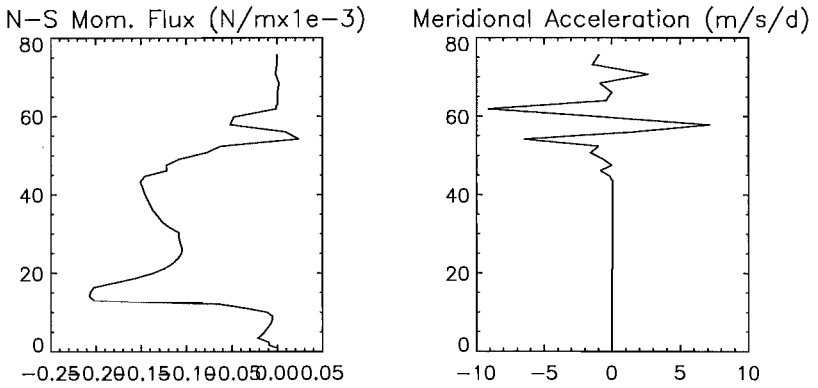

Figure D.12: Meridional momentum flux and acceleration with winter zonal wind profile in the presence of high mountains.

acceleration in *LOM* is comparable to the values obtained in *HIM*, figure D.9. It is also comparable to the values in *SUR*, figure D.1. This may indicate that in the presence of low altitude mountains, there is not much variability in gravity wave induced zonal stress and acceleration among *SUR*, *LOM* and *HIM*.

The zonal wind depicting mid-latitude summer wind profile, zonal and meridional momentum fluxes and forcings are shown in the figure D.13. Values of zonal stress and acceleration in *LOM* is comparable to the values obtained in *HIM*, figure D.9. It is also comparable to the values in *SUR*, figure D.1. This may indicate that in the presence of low altitude mountains, there is not much variability in gravity wave induced zonal stress and acceleration among *SUR*, *LOM* and *HIM*.

The meridional momentum flux in *LOM* and *HIM* has similar value in the troposphere, although the value for *HIM* in stratosphere is more negative. The meridional forcing in *LOM* is very small as compared to the other cases and hence its effects in the upper atmosphere can be ignored.

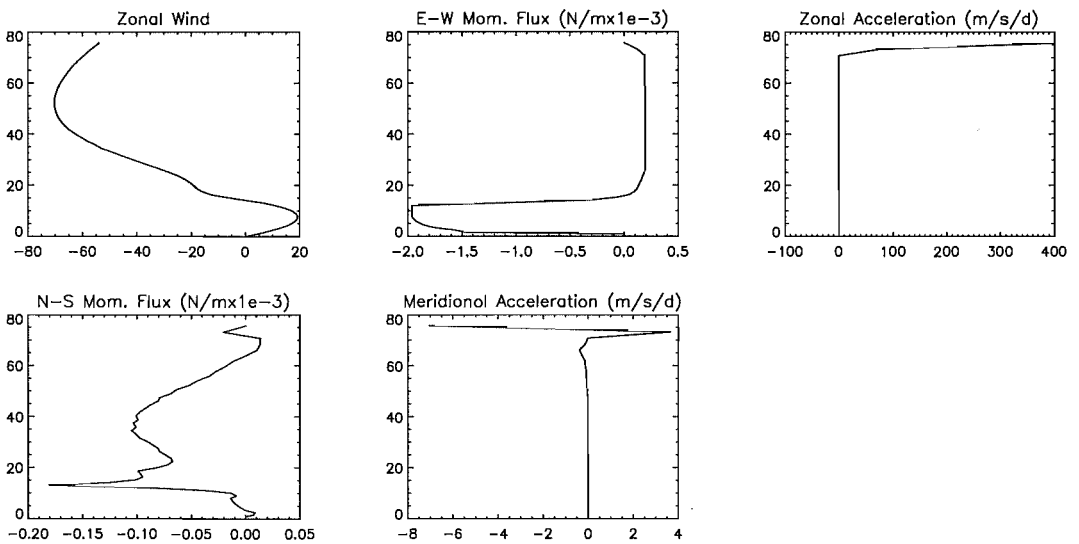

Figure D.13: Mid-latitude winter hemisphere zonal wind, zonal and meridional momentum flux and zonal and meridional acceleration in the presence of low mountains.

Appendix F

List of Symbols

a	Radius of the earth
c	Ground based zonal phase speed of gravity waves
f	Coriolis parameter
k	Horizontal wave number
m	Vertical wave number
p	Pressure
p_s	Standard constant pressure
t	Time
u	x component of velocity
v	y component of velocity
w	z component of velocity
x, y, z	Eastward, northward and upward distance respectively
E	Energy
F	Flux
F_r	Froude number
H	Scale height
J	Number of azimuths in a broad spctrum gravity wave
M	Universal vertical wave number spectrum
N	Buoyancy frequency
Q	Azimuth of a monochromatic gravity wave
R	Gas constant
R_i	Richardson number
T	Temperature
U	Horizontal velocity scale
X	Zonal turbulent drag force
δ	Standard deviation
η	Efficiency factor in Lindzen parameterization
θ	Potential temperature
κ	Ratio of gas constant to specific heat at constant pressure

λ	Longitude
ρ	Density
ρ_s	Standard density
τ	Orographic surface stress
σ	Root mean square wind variance
ϕ	Latitude
Φ	Geopotential
Π	Exner function
ω	Doppler shifted frequency of a broad spectrum gravity wave
Ω	Local intrinsic frequency of a broad spectrum gravity wave
$\mathbf{\Omega}$	Angular velocity of the earth

References

Coupling processes in the lower and middle atmopshere, vol. 387 of *C:Mathematical and Physical Sciences*. NATO Advanced Research Workshop, 1992.

Igwoc final report, 2001.

Allen, S. J., and R. A. Vincent, Gravity wave activity in the lower atmosphere: Seasonal and latitudinal variations, *J. Geophys. Res.*, *100*(D1), 1327–1350, 1995.

Andrews, D. G., J. R. Holton, and C. B. Leovy, *Middle atmosphere dynamics*. Academic Press, 1987.

Andrews, D. J., and M. E. McIntyre, Planetary waves in horizontal and vertical shear: The generalized eliassen-palm relation and the mean zonal acceleration, *Journal of the Atmospheric Sciences*, *33*, 2031, 1976.

Arakawa, A., and V. R. Lamb, *Methods in Computational Physics*, vol. 17, chap. 5, pp. 174–264. Academic Press, 1977.

Bacmiester, J. T., P. A. Newman, B. L. Gray, and K. R. Chan, An algorithm for forecasting mountain wave related turbulence in the stratosphere, *Weather and Forecasting*, *9*, 241–253, 1994.

Braesicke, P., and U. Langematz, On the occurance and evolution of extremely high temperatures at the polar winter stratospause - a gcm study, *Geophysical Research Letters*, *27*, 1467–1470, 2000.

Butchart, N., and J. Austin, Middle atmosphere climatologies from the troposphere-stratosphere configuration of the ukmo's unified model, *J. Atmos. Sci.*, *55*(17), 2782–2809, 1998.

Canziani, P. O., and J. R. Holton, Kelvin waves and the quasi-biennial oscillation: An observational analysis, *Journal of Geophysical Research*, *103*(D24), 31509–31521, 1998.

Charney, J. G., R. Fjortoft, and J. von Newmann, Numerical integration of the barotropic vorticity equation, *Tellus*, *2*, 237–254, 1950.

Coy, L., and R. Swinbank, The characteristics of stratospheric winds and temperatures produced by data assimilation., *Journal of Geophysical Research*, *102*, 25763–25781, 1997.

Cullen, M. J. P., The unified forecast/climate model, *The Meteorological Magazine*, *122*(1449), 81–94, 1993.

Cullen, M. J. P., and T. Davies, A conservative split-explicit integration scheme with fourth-order horizontal advection, *Q. J. R. Meteorol. Soc.*, *117*, 993–1002, 1991.

Cullen, M. J. P., T. Davies, and M. H. Mawson, Unified model documentation paper no.10, conservative finite difference schemes for a unified forecast/climate model, 1993.

Dewan, E. M., and R. E. Good, Saturation and the 'universal' spectrum for vertical profiles of horizontal scalar winds in atmosphere, *Journal of Geophysical Research*, *91*, 2742–2748, 1986.

Dunkerton, T. J., The role of gravity waves in the quasi-biennial oscillation, *J. Geophys. Res.*, *102*(D22), 26053–26076, 1997.

Dunkerton, T. J., and M. P. Baldwin, Quasi-biennial modulation of planetary-wave fluxes in the northern hemisphere winter, *Journal of the Atmospheric Sciences*, *48*, 1043–1061, 1991.

Eckermann, S. D., and W. K. Hocking, Effect of superposition on measurements of atmospheric gravity waves: A cautionary note and some reinterpretations, *Journal of Geophysical Research*, *94*(D5), 6333–6339, 1989.

Epsy, P. J., and R. Huppi, The intertrropical convergence zone as a short-period mesospheric gravity waves near the equator, *Journal of Atmospheric and Solar-Terrestrial Physics*, *59*, 1665–1671, 1997.

Erlebach, P., U. Langematz, and S. Pawson, Simulations of stratospheric sudden warmings in the berlin troposphere-stratosphere-mesosphere gcm, *Annales Geophysicae*, *14*, 443–463, 1996.

Farman, J. C., B. G. Gardiner, and J. D. Shanklin, Large losses of total ozone in antarctica reveal seasonal clox/nox interaction, *Nature*, *315*, 207–210, 1985.

Fels, S. B., Radiative-dynamical interactions in the middle atmosphere, *Adv. Geophysics*, *28 A*, 277–300, 1985.

Fleming, L. E., S. Chandra, J. J. Barnett, and M. Corey, Zonal mean temperature, pressure, zonal mean wind and geopotential height as a function of latitude, *Adv. Space Research, 10*, 11–59, 1990.

Fritts, D. C., and H. G. Chou, An inveatigation of the vertical wavenumber and frequency spectra of gravity wave motions in the lower stratosphere, *J. Atmos. Sci., 44*(24), 3610–3624, 1987.

Gadd, A. J., The 15-level weather prediction model, *Meteorological Magazine, 114*, 222–226, 1985.

Garcia, R. R., and S. Solomon, The effect of breaking gravity waves on the dynamics and chemical composition of the mesosphere and lower thermosphere, *J. Geophys. Res., 90*(D2), 3850–3868, 1985.

Gavrilov, N. M., Climatology and hydrodynamic sources of internal gravity waves in the middle and upper atmosphere, in *Gravity Wave Processes; Thier Parameterization in Global Climate Models*, edited by K. Hamilton, vol. 50 of *Series 1:Global Environment Change*, chap. 4, p. 16. Springer, 1996.

Geller, M. A., Tropospheric forcing of the middle atmosphere, in *Role of stratosphere in global change*, vol. 8 of *Series 1:Global Environment Change*. Springer, 1997.

Gregory, D., G. J. Shutts, and J. R. Mitchell, A new gravity wave drag scheme incorporating anisotropic orography and low level wave breaking: Impact upon the climate of the uk met. office unified model, *Q. J. R. Meteorol. Soc., 124*, 463–493, 1998.

Grotjahn, R., *Global Atmospheric Circulations, Observations and Theories*. Oxford University Press, 1993.

Haynes, P. H., C. J. Marks, M. E. McIntyre, T. G. Shepherd, and K. P. Shine, On the downward control of extratropical diabatic circulation., *Journal of the Atmospheric Science, 48*, 651–678, 1991.

Hines, C. O., Doppler-spread parameterization of gravity wave momentum deposition in the middle atmosphere. part 1:basic formulation, *J. Atmos. Terr. Phys., 59*(4), 371–386, 1997a.

Hines, C. O., Doppler-spread parameterization of gravity wave momentum deposition in the middle atmosphere. part 2:broad and quasi-monochromatic spectra and implementation, *J. Atmos. Terr. Phys., 59*(4), 387–400, 1997b.

Hirota, I., Some problems relating to the observed characteristics of gravity waves in the middle atmosphere, in *Gravity Wave Processes; Thier Parameterization in Global Climate Models*, edited by K. Hamilton, vol. 50. 1996.

Holton, J. R., *An Introduction to Dynamic Meteorology*, chap. 11, pp. 296–322. Academic Press, second edition edn., 1979.

Holton, J. R., The role of gravity wave induced drag and diffusion in the momentum budget of the mesosphere, *J. Atmos. Sci.*, *39*, 791–799, 1982.

Holton, J. R., *An Introduction to Dynamic Meteorology*. Academic Press, third edition edn., 1992.

Holton, J. R., and W. M. Wehrbein, A numerical model of the zonal mean circulation of the middle atmosphere, *Pure and Applied Geophysics*, pp. 284–306, 1980.

Kodera, K., The solar and equatorial qbo influences on the stratospheric circulation during the early northern hemisphere winter, *Geophysical Research Letters*, *18*, 1023–1026, 1991.

Labitzke, K., and H. vaan Loon, Some influences responsible for the interannual variations in the stratosphere of the northern hemisphere, in *Role of stratosphere in global change*, vol. 8 of *Series 1:Global Environment Change*. Springer, 1997.

Langematz, U., and S. Pawson, The berlin troposphere-stratosphere-mesosphere gcm: Climatology and forcing mechanisms, *Quarterly Journal of Royal Met. Society*, *123*, 1075–1096, 1997.

Lawrence, B. N., The effect of parameterized gravity wave drag on simulations of the middle atmosphere during northern winter 1991/1992-general evolution., in *Gravity Wave Processes; Thier Parameterization in Global Climate Models*, vol. 50 of *Series 1:Global Environment Change*. Springer, 1997a.

Lawrence, B. N., Some aspects of the sensitivity of stratospheric climate simulation to model lid, *Journal of Geophysical Research*, *102*, 23805–23811, 1997b.

Leovy, C., Simple models of thermally driven mesospheric circulation, *Journal of the Atmospheric Sciences*, *21*, 327–341, 1964.

Lilly, D. K., J. M. Nicholls, R. M. Chervin, P. J. Kennedy, and J. B. Klemp, Aircraft measurements of wave momentum flux over the colorado rocky mountains, *Q. J. R. Meteorol. Soc.*, *108*, 625–642, 1982.

Lindzen, R. S., Turbulence and stress owing to gravity wave and tidal breakdown, *Journal of Geophysical Research, 86*, 9707–9714, 1981.

Manney, G. L., R. W. Zurek, A. O'Neill, and R. Swinbank, On the motion of air through stratospheric polar-vortex, *Journal of the atmospheric Sciences, 51*, 2973–2994, 1994.

Manney, G. L., R. Swinbank, S. T. Massie, M. E. Gelman, A. J. Miller, R. Nagatani, A. O'Neill, and R. W. Zurek, Comparison of u.k. metereological office and us national metereological center stratospheric analysis during northern and southern winters, *Journal of Geophysical Research, 101*, 10311–10334, 1996.

Manzini, E., and N. A. McFarlane, The effect of varying the source spectrum of a gravity wave parameterization in a middle atmosphere gcm, *Journal of Geophysical Research, 103*(D24), 31523–31539, 1998.

Matsuno, T., Vertical propagation of stationary planetary waves in the winter northern hemisphere, *Journal of the Atmospheric Sciences, 27*, 871–883, 1970.

Matsuno, T., A dynamical model of the stratospheric sudden warming, *Journal of the Atmospheric Sciences, 28*, 1479–1494, 1971.

Mayr, H. G., J. G. Mengel, C. O. Hines, K. L. Chan, , N. F. Arnold, C. A. Reddy, and H. S. Porter, The gravity wave doppler spread theory applied in a numerical spectral model of the middle atmosphere. 2. equatorial oscillations, *J. Geophys. Res., 102*(D22), 26093–26105, 1997.

Mayr, H. G., J. G. Mengel, and K. L. Chan, Equatorial oscillations maintained by gravity waves as described with the doppler spread parameterization: I. numerical experiments, *J. Atmos. Terr. Phys., 60*(2), 181–199, 1998a.

Mayr, H. G., J. G. Mengel, C. A. Reddy, K. L. Chan, and H. S. Porter, Variability of the equatorial oscillations induced by gravity wave filtering, *Geophysical Research Letters, 25*(14), 2629–2632, 1998b.

McFarlane, N. A., The effect of orographically excited gravity wave drag on the general circulation of the lower stratosphere and troposphere, *J. Atmos. Sci., 44*(14), 1775–1800, 1987.

McIntyre, M. E., On dynamics and transport near the polar mesopause, *Journal of Geophysical Research, 94*, 14617–14628, 1989.

McLandress, C., On the importance of gravity waves in the middle atmosphere and their parameterization in gcms, *J. Atmos. Terr. Phys.*, *60*, 1357–1383, 1998.

Medvedev, A. S., G. P. Klassen, and S. R. Beagley, On the role of an anisotropic gravity wave spectrum in maintaining the circulation of the middle atmosphere, *Geophysical Research Letters*, *25*(4), 509–512, 1998.

Milton, S. F., and C. A. Wilson, The impact of parameterized subgrid-scale orographic forcing on systematic errors in a global nwp model, *Monthly Weather Review*, pp. 2023–2045, 1996.

Molina, M. J., and F. S. Rowland, Stratospheric sink for chloromethanes, chlorine atom catalysed destruction of ozone, *Nature*, *249*, 810–812, 1974.

O'Neill, A., and V. Pope, Simulations of linear and nonlinear disturbances in the stratopause, *Q.J.Royal Met. Society*, *114*, 1063–1110, 1988.

O'Neill, A., V. D. Pope, W. L. Gross, M. Bailey, H. MacLean, and R. Swinbank, Evolution of stratosphere during northern winter 1991-92 as diagnosed from ukmo analyses., *Journal of Atmospheric Sciences*, *51*, 2800–2817, 1994.

Osprey, S., Climate response to a variable gravity wave source, continuing, Ph.D. thesis, University of Canterbury, 2001.

Osprey, S. M., and B. N. Lawrence, A possible mechanism for in situ forcing of planetary waves in the summer extratropical mesosphere., *Geophysical Research Letters, in press*, 2001.

Palmer, T. N., G. J. Shutts, and R. Swinbank, Alleviation of a systematic westerly bias in general circulation and numerical weather prediction models through an orographic gravity wave drag parameterization, *Q. J. R. Meteorol. Soc.*, *112*, 1001–1009, 1986.

Pawson, S., U. Langematz, G. Radek, U. Schlese, and P. Strauch, The berlin troposphere-stratosphere-mesosphere gcm: Sensitivity to physical parameterizations, *Q. J. R. Meteorol. Soc.*, *124*(548 Part-B), 1343–1371, 1998.

Pawson, S., et al., The gcm-intercomparison project for sparc (grips):scientific issues and initial results, *Bulletin of American Meteorological Society*, *81*(4), 781–796, 2000.

Pope, V. D., M. L. Gallani, P. R. Rowntree, and R. A. Stratton, The impact of new physical parameterisations in the hadley centre climate model: Hadam3, *Climate Dynamics*, *16*, 123–146, 2000.

Randel, W. J., F. Wu, R. Swinbank, J. Nash, and A. O'Neill, Global qbo circulation derived from ukmo stratospheric analyse, *J. Atmos. Sci.*, *56*, 457–474, 1999.

Ray, E. A., M. J. Alexander, and J. R. Holton, An analysis of the structure and forcing of the equatorial semiannual oscillation in the zonal wind, *J. Geophys. Res.*, *103*(D2), 1759–1774, 1998.

Reed, R. J., W. J. Cambell, L. A. Rasmussen, and D. G. Rogers, Evidence of a downward-propagating wind reversal in the equatorial stratosphere, *Journal of Geophysical Research*, *66*, 813–818, 1961.

Richardson, L. F., *Weather predictions by numerical models.* Cambridge University Press, 1922.

Rosenlof, K. H., Seasonal cycle of residual mean meridional circulation in the stratosphere, *Journal of Geophysical Research*, *100*, 5173–5191, 1995.

Rosier, S. M., and B. N. Lawrence, The january 1992 stratospheric sudden warming: A role for tropical intertial instability?, *Quarterly Journal of Royal Met. Society*, *125*, 2575–2596, 1999.

Rosier, S. M., B. N. Lawrence, D. G. Andrews, and F. W. Taylor, Dynamical evolution of the northern stratosphere in early winter 1991/92, as observed by the improved stratospheric and mesospheric sounder, *Journal of the Atmospheric Sciences*, *51*(20), 2783–2799, 1994.

Ruth, S. L., J. J. Remedios, B. N. Lawrence, and F. W. Taylor, Measurements of no2 by the uars improved stratosphere and mesosphere sounder, *Journal of the Atmospheric Sciences*, *51*(20), 2818–2833, 1994.

Sato, K., Observation of gravity waves associated with convection, in *Gravity Wave Processes; Thier Parameterization in Global Climate Models*, edited by K. Hamilton, vol. 50 of *Series 1:Global Environment Change*, chap. 5, p. 16. Springer, 1996.

Sato, K., H. Hashiguchi, and S. Fukao, Gravity waves and terbulence assoiciated with cumulus convection observed with the uhf/vhf clear-air doppler radars, *J. Geophys. Res.*, *100*(D4), 7111–7119, 1995.

Scaife, A. A., N. Butchart, C. D. Warner, D. Stainforth, W. Norton, and J. Austin, Realistic quasi-biennial oscillations in a simulation of the global climate., *Geophysical Research Letters*, *27*, 3481–3484, 2000.

Schoeberl, M. R., and D. F. Strobel, The zonally averaged circulation of the middle atmosphere, *J. Atmos. Sci.*, *35*, 577–591, 1978.

Seol, D., and K. Yamazaki, Residual mean meridional circulation in the stratosphere and upper stratosphere, *Journal of the Met. Soc. of Japan*, *77*, 985–996, 1999.

Shutts, G. J., A new wave drag parameterization scheme for the unified model, 1990.

Shutts, G. J., and A. Gadian, Numerical simulations of orographic gravity waves in flows which back with height, *Q. J. R. Meteorol. Soc.*, *125*, 2743–2765, 1999.

Smith, S. A., D. C. Fritts, and T. E. VanZandt, Evidence for a saturated spectrum of atmospheric gravity waves, *Journal of the Atmospheric Sciences*, *44*, 1404–1410, 1987.

Swinbank, R., Examples of hybrid vertical co-ordinate system for the unified forecast/climate model, Technical Note 29, Met. Office U.K., 1989.

Swinbank, R., and A. O'Neill, A stratosphere-troposphere data assimilation system, *Monthly Weather Review*, *122*, 686–702, 1994.

Swinbank, R., W. A. Lahoz, A. O. Neill, C. S. Douglas, A. Heaps, and D. Podds, Middle atmosphere variability in the uk meterological office unified model, *Q. J. R. Meteorol. Soc.*, *124*(549 Part-A), 1485–1525, 1998.

Takahashi, M., Simulation of the quasi-biennial oscillation in a gcm, *Geophysical Research Letters*, *26*(9), 1307–1310, 1999.

Trenberth, K. E. (ed.), *Climate System Modelling.* Cambridge University Press, first edition edn., 1992.

Tsuda, T., T. Inque, T. E. VanZandt, S. Sato, T. Sato, and S. Fukao, Mst radar observations of a saturated gravity wave spectrum, *J. Atmos. Sci.*, *46*, 2440–2447, 1989.

U. S. Standard Atmosphere, U. s. government printing office, washington dc, 1976.

Unified Model User Guide, The u.k. met. office unified model, 1998.

Vincent, R. A., S. J. Allen, and S. D. Eckermann, Gravity wave parameters in the lower stratosphere, in *Gravity Wave Processes; Thier Parameterization in Global Climate Models*, vol. 50 of *Series 1:Global Environment Change*, chap. 2, p. 18. Springer, 1996.

Washington, W. M., and C. L. Parkinson, *An Introduction to Three-Dimensional Climate Modelling.* Univerity Science Books, 1986.

Webster, S., Unified model documentation paper no. 22, gravity wave drag, 1997.

Whiteway, J. A., and A. I. Carswell, Rayleigh lidar observations of the thermal structure and gravity wave activity in the high arctic during a stratospheric warming, *Journal of the Atmospheric Sciences*, *51*(21), 3122–3136, 1994.

Wu, D. L., and J. W. Waters, Satellite observations of atmospheric variances:a possible indication of gravity waves, *Geophysical Research Letters*, *23*, 3631–3634, 1996.

Yang, F., M. E. Schlesinger, and E. Rozanov, Description and performance of the uiuc 24-layer stratosphere/troposphere general circulation model, *Journal of Geophysical Research*, *105*, 17925–17954, 2000.

Yoden, S., T. Yamaga, S. Pawson, and U. Langematz, A composite analysis of the stratospheric sudden warmings simulated in a perpetual january integration of the berlin tsm gcm, *Journal of Met Society of Japan*, *77*, 431–445, 1999.

Yoden, S., M. Taguchi, and Y. Naito, Numerical experiments on internal interannual variations of the troposphere-stratosphere coupled system, in *Report of the Eighth Session of the SPARC scientific steering group.*, no. 16, pp. 18–21. Stratospheric Processes and their Role in Climate, 2001.

Yu, J. R., and C. Y. She, Cimatology of a midlatitude mesopause region observed by a lidar at fort collins, colorado $(40.6^o n, 105^o w)$, *J. Geophys. Res.*, *100*(D4), 7441–7452, 1995.